Check for updates

Electrocatalysis enabled transformation of earth-abundant water, nitrogen and carbon dioxide for a sustainable future

Kaili Liu,[†ab] Pengfei Cao,[†c] Wei Chen,[†a] Collins I. Ezeh,[a] Zijian Chen, [a]
Yonglan Luo, [d] Qian Liu,[e] Haitao Zhao,*[a] Zhenhua Rui,[f] Shuyan Gao, [g]
Zongyou Yin, *[b] Xuping Sun *[d] and Xuefeng Yu [a]

The integration of electrochemistry with catalyst systems underscores a major sustainable scheme for the production of fossil-free fuels and valuable chemicals. This undertaking necessitates the need for rational design of electrocatalysts with high catalytic activity, selectivity, and stability for electrochemical conversion. Significant progress has been made in this regard considering the importance of the products in these reaction systems. Hence, this review presents an update of both experimental and theoretical investigations that can offer insights into the design of high-performance electrocatalysts to facilitate the electrochemical conversion of H_2O, N_2 and CO_2 into value added products. We analyse the current status of available electrocatalysts based on a standard set of figures of merit, namely yield rate, faradaic efficiency, overpotential, current density and stability. Then, we constructively compare the different electrocatalysts based on their reaction mechanisms and operation performances by evaluating the catalyst construction, electrolyte utilization and device practicality. Finally, we provide challenges and prospects from the aspects of both theoretical and experimental insights as a general guide to offer potential future directions.

1. Introduction

Fossil fuels are the primary energy source driving over 86% of the global anthropogenic effect, not to mention their limited abundance that could only sustain for the next 50 years approximately.[1] Their continuous consumption will lead to an increase in the level of atmospheric CO_2 with a deleterious impact on the climate. To effectively mitigate this impact for a sustainable future, it is critical to replace fossil fuels with

[a] *Materials Interfaces Center, Shenzhen Institutes of Advanced Technology, Chinese Academy of Sciences, Shenzhen 518055, Guangdong, China. E-mail: ht.zhao@siat.ac.cn*

[b] *Research School of Chemistry, Australian National University, Canberra, ATC 2601, Australia. E-mail: zongyou.yin@anu.edu.au*

[c] *School of Chemical Engineering and Technology, Xi'an Jiaotong University, Xi'an 710049, Shanxi, China*

[d] *Institute of Fundamental and Frontier Sciences, University of Electronic Science and Technology of China, Chengdu 610054, Sichuan, China. E-mail: xpsun@uestc.edu.cn*

[e] *Institute for Advanced Study, Chengdu University, Chengdu 610106, Sichuan, China*

[f] *Department of Mechanical Engineering, Massachusetts Institute of Technology, Cambridge, 02139, USA*

[g] *School of Materials Science and Engineering, Henan Normal University, Xinxiang 453007, Henan, China*

† These authors contributed equally to this work.

alternative energy sources.[2] Earth's atmosphere provides a universal feedstock of water, carbon dioxide, and nitrogen which can be converted into hydrogen, hydrocarbons and ammonia, respectively. This would significantly contribute to solve societal problems sustainably in terms of clean energy (hydrogen fuel), chemical sources (hydrocarbon, ammonia) and a clean environment (CO_2 capturing).

The development of electrochemical technology that can transform earth-abundant molecules into valuable products offers us the chance to directly address the most pressing environmental challenges and energy crisis by decreasing the utilization of fossil fuels while increasing the production of sustainable fuels and chemicals. Unfortunately, the efficiency and/or stability of such electrochemical processes are still not that satisfactory due to the sluggish kinetics of key reactions and/or the catalyst's susceptibility to the working environment. The integration of the electrochemical processes and rationally designed catalysts is essential for the transformation of these abundant molecules with efficient and versatile platforms to store and utilize green energy and/or produce valuable chemicals for other uses.[3,4]

An emerging sustainable scheme considers the coupling of renewable-energy plants and electrocatalytic reactors, where electrocatalysis can enable the high-performance chemical transformation with improved kinetics, efficiency, and selectivity.

Electrocatalysis is an interdisciplinary area that encompasses the principles of physics, chemistry, and materials science to allow a comprehensive understanding of the reaction kinetics and stability.[5] Hence, insight into electrocatalysis is an indispensable issue to ensure the scalable transformation of earth-abundant molecules for a sustainable future.[6,7]

The pioneering works to transform these molecules have long been recorded in history. Electrochemical water splitting was demonstrated for the production of hydrogen in 1800 by Nicholson and Carlisle.[8] Following the first substantiated report on CO_2 reduction reaction (CRR) *via* electrochemistry by Jordan and Smith in 1960,[9,10] Hori and co-workers revealed the possible means of producing carbonaceous chemicals and fuels using this process in 1985.[11–13] In 1990, electrocatalytic nitrogen reduction reaction to ammonia was reported by Furuya and Yoshiba.[14] Because of these historical initiatives, more scientific studies adopting these chemical transformations and energy conversion processes have been conducted. Despite the recent development, these electrochemical processes are confronted with shortcomings, limiting their practical implementation. Therefore, it is of paramount importance to carry out a systematic review on the development of electrocatalysts for a sustainable future.

Nowadays, high-quality reviews on the general concept of electrocatalysis[3] and electrocatalysts for energy-related reactions[15] and perspectives on electrocatalytic conversion[6] have been reported addressing the fundamentals and technical issues. However, there is still a paucity of information regarding the comprehensive and critical outlook on advanced electrocatalysts for the transformation of these three molecules (water, nitrogen and carbon dioxide) with a systematic and constructive survey. Moreover, the field is developing very rapidly and hence new progress is being made in understanding the role of electrocatalysts in the key reactions such as water splitting, NRR and CRR. Therefore, this field deserves a timely review encompassing the dynamic advancement of electrocatalysis in transforming earth-abundant molecules into valuable products for a sustainable future.

Hence, this study is a critical review of both experimental and theoretical investigations offering insights into catalysts for electrochemical conversion of essential molecules – water, nitrogen and carbon dioxide – and guiding the design of high-performance catalyst systems necessary to facilitate these conversions. Herein, we analyze the current status of available catalytic materials (metal and metal-free) based on a standard set of figures of merit, namely faradaic efficiency, energy efficiency, overpotential, current density, and stability. This approach enables a fair and insightful comparison among the different electrocatalysts, identifies the limiting phenomena, and forecasts the feasibility of practical applications in a much shorter timeframe.

2. Hydrogen production *via* water splitting

Hydrogen energy is a carbon-neutral resource for replacing fossil fuels in the future and the 'hydrogen economy' calls for efficient processes for the production of hydrogen from renewables.[16,17] So far, there are three recognized approaches to produce hydrogen: water splitting, steam reformation of methane and coal gasification.[1] Among them, water splitting is a spotless pathway and indeed represents the most sustainable strategy if backed up by renewable resources. Yet, this route accounts only for approximately 1% of the overall hydrogen production in the world.[18–20] To function effectively, water splitting has been pursuing the development of catalysts that can stabilize and accelerate the reaction along a particular route. Catalysts with good charge transfer, high activity, high selectivity and extensive stability are desired.[21–23] Electrocatalysts have been widely employed to enhance the conversion efficiency of water to H_2 and O_2.[24,25] Herein, we discuss the chemistry underlying the electrosynthesis of H_2 and O_2 from water and thereafter, review recent advancements in the catalytic performances of electrocatalysts towards the overall water splitting.
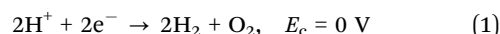
2.1. Electrochemistry of water splitting

A typical water splitting electrolytic cell was first proposed in 1789 by J. R. Deiman and Adriaan Paets van Troostwijk.[26] The water splitting process involves two half-cell reactions: anodic oxidation and cathodic reduction reactions. Alternatively, these reactions are conceptualised as oxygen evolution reaction (OER) and hydrogen evolution reaction (HER), respectively.
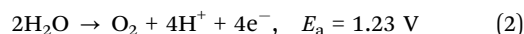
Based on the nature of the electrolytes, the specific half-cell reactions are different at the electrodes. Nevertheless, the overall reaction is the same.[6,27]
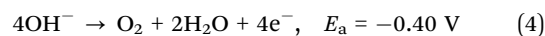
In an acidic electrolyte:

At the cathode:

$$2H^+ + 2e^- \rightarrow 2H_2 + O_2, \quad E_c = 0 \text{ V} \tag{1}$$

At the anode:

$$2H_2O \rightarrow O_2 + 4H^+ + 4e^-, \quad E_a = 1.23 \text{ V} \tag{2}$$

In an alkaline electrolyte:

At the cathode:

$$2H_2O + 2e^- \rightarrow H_2 + 2OH^-, \quad E_c = -0.83 \text{ V} \tag{3}$$

At the anode:

$$4OH^- \rightarrow O_2 + 2H_2O + 4e^-, \quad E_a = -0.40 \text{ V} \tag{4}$$

Overall reaction:

$$2H_2O \rightarrow 2H_2 + O_2 \tag{5}$$
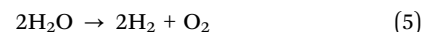
Regardless of the electrolytes, the theoretical reaction potential difference of the process is 1.23 V at 25 °C and atmospheric pressure. The cell potential of the cathode (E_c) and anode (E_a) is based on the normal hydrogen electrode (NHE). For practical application of the water splitting process, an excess potential (overpotential, η_T) is employed for reporting. This excess potential is primarily to overcome the inherent activation difficulties at the cathode (η_c) and anode (η_a) and other associated hindrances (η_{other}) like contact resistance. Realistically, the overall

water splitting reaction is represented with an operational potential (E_{OP}) defined by
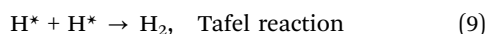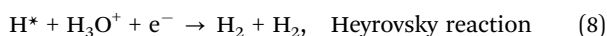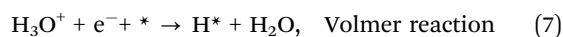
$$E_{OP} = 1.23 \text{ V} + \eta_T$$

$$E_{OP} = 1.23 \text{ V} + \eta_a + \eta_c + \eta_{other} \qquad (6)$$

From this equation, it is paramount to decrease the overpotential (η_T) for the overall reaction to be energy-efficient and economical. Undeniably, the effective reduction of η_c and η_a could be achieved by HER and OER electrocatalysts, respectively. In line with this, optimizing the design of the electrolyzer is an effective strategy for minimizing η_{other}. Detailed discussion on the overpotential and measures for its reduction are described in the literature.[26] To ensure that the overall water splitting process is more economical, the understanding of the fundamentals with recent theoretical insight and the development of efficient HER and OER electrocatalysts are essential. In addition, studies should preferably be centred on non-hazardous, earth-abundant and less expensive materials.[28]
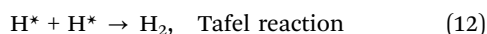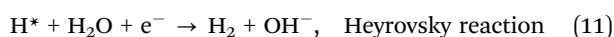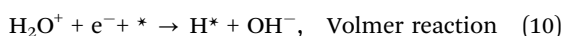
2.1.1. Fundamentals of hydrogen evolution reaction (HER). HER involves a multi-step process with the transfer of two-electrons at the surface of the cathode by two different mechanisms *via* three probable reactions.[29,30]

In an acidic medium[30,31] (* indicates the active site on the catalyst surface),

$$H_3O^+ + e^- + * \rightarrow H* + H_2O, \quad \text{Volmer reaction} \qquad (7)$$

$$H* + H_3O^+ + e^- \rightarrow H_2 + H_2, \quad \text{Heyrovsky reaction} \qquad (8)$$

$$H* + H* \rightarrow H_2, \quad \text{Tafel reaction} \qquad (9)$$

However, in an alkaline medium,[29]

$$H_2O^+ + e^- + * \rightarrow H* + OH^-, \quad \text{Volmer reaction} \qquad (10)$$

$$H* + H_2O + e^- \rightarrow H_2 + OH^-, \quad \text{Heyrovsky reaction} \qquad (11)$$

$$H* + H* \rightarrow H_2, \quad \text{Tafel reaction} \qquad (12)$$

Generally, HER in an alkaline medium is relatively slower than in the acidic medium as it involves the prior dissociation of H_2O to yield the H* intermediates. Irrespective of the HER pathway, the formation of the H* intermediate is necessary. Thus, estimating the extent of the H* adsorption process provides a critical clue about the favorability of the electrode surface to undergo HER. Following this fact, the free energy of hydrogen adsorption (ΔG_{H*}) is a universally established descriptor for hydrogen-evolving materials. The ΔG_{H*} value for an optimal HER catalyst is estimated to be close to zero. The reason for this is that a large ΔG_{H*} suggests the difficulty of breaking the adsorbed H* and hence, impeding H_2 desorption. Moreover, a low ΔG_{H*} value indicates a weak H* adsorption resulting in a poor interaction between the cathode and the protons.

A computationally derived volcano plot of theoretical ΔG_{H*} *vs.* the exchange current densities ($\log j_0$) reflects the HER activities for a range of catalysts.[32] This plot proposes an instinctive approach to visualize and compare the activity of a range of catalysts to enable the optimization of material design

for HER. In addition, understanding the relative HER mechanism for each material is also crucial towards its design. The Tafel slope, derived from the Tafel plot and polarization curve, can be used to understand the HER mechanism.[33,34] This slope is an inherent property of the catalyst, which is computed to define the rate-determining step of the HER process. In general, there are three Tafel slopes recognized to get insight into the reaction kinetics in HER, namely, 29 mV dec^{-1}, 39 mV dec^{-1} and 118 mV dec^{-1}, representing the Tafel, Heyrovsky and Volmer reactions, respectively. The rate-determining step of an electrode is defined by the proximity of its Tafel slope to that of the above-mentioned reactions. However, it is a challenge to unequivocally distinguish whether the rate-determining step is Tafel and Heyrovsky given that the values of their Tafel slopes are similar.
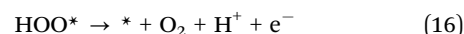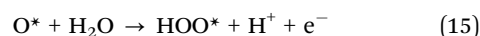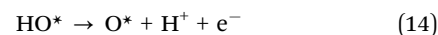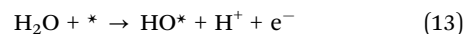
For instance, Zhao and co-workers reported that the Tafel slope of a Pt electrode with the Pt(110) plane is ~ 30 mV dec^{-1}; however, the rate-determining step could be either the Tafel or Heyrovsky reaction despite the value being close to that of Tafel reaction.[35] To distinguish these reactions, the rate-determining steps (Tafel or Heyrovsky) should be related to the surface coverage of H* on the electrode.[35,36] The determination and interpretation of the reaction mechanisms are significant to gain theoretical insight into the elementary steps involved in HER.

2.1.2. Fundamentals of oxygen evolution reaction (OER). As mentioned earlier, OER occurs at the anode as a multi-step process involving the transfer of four-electrons. The mechanism and reaction routes for OER are relatively more intricate than that for HER owing to the slow electro-kinetic profile.[37] Similar to HER, OER differs depending on the medium. In an acidic medium, oxygen (O_2) and a hydrogen ion are formed from the oxidation of H_2O, whereas in an alkaline or neutral medium, H_2O and O_2 are formed from the oxidation of a hydroxyl ion (OH^-).

These reactions occur with the involvement of adsorbed OH^-, O^{2-} and OOH^- intermediates on the surface of the catalyst. Hypothetically, a generally accepted OER mechanism is illustrated as follows.[38]

OER in an acidic medium:

$$H_2O + * \rightarrow HO* + H^+ + e^- \qquad (13)$$

$$HO* \rightarrow O* + H^+ + e^- \qquad (14)$$

$$O* + H_2O \rightarrow HOO* + H^+ + e^- \qquad (15)$$

$$HOO* \rightarrow * + O_2 + H^+ + e^- \qquad (16)$$

OER in an alkaline medium:

$$OH^- + * \rightarrow HO* + e^- \qquad (17)$$

$$OH^- + HO* \rightarrow O* + H_2O + e^- \qquad (18)$$

$$O* + OH^- \rightarrow HOO* + e^- \qquad (19)$$

$$4HOO* \rightarrow * + O_2 + 2H_2O + e^- \qquad (20)$$
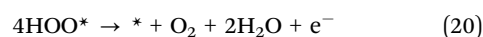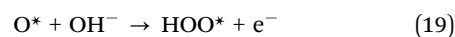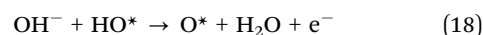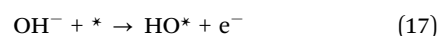
Recently, density functional theory (DFT) computation provided insight into the underlying mechanisms for each reaction step as follows:[39]

$$2H_2O + {}^* \rightarrow H_2O + HO^* + H^+ + e^- \tag{21}$$

$$\Delta G_1 = \Delta G_{HO^*} - \Delta G_{H_2O} - eU + k_B T \ln[H^+] \tag{22}$$

$$H_2O + HO^* \rightarrow H_2O + O^* + H^+ + e^- \tag{23}$$

$$\Delta G_2 = \Delta G_{O^*} - \Delta G_{HO^*} - eU + k_B T \ln[H^+] \tag{24}$$

$$O^* + H_2O \rightarrow HOO^* + H^+ + e^- \tag{25}$$

$$\Delta G_3 = \Delta G_{HOO^*} - \Delta G_{O^*} - eU + k_B T \ln[H^+] \tag{26}$$
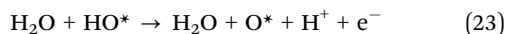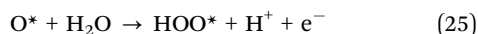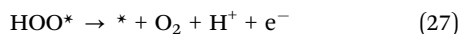
$$HOO^* \rightarrow {}^* + O_2 + H^+ + e^- \tag{27}$$

$$\Delta G_4 = \Delta G_{O_2} - \Delta G_{HOO^*} - eU + k_B T \ln[H^+] \tag{28}$$

where ΔG_i is the Gibbs free energy of the ith reaction step; U represents the measured electrode potential (*vs.* NHE under standard conditions); k_B is the Boltzmann constant; and T is the absolute temperature. ΔG_1, ΔG_2, and ΔG_3 (and ΔG_4) refer to the adsorption energies of HO*, O* and HOO*, respectively. For an ideal case, ΔG_{HO^*}, ΔG_{O^*}, and ΔG_{HOO^*} are 1.23 eV, 2.46 eV and 3.69 eV, respectively.[40]

Under standard conditions, when the measured electrode potential is 0 *versus* the standard hydrogen electrode (SHE), the theoretical overpotential η^{OER} is defined as[26]

$$\eta^{OER} = \left(\frac{G^{OER}}{e}\right) - 1.23 \text{ V} \tag{29}$$

where G^{OER} is the largest Gibbs free energy of the reactions ($G^{OER} = \max\{\Delta G_1, \Delta G_2, \Delta G_3, \Delta G_4\}$).[41]

For minimal overpotential ($\eta^{OER} = 0$), ΔG^{OER} is 1.23 eV. Given that $\Delta G_1 = \Delta G_2 = \Delta G_3 = \Delta G_4$ for an ideal OER catalyst under standard conditions, this suggests that the ΔG for each step at $\eta^{OER} = 1.23$ eV.[40] Based on this hypothesis, a volcano plot analogous to that for the HER catalysts is obtained for a range of OER catalysts (Fig. 1). Here, the standard free energy $(\Delta G_{O^*}^0 - \Delta G_{HO^*}^0)$ is plotted against the theoretical overpotential to reflect the OER activities for a series of catalysts. $\Delta G_{O^*}^0 - \Delta G_{HO^*}^0$ is a notable descriptor for OER activity. Deductions from the volcano plot indicate that the plot can be beneficial towards the design and optimization of highly efficient OER catalysts. Moreover, the Tafel slope, which is also correlated with the OER overpotential, can direct the understanding of the OER mechanism by providing kinetic information of OER catalysts.[42]

2.2 Electrocatalysts for water splitting

To sustain an efficient and economic water splitting process, HER–OER bifunctional catalysts that can offer a minimum overpotential in aqueous alkaline or acidic medium are indispensable.[44] However, the design and development of electrocatalysts are complex and challenging as several factors need to be considered in this regard.[45] For instance, the electrocatalysts suitable for alkaline solutions may be unstable or inactive in acidic medium, and *vice versa*. Therefore, it is
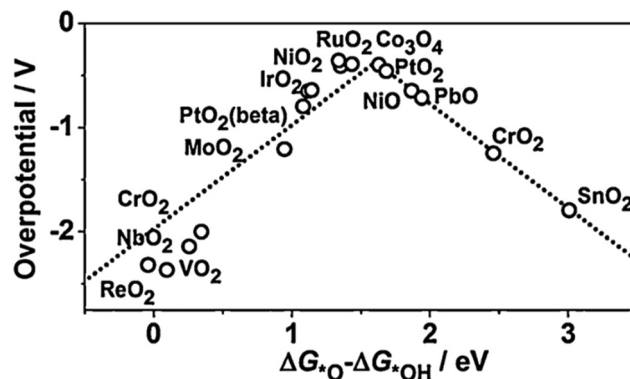

Fig. 1 Volcano plot for OER on metal oxides. Reproduced with permission.[43] Copyright 2015, Elsevier.

exceedingly attractive to develop bifunctional electrocatalysts with high activity towards both OER and HER in the same electrolyte.[46,47]

Hitherto, both metal-based and metal-free catalyst systems have shown potential to catalyze the water splitting process. Metal-based catalyst systems including noble metals (such as iridium (Ir), palladium (Pd), platinum (Pt), ruthenium (Ru) and gold (Au)) and transition metals (TMs, such as cobalt (Co), iron (Fe), nickel (Ni), molybdenum (Mo) and copper (Cu)) and their compounds are the most widely utilized HER–OER electrocatalysts. However, owing to their structural complexities, physiochemical challenges and thermodynamic instability, these catalyst systems are constrained by their weak durability and low selectivity. This coupled with their high cost has led to research endeavor to seek for alternatives to replace metal-based electrocatalysts for water splitting.[44]

Following the discovery of carbon-based materials as oxygen reduction reaction (ORR) catalysts in 2009, steps were taken to design and develop metal-free electrocatalysts for water splitting. Thereafter, considerable headway has been made in this regard, particularly with respect to earth-abundant metal-free materials.[44,45] Beyond their natural abundance, metal-free electrocatalysts have demonstrated good catalytic performance for water splitting due to their remarkable electrical conductivity, large surface area and high tolerance under wide operating conditions.[46,48] Moreover, the flexible architecture of metal-free catalysts exposes these materials to potential heteroatom doping and structure reengineering, which can modulate the charge distribution of the carbon genomics with potential synergistic effects for water splitting.[49] Notable examples of these catalysts include heteroatom-doped carbon nanotubes and graphene.[50]

Apart from the category, composition and structure of electrocatalysts, the properties (*e.g.* pH) of electrolytes play a role in the electrochemical water splitting reactions. The acidic electrolytes are beneficial for water splitting as they offer more hydroniums (H_3O^+) with weak covalent bonding and thereby lead to fast reaction kinetics for the reduction reaction at the cathode while the alkaline water splitting is more popular than acidic water splitting because of the availability of more choice

of electrocatalysts for anodic half-cell OER reaction and the facile formation of OH* and O* species.[51] Moreover, the strong acid condition requires the employment of an acid proton exchange membrane and suffers from the issue of high cost and pollution from the evaporated acid electrolyte. Comparatively, an alkaline electrolyte can relieve these problems in acid conditions for water splitting. The alkaline environment, typically realized by the adoption of 1.0 M KOH solution, has been widely employed for water splitting and has demonstrated inspiring performance over the past few decades.[51] However, the drawbacks of harsh alkaline or acidic electrolytes such as the corrosion issue and the requirement of specific ion exchange membranes with good stability are inescapable when it comes to applications. Therefore, electrochemical water splitting under neutral and near-neutral conditions has gained much research interest.[52,53] Different from water electrolysis under extreme acidic or alkaline conditions, water splitting under neutral or near-neutral conditions is seriously affected by reactant switching and identity and concentration of the buffered anions in similar pH values. Thus, buffer solutions, for instance phosphate buffered saline (pH 7), bicarbonate and carbonate buffer solution (pH 9.2 to 10.6), sodium sulfate solution (pH 7) and borate buffer solution (pH 8.5), are widely used in neutral electrocatalytic water splitting.[54]

Shu-Hong Yu and co-workers[55] reported the synthesis and application of ternary $Ni_{0.1}Co_{0.9}P$ porous nanosheets onto conductive carbon fiber paper which exhibited promising potential in neutral-pH water electrolysis. The ternary $Ni_{0.1}Co_{0.9}P$ catalyst endows the resultant device with a voltage requirement of mere 1.81 V to reach a current density of 10 mA cm^{-2}, showing excellent efficiency among the noble-metal-free neutral-pH electrolyzers. Jie Yu and co-workers[56] reviewed the recent research on the electrocatalytic water-splitting performance of precious-metal-free catalytic materials in neutral media. Anantharaj and Aravindan[54] summarized 3d transition-metal-based electrocatalysts for neutral and near-neutral water splitting from the perspective of activity, selectivity, and stability. These reviews provide a comprehensive summary of the catalytic performance of catalysts with neutral electrolytes. It is worth noting that the neutral electrolytes are good electrolytes with potential as they have more similar physical and chemical properties to seawater. However, most electrocatalysts towards overall water splitting showed better efficiency in alkaline electrolytes. It is still promising to develop efficient electrocatalysts in a neutral or near neutral pH environment.

In general, bifunctional electrocatalysts preferentially favor either the HER or OER depending on their intrinsic characteristics. Hence, to enable a high overall performance, the intrinsic activity and physiochemical properties of the catalysts should be synergistically improved.[46] In this section, we critically review the recent advances in metal-based and metal-free electrocatalysts towards the overall water splitting process, and discuss the theoretical perspectives in understanding the catalytic process and recent challenges.

2.2.1 Noble metal-based electrocatalysts. The design and development of an energy-efficient electrocatalyst for cathodic

HER and anodic OER are aimed to overcome the large water-splitting overpotentials.[20] To date, the noble metal-based electrocatalysts (Ir, Pd, Pt, Rh and Ru) are still the most effective catalyst systems for water splitting, particularly in an acidic solution. Pt-based materials are known to possess the highest activity toward HER,[57] while Ir- and Ru-based materials are the most efficient OER electrocatalysts.[58] This is due to their superior properties such as large specific surface area, unique pore structure, and excellent structural stability.[59,60] However, owing to their rarity and high cost, research studies have engaged in developing bifunctional electrocatalysts with minimal noble metal loading, offering high catalytic activity and stability. Numerous schemes such as size reduction, shape modulation, heteroatom doping, and anchoring noble metals on a support have been proposed to improve the performances.[60] The alloying of noble metals with bi- or multi-metallic elements has been proven to improve the OER-HER activity of noble metals.[61] Guo and co-workers demonstrated the superior water splitting performance of bimetallic doped IrCoNi porous hollow nanocrystals (PHNCs) over the single doping. When tested in 0.5 M H_2SO_4, IrCoNi PHNCs displayed a low cell voltage of 1.56 V at 2 mA cm^{-2} current density with excellent stability after 1000 cycles (Fig. 2(a) and (b)).[61] The improved electrocatalytic activity was attributed to the large surface area due to the porous nature and size reduction.

Alternatively, the anchoring of noble metals on support surfaces has presented a myriad of novel heterogeneous electrocatalysts with high HER–OER activity. This approach typically augments the interaction between the metals and the support, thereby leading to an enhanced charge distribution. Specifically, exploiting surface defects on the support (particularly supports that offer enriched coordinating atoms with lone electron pairs as active centers) and fabricating porous frameworks are the most recently adopted schemes to improve the catalytic activity.[60] For instance, Lee and co-workers utilized a structure-supporting hemispherical core–shell to fortify the HER–OER activity on an Ir-based multi-metallic nanoframe anchored on an Au-based core (AuCu@IrNi).[62] Here, the authors demonstrated that the developed hemicore@frame AuCu@IrNi complex suitably catalyzed OER and HER in 0.1 M $HClO_4$ with low overpotentials of 308 mV and 13.7 mV with Tafel slopes of 58 mV dec^{-1} and 22 mV dec^{-1}, respectively (Fig. 2(c) and (d)).

Table 1 summarizes the catalytic activity of some of the bifunctional water splitting electrocatalysts. Generally, most noble metals are inclined to favor either the OER or HER process; therefore they are not so effective for bifunctional water splitting, particularly in the same medium. It is well documented that modulating the surface morphology, electronic structure, and element doping (bi- or multi-metallic) plays a crucial role in upgrading the activity of noble metal-based materials as OER-HER bifunctional electrocatalysts. Nonetheless, the commercial application of these catalysts is limited by their scarcity and high cost. This has driven the research interest for the design of efficient catalyst systems made from readily available and low-cost materials such as earth-abundant materials.
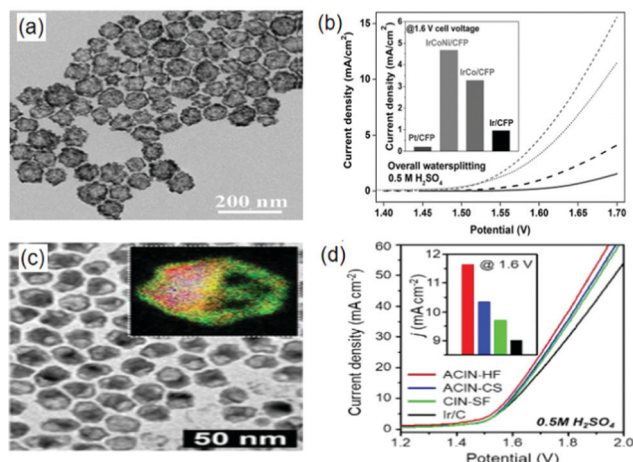
Fig. 2 (a) TEM image of IrCoNi PHNCs and their (b) polarization curve in comparison to that of IrCo/CFP, Ir/CFP, and Pt/CFP for overall water splitting in 0.5 M H_2SO_4 solution at a scan rate of 5 mV s^{-1} (inset: with the corresponding current densities at 1.6 V). Panels (a) and (b) are reproduced with permission.[61] Copyright 2017, Wiley-VCH. (c) TEM image of AuCu@IrNi and (d) polarization curves of ACIN-HF/CFP, ACIN-CS/CFP, CIN-SF/CFP and Ir/CFP for overall water splitting in 0.1 M $HClO_4$ solution at a scan rate of 5 mV s^{-1} (inset: with the corresponding current densities). Panels (c) and (d) are reproduced with permission.[62] Copyright 2019, Royal Society of Chemistry.

2.2.2 Non-noble metal-based electrocatalysts. Recently, a vast number of non-noble metal-based electrocatalysts have been extensively investigated for electrochemical water splitting.[15] Among them,[60,63,64] this section will focus on earth-abundant transition metal-based electrocatalysts (such as Ni-, Co-, Cu-, Fe-, Mo- and W-based materials) due to their theoretically asserted high electrocatalytic performances with low-cost.[65,66] To present a fair comparison, the different electrocatalysts have been divided into major groups including metallic substances, metal hydroxides/oxides, metal chalcogenides, metal phosphates/phosphides, metal nitrides and metal carbides. Correspondingly, the investigated bifunctional electrocatalysts are listed in Table 1.

Metallic substance. Metallic substances are well-known electrocatalysts that are commonly used in the commercial application of electrolytic water splitting.[67,68] Nevertheless, this set of electrocatalysts are known to exhibit low efficiency and less stability necessitating measures to enhance their electrocatalytic activity. For instance, Martindale and Reisner reported the unstable condition of Fe due to its dissolution at the anodic and cathodic potentials under neutral and acidic media, respectively.[69] Similarly, Jahan and co-workers reported the instability of Cu complexes due to their corrosion and instability in an acidic medium.[63]

One option is incorporating the metal based materials with non-metal or another transition metal based dopant.[68,70–72] Our group reported an amorphous Ni-B nanoparticle film on Ni foam (Ni-B/Ni foam) with good water splitting potential (Fig. 3(a) and (b)). An electrolytic cell voltage of 1.69 V was required to attain 15 mA cm^{-2} current density in 1.0 M KOH with overpotentials of 125 mV and 360 mV at 20 mA cm^{-2} and 100 mA cm^{-2} for the HER and OER, respectively.[68]

In the past, Co-[70,73–75] and Fe-based[76–78] compounds have been used as potential water splitting electrocatalysts. However, given that Fe is one of the most abundant earth metals and highly attractive for the development of low-cost catalysts, Fe-based compounds have been extensively examined as HER or OER electrocatalysts.[76–78] Nonetheless, similar to Co-based metallic compounds, only a fair number of studies have reported the bifunctionally active catalysts compared to the Fe-based metallic compounds for water splitting. Among those studies, Martindale and Reisner demonstrated an Fe-only electrode to be active for catalysing both proton reduction and water oxidation in alkaline medium with superior activity than bifunctional Co and Ni electrocatalysts.[69] The authors also demonstrated that the electrolyzer system with an Fe-only electrode was relatively more stable and durable. This was ascribed to the reversible interconversion of catalytically active Fe-species (an iron oxide-hydroxide (FeO_x) phase under the anodic bias and Fe(0) phase under the cathodic bias).

Another example of low-cost catalytic materials is Cu and its derivatives, which are reported to be beneficial towards the activation of oxygen reduction reaction (ORR)[79] and serve as HER/OER electrocatalysts.[63,80] However, similar to Co-based metallic materials, the practical application of Cu-based metallic catalysts is hindered by their large overpotential and/or low stability, which requires further modifications. For instance, Jahan and co-workers fabricated a Cu-MOF composite by anchoring a Cu-centered MOF on graphene oxide (GO),[63] which was employed as a tri-functional HER, OER and ORR electrocatalyst, particularly in an acidic solution. The exceptional performance of the catalyst was founded on the GO-MOF synergistic effects including the unique porous scaffold structure and improved electron transport. Likewise, anchoring Co on N-doped carbon nanostructures (Co–N–C)[81,82] has been demonstrated to result in robust water splitting electrocatalysts due to the synergistic chemical coupling between the embedded Co and the N-dopant or carbon layers, leading to a better H-bonding energy necessary for HER[82] and both greater mechanical and chemical rigidity.

Furthermore, the doping of these metallic catalysts with other metals or non-metals has also been shown to improve their individual electrocatalytic performance. For instance, the incorporation of Fe with Ni resulted in a Ni–Fe composite which displayed high potential as a HER–OER electrocatalyst in alkaline solutions, requiring overpotentials of only 240 and 270 mV to deliver current densities of 500 and 1000 mA cm^{-2}, respectively. The electrode also displayed prolonged stability against bulk water electrolysis at large currents[83] attributed to the optimal behaviour of this binary film due to the stabilizing effect of Fe on Ni at a higher oxidation level.[84]

The use of 3D catalytic substrates has been demonstrated towards improving the surface morphology, exposed active centres and electrical characteristics of the electrocatalysts.[70,83,85,86] A commonly used low-cost conductive substrate is Ni foam, which when compared to other substrates such as Ni foil has shown superior activity due to its 3D macroporous structure and structure-induced electronic effect.[83] In addition, Ni foam

Table 1 Summary of the performances of water-splitting electrocatalysts

| Electrocatalyst	Electrolyte	Mass loading (mg cm^{-2})	Overpotential@j (mA cm^{-2}) (mV) HER	OER	Tafel slope (mV/dec) HER	OER	Cell voltage (V)@j (mA cm^{-2})	Overall stability	Ref.
Noble metal-based									
AuCu@IrNi	0.1 M HClO$_4$	—	13.7@10	308@10	22	58	—	—	62
	0.5 M H$_2$SO$_4$	—	—	—	—	—	1.585@10	24 h	
IrCo alloys	0.5 M H$_2$SO$_4$	0.0189 (Ir)	23.9@10	270@10	25.7	71.8	1.55@10	100 min	165
IrNiCo PHNC	0.5 M H$_2$SO$_4$	—	68@10	309@10	—	—	1.52@2	1000 cycles	61
	0.1 M HClO$_4$	—	50@17.43	303@10	31.9	53.8	—	200 min	
Pt$_{62}$Co$_{23}$/Ir$_{15}$ FBNWs/C	0.1 M HClO$_4$	—	14@10	308@10	—	—	1.53@10	10 h	166
Ru$_2$Ni$_2$ SNs	1.0 M KOH	—	39.3@10	357@10	25	∼100	1.58@10	40 h	167
Non-noble metal-based									
Metallic substance									
Cu–MOF (8%GO)	0.5 M H$_2$SO$_4$	0.226	209@30	110@2	84	65	—	—	63
Fe-FeO$_x$-FeS$_x$	0.1 M KOH	—	360@10	400@10	—	—	1.68@10	3 d	69
Ni-B/Ni foam	1.0 M KOH	12.3	125@20	360@100	93	76	1.69@15	10 h	68
CoSn$_2$	1.0 M KOH	∼1	196@10	299@10	78	89	—	—	168
		∼3	103@10	230@10	—	—	1.55@10	16 h	
Co:W:Cu (1:1.5:8)	0.1 M KOH	1.25	103@10	313@10	335 ± 1.0	162 ± 0.7	1.8@10	10 h	80
Metal chalcogenides									
Ni$_3$S$_2$/NF	pH 14	1.6	223@10	260@10	—	—	1.76@13	>200 h	87
NiSe/NF	1.0 M KOH	2.8	96@10	270@20	120	64	1.63@10	12 h	70
Zn$_{0.1}$Co$_{0.9}$Se$_2$	1.0 M KOH	0.285	—	340@10	—	43.2	—	—	169
	0.5 M H$_2$SO$_4$		140@10	—	49.9	—	—	—	
MoS$_2$/Ni(OH)$_2$	1.0 M KOH	—	134@10	233@10	35	49	1.46@10	50 h	94
MoS$_2$/Ni$_3$S$_2$	1.0 M KOH	7	110@10	218@10	83	88	1.56@10	10 h	115
(Ni, Fe)S$_2$/MoS$_2$	1.0 M KOH	—	130@10	270@10	101.22	43.21	1.56@10	28 h	170
Ni/Ni$_9$S$_8$	1.0 M KOH	11.04	230@10	340@30	123.3	109.8	—	—	139
H–Fe–CoMoS	1.0 M KOH	—	137@10	282@10	98	58	1.60@20	—	171
Co$_9$S$_8$/Ni$_3$S$_2$	1.0 M KOH	—	128@10	227@10	97.6	46.5	1.64@10	12 h	116
CuCo$_2$S$_4$	1.0 M KOH	∼2	158@10	290@20	113	—	1.66@10	24 h	105
Mo/Mn-Ni$_x$S$_y$/NF	1.0 M KOH	7.67	162@50	144@10	91	110	1.49@10	24 h	172
NCT-NiCo$_2$S$_4$	1.0 M KOH	—	295@100	330@100	86.8	86.8	1.60@10	15 h	173
NiCo$_2$S$_4$ NA/CC	1.0 M KOH	4	263@50	310@50	141	89	1.68@10	12 h	114
			305@100	340@100					
Metal phosphates and phosphides									
Fe$_2$P	0.5 M H$_2$SO$_4$	—	191@10	—	55	—	—	—	142
	1.0 M KOH	—	300@10	390@10	126	—	—	—	
FeP NTs	0.5 M H$_2$SO$_4$	1.6	88@10	—	35.5	—	1.69@10	14 h	141
	1.0 M KOH		120@10	288@10	59.5	43	—	—	
Ni-P foam	1.0 M KOH	—	150@10	350@191	—	179.9	1.44@5	26 h	174
Ni$_2$P	1.0 M KOH	0.14	220@10	290@10	—	59	1.63@10	210 min	136
Ni$_5$P$_4$	0.5 M H$_2$SO$_4$	3.5	140@10	—	40	—	1.7@10	20 h	138
	1.0 M KOH	—	150@10	290@10	53	—	—	—	
Co-P-B	1.0 M KOH	0.3	145@10	290@10	38	48	1.65@10	20 h	175
Ni/Ni$_8$P$_3$	1.0 M KOH	10.58	130@10	270@30	58.5	73.2	1.61@10	24 h	139
NiFeP	0.5 M H$_2$SO$_4$	—	143@10	—	67	—	—	—	142
	1.0 M KOH	—	255@10	227@10	83	—	—	—	
LiCoBPO	1.0 M KOH	∼1	245@10	293@10	98	58	1.94@10	90 h	176
		∼3	121@10	216@10	121	62	1.84@10	10 days	
NaCoBPO	1.0 M KOH	∼1	298@10	328@10	124	60	—	—	176
		∼3	207@10	242@10	128	99	—	—	
N-NiCoP/NCF	1.0 M KOH	∼2.085	78@10	225@10	83.17	66.94	—	100 h	177
Metal nitrides									
TiN@Ni$_3$N	1.0 M KOH	0.6	21@10	350@10	42.1	—	1.64@10	16 h	148
Ni$_3$FeN-NPs	1.0 M KOH	0.35	158@10	280@10	42	46	—	9 h	151
Ni$_3$N-NiMoN	1.0 M KOH	∼1.63	31@10	277@10	64	118	1.54@10	20 h	178
Metal carbides									
β-Mo$_2$C	1.0 M KOH	0.25	130@10	274@10	66.5	70	1.65@10	30 h	179
B, N: Mo$_2$C/BCN	1.0 M KOH	∼1.0	100@10	360@100	62	61	1.84@100	20 h	180
Metal-free									
e-ICLDH@GDY	1.0 M KOH	—	43@10	216@10	98.9	43.6	1.43@10	60 h	181
		—	215@100	249@100	—	—	1.46@100	—	
		—	256@1000	278@1000	—	—	1.49@1000	—	
ONPPGC/OCC	1.0 M KOH	0.1	446@10	410@10	154	83	1.66@10	10 h	163
	0.2 M PBS		352@1	420@2	374	231	1.71@2		
	0.5 M H$_2$SO$_4$		386@10	470@10	109	200	1.75@5		
PO-Ni/Ni-N-CNFs	1.0 M KOH	8	262@10	420@10	97.42	113.1	1.69@10	40 h	158
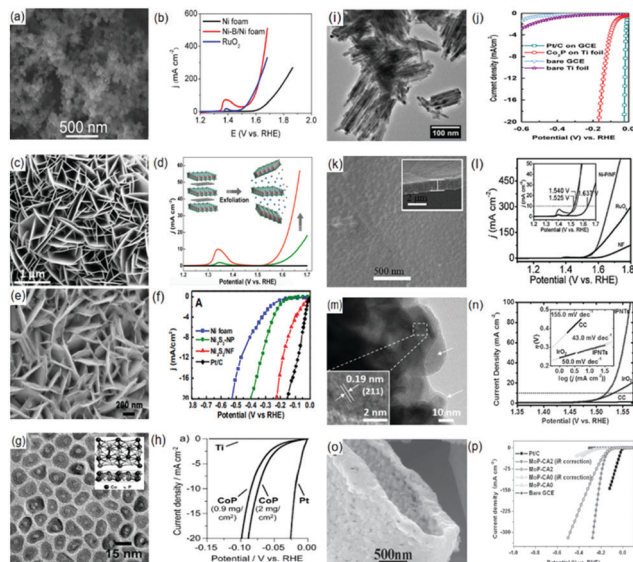
Fig. 3 (a) SEM image of Ni-B/Ni foam. Polarization curve (in 1.0 M KOH at a scan rate of 2 mV s^{-1}) for (b) OER on Ni foam, Ni-B/Ni foam and RuO$_2$-Ni foam. Panels (a) and (b) are reproduced with permission.[68] Copyright 2016, IOP Publishing Ltd. (c) TEM image of as-synthesized NiCo LDH nanoplates on carbon paper *via* HCFR. (d) Polarization curves (in O$_2$-saturated 1 M KOH at a scan rate of 0.5 mV s^{-1}) of NiCo LDH catalysts and carbon paper. Images (c) and (d) are reproduced with permission.[113] Copyright 2015, American Chemical Society. (e) Top-view SEM image of Ni$_3$S$_2$/NF. (f) Steady-state current density as a function of applied voltage during HER at pH 7 over nickel foam (NF), Ni$_3$S$_2$-NP, Ni$_3$S$_2$/NF and Pt/C(20 wt%). Images (e) and (f) are reproduced with permission.[87] Copyright 2015, American Chemical Society. (g) TEM image of CoP nanoparticles. (h) HER performance of the CoP/Ti electrode in 0.5 M H$_2$SO$_4$. Panels (g) and (h) are reproduced with permission.[129] Copyright 2014, Wiley. (i) TEM image of the Co$_2$P nanorods. (j) Polarization curves of Pt/C on GCE (loading amount: 0.285 g cm^{-2}), Co$_2$P on Ti foil, bare GCE, and bare Ti foil in 0.5 M H$_2$SO$_4$ solution (iR corrected). The bare Ti foil was subjected to the same annealing treatment as Co$_2$P on a Ti foil sample prior to the measurement. Panels (i) and (j) are reproduced with permission.[130] Copyright 2014, Elsevier. (k) SEM image of Ni-P/NF (inset: cross-sectional analysis). (l) Polarization curve (in 1.0 M KOH at a scan rate of 2 mV s^{-1}) for OER on Ni-P/NF, NF, and Pt/C-NF. Panels (k) and (l) are reproduced with permission.[85] Copyright 2015, Wiley. (m) HRTEM image of IPNTs (inset: enlarged HRTEM image). (n) iR-Corrected LSV curves measured in 1.0 M KOH (inset: the corresponding Tafel slopes). Panels (m) and (n) are reproduced with permission.[141] Copyright 2015, Wiley. (o) High-magnification SEM images of the MoP-CA2 microstructure, and (p) polarization curves (in 0.5 M H$_2$SO$_4$ with a scan rate of 2 mV s^{-1}) of MoP-CA2, MoP-CA0, Pt/C, and bare GCE. Reproduced with permission.[64] Copyright 2014, Wiley.

offers a much higher surface roughness than Ni foil, which tends to promote more surface activity.[87,88] Other reported common conductive substrates include Ti plate[27,44,89] and Cu foam.[90]

Metal chalcogenides. Metal chalcogenides such as sulfides[70,72,85,91] and selenides[44,70,89,90,92,93] have demonstrated highly efficient performance in catalyzing HER–OER. Frequently investigated metal chalcogenides for water splitting include Ni-,[70,86,94] Co-,[95,96] Mo- (MoS$_2$[97,98] and MoSe$_2$[99,100]) and W-[101] chalcogenides. In 2013, our group disclosed that the cobalt sulfide (Co–S) film is effective as a HER–OER electrocatalyst with

a faradaic efficiency of almost 100% in 1.0 M KOH.[102] The Co–S film exhibits a promising activity in the production of H$_2$ from seawater. However, it suffers from stability issues in acidic medium (0.5 M H$_2$SO$_4$). Moreover, Co–S anchored on a conductive template such as Ti mesh has also revealed high catalytic activity and good stability as an OER electrocatalyst.[70] Other adoptable conductive substrates include carbon-based materials such as carbon nanotubes (CNTs) and reduced graphene oxide (RGO).[103,104] The interconnected CNT architecture offers improvement in porous characteristics while ensuring high electronic and mass transport. On the other hand, the RGO sheets are known to promote interfacial contact, thereby enhancing particle distribution and exposure of active sites.

Similar to the effect of bi-/multi-metallic elements on noble metal electrocatalysts, studies have shown that bi-/multi-metallic sulfides have superior activity towards HER than their single component monometallic counterparts.[96,101,105] However, the nature of the involved metal atoms and their respective compositions play a paramount role in the catalytic activities. For instance, Ni$_{0.68}$Co$_{0.32}$S$_2$ NWs displayed a lower HER activity than the undoped counterparts, CoS$_2$ and NiS$_2$.[96] On the other hand Ni$_{0.33}$Co$_{0.67}$S$_2$ NWs grown on Ti foil synthesized *via* sulfurization of the NiCo$_2$O$_4$ precursor displayed the best HER activity in both neutral and alkaline media as compared to the undoped CoS$_2$ and NiS$_2$.[106] Similarly, our group demonstrated that the presence of Co (NiCo$_2$S$_4$ NA/CC) enhances the catalytic activity as witnessed from the observed current density of 100 mA cm^{-2} at an overpotential of 305 mV (for HER) and 340 mV (for OER). The outstanding performance of NiCo$_2$S$_4$ NA/CC was attributed to the high capacitance of the catalyst indicating a high surface roughness and surface area.

In an acidic medium, cobalt selenides are more stable electrocatalysts for water splitting than cobalt sulfides, especially when supported on carbon black,[96] carbon fiber paper (CFP)[107] and carbon cloth (CC).[108] Attributable features for the improved HER–OER activity include the increased surface area and boosted electrical conductivity. Other notable approaches for enhancing the catalytic efficacy of cobalt selenides include grafting or anchoring other components into the structure of the electrocatalysts. In this direction, numerous composites based on CoSe$_2$ nanobelts with tremendous water splitting capacity have been developed. These include Ni/NiO/CoSe$_2$[109] and MoS$_2$/CoSe$_2$[110] composites for the HER process, and Mn$_3$O$_4$/CoSe$_2$,[111] N-doped graphene (NG)/CoSe$_2$[112] and CeO$_2$/CoSe$_2$[106] for the OER process. The enhanced OER and HER activities of these composites are ascribed to the synergetic chemical coupling effects.

Anchoring of the catalyst system on other components has been widely adopted to boost the catalytic performance of water splitting electrocatalysts. For example, Jin and coworkers introduced a high pressure and temperature hydrothermal continuous flow reactor (HCFR) for synthesizing NiCo LDHs on carbon fiber. The HCFR enabled the stable control of the reactor pressure that assisted the better tuning of the LDH size and morphology (Fig. 3(c)), which led to a current density of 10 mA cm^{-2} at 367 mV (*vs.* RHE) (Fig. 3(d)).[113] On the other

hand, Liu *et al.* showed that the $NiCo_2S_4$ nanowire array on carbon cloth ($NiCo_2S_4$ NA/CC) showed a better HER–OER performance than $NiCo_2O_4$ NA/CC. This was because at the beginning of the OER process, NiOOH and $Co(OH)_2$ formed at the surface of $NiCo_2S_4$ which served as the active phases for the OER.[114]

Furthermore, Feng and co-workers revealed that Ni_3S_2 nanoarrays deposited on a good conductive substrate like nickel foam (NF) are active and stable bifunctional water splitting electrocatalysts (Fig. 3(e) and (f)).[87] Similarly, a NiSe nanowire film anchored on nickel foam (NiSe/NF) fabricated by means of a hydrothermal reaction of NF and NaHSe was reported to be an efficient bifunctional water splitting electrocatalyst. However, theoretical evidence reveals that the harmonious effect of the interconnected architecture of catalyst's nanoarrays and the high-index planes is responsible for its unique electrocatalytic efficacy.[70]

For enriching the active sites, an interfaced MoS_2/Ni_3S_2 heterostructure engineered on NF as an advanced bifunctional electrocatalyst was developed.[115] The generated abundant interfaces delivered 10 mA cm^{-2} current density at a very low cell voltage of 1.56 V (*vs.* RHE). Coupled with theoretical calculations, it was revealed that the generated interfaces synergistically facilitated the chemisorption of H- and O-bound intermediates, thus expediting the overall water splitting process. Moreover, it was also confirmed that the induced lattice defects arising from the existence of Co_9S_8 and Ni_3S_2 combined phases highly contributed to the improved chemisorption of H and O-containing intermediates.[116] On these defective heterointerfaces, DFT computation revealed a lower free energy for hydrogen (ΔG_H) and hydroxide (ΔG_{OH}), indicating a conducive active site for both HER and OER processes.

Metal phosphates and phosphides. In the past few decades, a myriad of transition metal based electrocatalysts have been used as potential water splitting electrocatalysts.[70,73–75,117] Among these electrocatalysts, phosphates are one of the most studied bifunctional HER–OER electrocatalysts.[24,37,118–120] In 2008, Nocera and co-workers reported an *in situ* synthesis approach for Co^{2+}/phosphate as OER catalysts by means of an indium tin oxide (ITO) substrate in Co^{2+}-containing phosphate buffered saline (PBS).[121,122] Nonetheless, the catalytic activity of this catalyst is pH-dependent. This is quite similar to the study of Artero and co-workers where a robust cobalt-phosphate-based electrocatalytic material (Janus H_2-CoCat NP) was developed for HER in a neutral electrolyte.[123] Although with a remarkable catalytic activity, these NPs have to operate under near-neutral conditions.

Cobalt phosphides are suggested to be suitable catalysts for HER–OER.[124–128] In 2014, Popczun and co-workers confirmed that CoP fabricated by means of a two-step colloidal synthesis approach is highly efficient and stable for HER in an acidic medium (Fig. 3(g)). Acting as a cathode in 0.5 M H_2SO_4, CoP NPs (electrodeposited on Ti foil) yielded a current density of -20 mA cm^{-2} at 85 mV (*vs.* RHE) overpotential (Fig. 3(h)) with a stability of 24 h (400 cyclic voltammetric sweeps).[129] Another form

of cobalt phosphide that can serve as a HER electrocatalyst is Co_2P (Fig. 3(i) and (j)).[130] However, this material was revealed to have a larger HER overpotential than CoP. The high Co/P ratio and low Co–P character make it unlikely for Co_2P NPs to enable surficial distribution of conceivable active centers on the catalyst.[131]

Furthermore, following the catalytic efficacy of water splitting electrocatalysts due to the presence of phosphorus, various studies have demonstrated that incorporating metal catalysts with phosphorus can generate highly efficient HER–OER activity.[71,85,132–134] For instance, Wei and co-workers revealed that the catalytic activity of Ni can be tuned with the extent of P deposition with the best activity observed at 10.8 wt% P.[135] Moreover, pioneering studies conducted by our group showed that nickel phosphide (Ni–P) also demonstrated high activity for OER. Here, the authors established that a Ni–P nanoparticle film electrodeposited on Ni foam (Ni–P/NF) achieved a current density of 10 mA cm^{-2} at 1.67 V (*vs.* RHE) with 80 mV and 309 mV overpotentials for HER and OER, respectively, in 1.0 M KOH (Fig. 3(k) and (l)).[85] Other forms of nickel phosphides reported with high catalytic activity include Ni_2P,[136,137] Ni_5P_4[138] and Ni/Ni_8P_3.[139] Most importantly, the Ni_2P nanoarray has been demonstrated to be not only a high-performance non-noble-metal 3D catalyst electrode for hydrazine oxidation reaction (HzOR), but also a bifunctional catalyst material toward more energy-efficient hydrazine-assisted electrolytic hydrogen production.[137]

Aside from the common colloidal synthesis method for fabricating transition metal phosphides (TMPs), a recent surfactant-free low-temperature phosphidation approach by means of topotactic conversion of the corresponding precursors is developed.[140] In this route, the propagation of CoP nanostructures is achieved through the use of conductive substrates to fabricate binder-free HER cathodes. A typical example is the synthesis of porous CoP/CC with a rough surface using low-temperature phosphidation of the smooth-surfaced Co(OH)F/CC precursor. The modified roughness of the surface was attributed to the dehydration and release of gases during the annealing of the precursor. The as-synthesized CoP/CC displayed a remarkable HER performance with an overpotential of 209, 106, and 67 mV (*vs.* RHE) to afford a current density of 10 mA cm^{-2} in alkaline, neutral and acidic media, respectively. The remarkable performance can be partly related to the expedited electron transfer resulting from the improved interfacial contact between CoP and the CC conductive support, alongside the improved exposure of active centers. Similarly, our group reported the fabrication of CoP nanostructures decorated on carbon cloth (CoP/CC) *via* low-temperature phosphidation of the Co(OH)F/CC precursor.[57] When utilized as an electrocatalyst for HER, CoP/CC also displayed a remarkable performance in alkaline and neutral media. Encouraged by the performance of Co and Ni phosphides as bifunctional electrocatalysts and the merits of 3D structured catalysts, our group synthesized Ti-supported FeP nanowire arrays (FeP NA/Ti) to catalyze overall water splitting.[77] The FeP NA served as the active site while Ti acted as the current collector. In an acidic medium, the FeP NA/Ti electrode displayed a low onset overpotential of 16 mV with a Tafel slope of 38 mV dec^{-1} and an

exchange current density of 0.42 mA cm^{-2}. The good acidic stability of FeP NWs is depicted by the negligible changes in the overpotential after 2000 and 3000 cyclictest runs or 15 h of continuous operation. These attributes were related to the structure-induced electronic effect after phosphidation. After phosphidation, the 1D array format of FeP NWs is retained but the lengths and diameters are decreased (up to 600 nm) and increased (50–95 nm), respectively. Similarly, for exploiting the benefits of 3D architectured electrocatalysts, Wang and co-workers developed flexible 3D iron phosphide nanotubes (IPNTs) as a HER electrocatalyst.[141] The prepared compound comprised of FeP coated with NiFeO$_x$/CFP species yielded low onset overpotentials of 31 and 35 mV (vs. RHE) in alkaline and acidic solutions, respectively. Strangely, the in situ fabricated surficial iron oxide/phosphate species assisted the activation of OER with an onset overpotential of 250 mV (vs. RHE). Moreover, when the flexible 3D iron phosphide electrocatalyst was employed in a constructed alkaline electrolyzer, it displayed a good activity with a current density of 10 mA cm^{-2} at only 1.69 V (Fig. 3(m) and (n)).[141] Another synthesis approach is the facile reaction of metal and bimetallic foils with several orga-nophosphine sources to produce TMPs, proposed by Read and coworkers.[142] The as-synthesized phosphides demonstrated outstanding OER and HER activity which compared favorably with samples prepared by means of more costly and elaborate procedures. Another TMP-based material considered as a water splitting electrocatalyst is MoP. Our group developed a closely interconnected network of MoP NPs with high specific surface area (SSA) as illustrated in Fig. 3(o). The synthesis of this microstructure was by a temperature-programmed reduction of the air-calcined precursor obtained from $(NH_4)_6Mo_7O_{24} \cdot 4H_2O$, $(NH_4)_2HPO_4$ and citric acid (CA) with a Mo : P : CA molar ratio of 1 : 1 : 2 (MoP-CA2). The MoP-CA2 NPs displayed a current density of 0.086 mA cm^{-2} with an onset overpotential of 40 mV, a Tafel slope of 54 mV dec^{-1}, and an almost 100% FE (Fig. 3(p)). In addition, a remarkable stability for 4000 cycles (at least 24 h) was maintained.[64] A most compelling feature is that metal phosphides are prone to oxidation and hence their surface turns into an oxide during OER catalysis.[126] This newly formed oxide surface is the one that plays the true role of a catalyst. A recent study by Shifa et al.[143] revealed that Sn doped Ni$_5$P$_4$ in situ transformed into more active Sn$_x$NiO during the OER process. The electrochemically induced oxide is catalyti-cally more active than the pristine oxides as it is formed in the vicinity of conductive phosphide species.

Metal nitrides. Metal nitrides have demonstrated superior HER–OER activities due to their good corrosion resistance and electrical conductivity.[144] Comprehensive studies of this set of electrocatalysts are mostly focused on their intrinsic HER characteristics.[145] Only a few studies have established the potential of metal nitrides to activate the OER.[146] One among such studies is the synthesis of Ni$_3$N nanosheets, which were reported for the first time to be a suitable OER electrocatalyst when compared to NiO nanosheets. The improved intrinsic OER activity was attributed to the enhanced electrical conductivity with

metallic characteristics and atomically disordered structure.[147] On this account, it was suggested that metal nitride nanosheets could serve as bifunctional HER–OER electrocatalysts, where the chemical stability of nitrides deserves special attention in addition to their efficiency.

Despite the recent developments in improving the intrinsic OER behaviour, related studies in this regard, especially for overall water splitting, are limited. This may be related to the high overpotentials resulting from the restricted charge/ion transport. To circumvent this, a rational design to enhance the morphological effect, surface electrochemical reaction and electronic conductivity was proposed by Zhang and co-workers. Here, the authors synthesized Myriophyllum-like TiN@Ni$_3$N nanowire arrays via a chemical bath deposition approach followed by an annealing process as a bifunctional HER–OER electrocatalyst. The as-synthesized TiN@Ni$_3$N nanowire arrays displayed good HER and OER activities, and achieved a water splitting onset of ~1.57 V with a current retention of 63.8% after 16 h of operation.[148]

Compared with single-metal nitrides, specific double metal nitrides have demonstrated better electrocatalytic activity and can be easily optimized by modulating the valence and electronic states of the metal elements.[149,150] Cao and co-workers demon-strated this concept by revealing the enhanced HER activity and stability of cobalt molybdenum nitride (Co$_{0.6}$Mo$_{1.4}$N$_2$) with a nanoscale morphology. Synthesized via a two-step solid-state reaction, Co$_{0.6}$Mo$_{1.4}$N$_2$ possessed a stacked four-layered sequence of mixed close-packed structures with alternating layers of transi-tion metals in octahedral and trigonal prismatic coordination. Owing to this morphology, Co$_{0.6}$Mo$_{1.4}$N$_2$ with a low catalyst loading of 0.24 mg cm^{-2} achieved a current density of 10 mA cm^{-2} at -0.20 V (vs. RHE) under acidic conditions.[149]

Similarly, Jia and co-workers synthesized Ni$_3$FeN nano-particles (Ni$_3$FeN-NPs) by means of thermal ammonolysis of ultrathin NiFe-LDH nanosheets. The as-prepared NPs were highly effective for full water splitting owing to the unique electronic structure of the metallic composite, thereby facilitat-ing charge distribution and H$_2$O adsorption.[151] Moreover, the particle size (100 nm) effect was alleged to boost the accessi-bility of active sites for the water splitting process.

Metal carbides. Similar to metal nitrides, metal carbides (also known as transition metal carbides (TMCs)) have a unique electronic structure, with which catalytic water splitting reac-tions can be accelerated through. Both theoretical and experi-mental verifications of improved electronic characteristics as a result of the hybridization of the d-orbitals of the metal and the sp-orbitals of carbon are provided.[144,145] On this account, the d-band structure is broadened as this favors the hydrogen binding energy, thereby promoting the HER.[145]

Among this class of metals, molybdenum (Mo) and tungsten (W) carbides are so far the most investigated metal carbides for water splitting,[152] with WC being the most stable in acidic solutions.[153] On the other hand, WC, W$_2$C, and Mo$_2$C have similar passivation regions in alkaline/neutral medium. Overall, the stability of these compounds is influenced by the generation

of surface oxide motifs in the considered pH range.[152] Weigert and co-workers demonstrated the superior electrochemical stability of WC foil modified with a low coverage of Pt compared to that of pristine WC.[153] The result showed that the stability of Pt-modified WC was sustained till a potential of ~1.0 V (*vs.* NHE).

Among the different Mo carbides,[145] Mo_2C is the most reported for water splitting and was previously explored as an effective noble-metal free electrocatalyst to replace Pt owing to its similar electronic characteristics to that of Pt and optimal hydrogen-adsorption properties.[100,154,155] One major setback of this compound is its large particle size which acts as a limiting factor for the exposure of its active sites. In addition, the usage of these catalyst systems is challenged by surface oxidation or corrosion.[153] So far, numerous approaches are proposed to promote particle miniaturization, and among those methods, dispersion is considered to be the most effective way to increase the surface area, enrich active sites and promote electron/mass activity. Recently, an enhanced electrocatalytic performance of Mo_2C was demonstrated by embedding Mo_2C nanoparticles in nitrogen-doped carbon nanosheet/graphene ($Mo_2C@N-DC/G$) aerogel films.[156] The carbon nanomaterial has a high surface area which prevents the aggregation of Mo_2C nanocrystals, as well as protects the metal catalysts from acid corrosion, enhances the stability in an acidic medium and simultaneously serves as "electron highways" for rapid electron transfer.[157] Moreover, the heteroatom N dopant modifies the surface chemistry with different defects and alters the electronic structure of the catalysts, leading to optimized adsorption energy of the key intermediates on the surface. The synergistic effect of N-doped carbon nanomaterials and Mo_2C nanoparticles enriched the electron density on the carbon surface and promoted hydrogen adsorption as well as evolution.

In summary, the above discussed studies have evidently shown that the performances of metal-based electrocatalysts (as listed in Table 1) for water splitting are dependent on several key parameters. First, their overall HER–OER activity mostly depends on the structure and specific active surface area of the catalyst system rather than the nature of the constituting metal. This deduction elaborates the importance of morphology engineering and composition towards the optimization of the density and distribution of catalytic active sites. Second, the electrolyte selection, which is also critical to efficiency and stability, is dependent on its ion species, concentration, pH values and the suitability with electrocatalysts. Since the electrolyte would directly affect the reaction kinetics and an inappropriate electrolyte would cause corrosion of the electrode, choosing a suitable electrolyte has a great influence on the performance and stability of the electrocatalysts. Third, the lifetime of a catalyst directly affects its practical application. The economic strategies for catalyst reactivation so as to further extend the shelf life of a catalyst will also play an important role in developing commercializable technologies. Additionally, the cost from material elements, catalyst preparation, electrolytes, and electrodes will decide the upscalability and hence the practicality of this technology. Although non-noble metals are preferred to minimize element cost, noble metals would be still competitive if their cost-effectiveness surpasses non-noble candidates, *i.e.* a tiny amount of noble metals, for example in the monodispersed single-atom catalysts, could enhance catalysis and stability greatly.

2.2.3 Defected functional electrocatalysts. As an alternative to metal-based catalyst systems, defected functional materials with the potential to catalyze HER and OER processes, such as functional carbon materials such as carbon nanotubes/nanofibers[158] and graphene-based nanosheets,[159] have captivated researchers in this field. In addition to the favorable intrinsic catalytic characteristics, functional carbon catalysts display a more exceptional catalytic quality when doped with non-metal heteroatoms.[160] Under this circumstance, the electronic structure of the carbon species is altered with an increase in surface defects, which often act as the catalytic active sites.[161,162] The harmonious effect of the enriched active sites resulting from the doping and the intrinsic properties of the functional carbon materials portrays this catalyst system as a suitable candidate for an energy-saving electrochemical system.

However, the investigation of the bifunctional HER and OER activity on these carbon surfaces is still limited. Therefore, exploring the application of functional carbon-based materials for overall water splitting cannot be over-exaggerated. In this regard, Lai and coworkers first conducted an extensive study on the fabrication of porous graphite nanocarbons co-doped with O, N and P heteroatoms as a self-supported 3D electrode (ONPPGC/OCC) for overall water splitting at various pH values.[163] For instance, in an alkaline medium, ONPPGC/OCC electrocatalysts displayed good HER and OER activities. The electrolyzer attained a current density of 10 mA cm^{-2} at a cell voltage of 1.66 V with remarkable stability. The remarkable electrocatalytic performance of the porous nanocarbon was attributed to the unique 3D structure and pore distribution, highly dispersed active sites, improved transport properties, and good electrical conductivity. Qiao and co-workers presented a 3D-architectured hydrated catalyst NiCo LDH on N-doped graphene hydrogels (NG-NiCo) synthesized through ammonia-involved hydrothermal treatment of a graphene hydrogel followed by heterogeneous deposition of the obtained NiCo hydroxide on NG.[164] While the presence of N-dopant reduces the catalyst's internal resistance and the graphene provides a porous 3D interconnected network, the synergistic metal–O–C and metal–N–C interactions yield interfacial active centers to activate the HER–OER. Undeniably, this study offers a unique exciting means to explore functional carbon compounds as water splitting electrocatalysts. The electrocatalytic performance of ONPPGC/OCC in other media is presented in Table 1.

Another widely used carbon-based material is graphdiyne (GDY), a novel plane carbon network consisting of sp-/sp^2-*co*-hybridized carbon atoms.[182] This porous carbon network with a unique intrinsic band gap, excellent electric conductivity, and strong stability was first synthesized by Li and co-workers in 2010.[183] Given its intrinsic properties, the authors prepared a GDY anchored on CoN$_x$ nanosheets with a seamless interacting

interface on Ni foam (CoN$_x$@GDY NS/NF).[182] When tested in 1.0 M KOH, CoN$_x$@GDY NS/NF attained a current density of 10 mA cm^{-2} with a cell voltage of 1.48 V when employed as a bifunctional electrocatalyst. Similarly, Si and co-workers utilized GDY to develop a hierarchical heterostructure composite with NiFe LDH anchored on copper foam (GDY@NiFe-LDH/CF) to catalyze the overall water splitting.[184] In its function, GDY@NiFe-LDH/CF attained a current density of 20 mA cm^{-2} with a cell voltage of 1.512 V. The remarkable electrochemical performance was credited to the improved interfacial chemical interaction between Fe, Ni and the triple C–C bonds in GDY. This interaction facilitated an improved electron charge distribution with a controlled diffusion rate.[184] In addition, Table 1 presents a summary of other adopted metal-free electrocatalysts.

Benefitting from the synergistic effect of metallic behaviour, interconnected pores of nanowire arrays, and a distinct 3D electrode structure, Co$_4$N porous nanowire arrays on carbon cloth attained a low overpotential of $\sim$0.26 V at 10 mA cm^{-2} and a Tafel slope of 44 mV dec^{-1} in an alkaline medium. Moreover, theoretical evidence shows that the metallic Co$_4$N core with a thin cobalt oxides/hydroxides shell serves as the active centre during the OER process.[146]

In short, defected functional catalysts would still need the metal-based materials for the synergistic catalysis and/or as the supporting template. Besides laterally referenceable perspectives discussed above for metal-based catalysts, the synergy of interface coupling between metal-free and metallic components will play a significant role in enabling an efficient carrier (electrons in HER and holes in OER) transportation within the catalysts, thus affecting the performances.

3. Ammonia synthesis via N$_2$ reduction reaction

Ammonia (NH$_3$) is a commonly synthesized chemical across the world. It can function as a building block for the production of other N-based compounds and as a clean energy carrier due to its high H-content.[185,186] Presently, NH$_3$ is industrially fabricated via the Haber–Bosch process involving an exothermic interaction between N$_2$ and H$_2$ (N$_2$ + 3H$_2$ → 2NH$_3$) in the presence of a catalyst at high pressure and high temperature.[187] Theoretically, compared with Fe-based catalysts, Ru-based catalysts are more effective to operate the Haber–Bosch process under a relatively mild condition (pressure $\leq$ 100 bar).[188] Despite this, the thermodynamics is still low (approximately 10–15%) with an energy implication estimated at 1–2% of global annual energy[186,189] and the involvement of H$_2$ in this process is undermined by the consumption of fossil fuels (with sizeable CO$_2$ emissions).[190]

Recently, electrocatalytic N$_2$ reduction reaction (NRR) is viewed as an energy-saving approach for NH$_3$ production, as the process of synthesizing NH$_3$ is carried out under ambient temperature and pressure. Hence, electrocatalytic NRR is considered as an eco-friendly and energy-conservation approach for NH$_3$ synthesis. However, its practical application is still constrained by the costly electrolytes, low NH$_3$ yields and so on.[188] On this account, a knowledge-driven guide towards the development of efficient electrocatalysts is a fundamental step for realizing electrocatalytic N$_2$ fixation and accelerated NRR processes. Characteristically, NRR electrocatalysts are of three types: biocatalysts, homogeneous, and heterogeneous. The biocatalysts and homogeneous electrocatalysts contain ligand-surrounded metal centers,[191] which poses a limitation due to the high cost of the ligands. Synthesis challenges as well as the low electrical properties hinder the development of these types of catalysts.[192] On the other hand, heterogeneous electrocatalysts are highly durable and are more integrable with functional energy conversion devices.[193] On this account, the design and development of heterogeneous electrocatalysts have been exploited for NH$_3$ synthesis.

In this review, recent experimental and theoretical insights into the development of NRR electrocatalysts are highlighted. Particular emphasis will be devoted to the significance and implications of recent developments. First, the electrochemical NRR mechanisms are discussed, providing idealistic modalities for enhancing catalytic activity, selectivity and stability. Based on these mechanisms, various heterogeneous electrocatalysts are reviewed in terms of catalytic performance, reflecting different accumulated outcomes and mechanistic understanding of catalyst design principles. Here, electrocatalysts including metal (noble and non-noble) catalysts and metal-free catalysts are discussed.

3.1. Electrochemistry of N$_2$ reduction reaction (NRR)

3.1.1. Fundamentals of NRR.
Generally, the electroreduction of nitrogen on a heterogeneous catalyst involves two major reaction mechanisms: dissociative and associative (Fig. 4). The dissociative mechanism involves breaking of the N≡N bond of the N$_2$ molecule to form N-adatoms on the surface of the catalyst prior to the protonation process. Subsequent protonation of the adatoms on the surface results in the yield of NH$_3$ independently. Fig. 4(a) presents a detailed schematic representation of the mechanistic pathway, with a characteristic ΔG plot to illustrate the minimum energy pathway (MEP) on the Ru NP catalyst (Fig. 4(b)).[194] Deductions from the mechanistic pathway and the characteristic ΔG plot suggest that the last reduction step (*NH$_2$ + H$^+$ + e$^-$ → *NH$_3$, $\Delta\Delta G$ = 0.32 eV uphill) is the rate-determining step.[195] On the other hand, in the associative mechanism, the two N centers in N$_2$ remain intact as a molecule while being protonated, with the release of NH$_3$ after the severance of the N–N bond (Fig. 4(c)). This mechanism is further characterized based on the order of protonation of the two N centers (with the assumption that the N$_2$ molecule is adsorbed on the catalyst). The protonation sequence and its associated energies will dictate the rate-determining reaction on the catalyst surface. Fig. 4(d) illustrates that the first reduction process (*N$_2$ + H$^+$ + e$^-$ → *N$_2$H, ΔG = 1.03 eV uphill) is the rate-determining step of the associative reaction on the Ru NP catalyst.[194]

Generally, protonation of the N centers occurs via two routes in the associative reaction. In the first instance, the N center
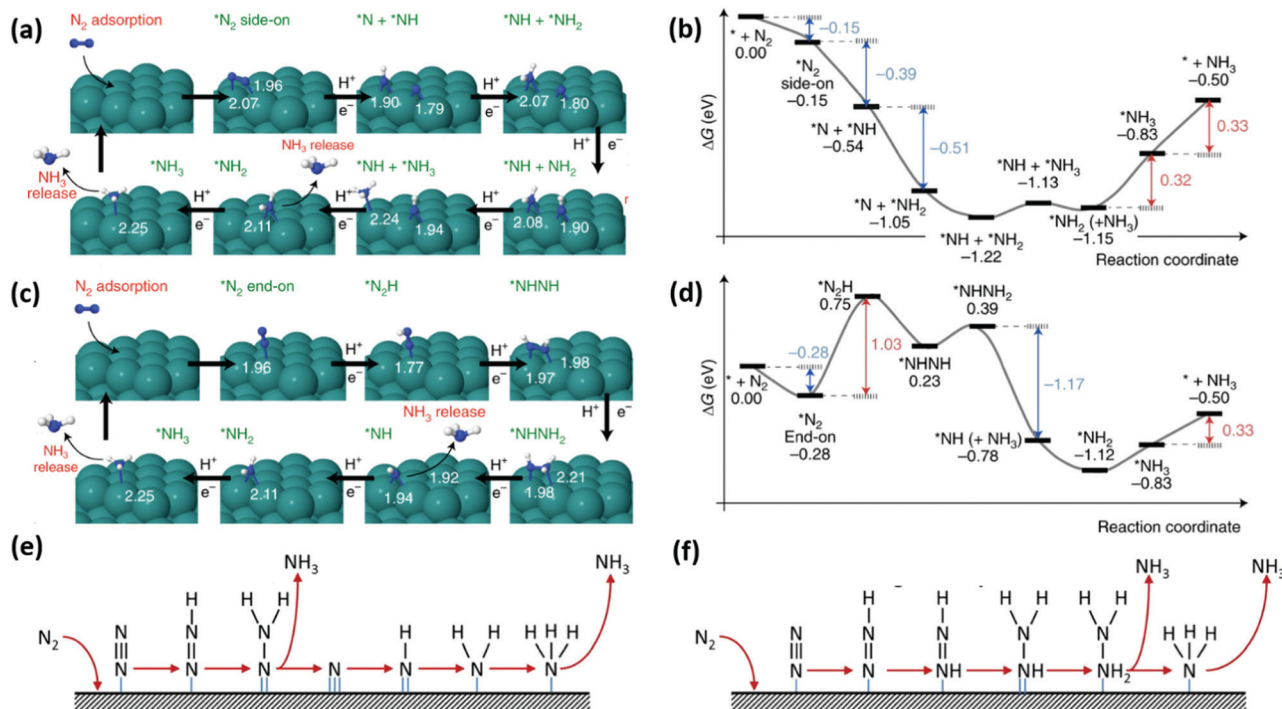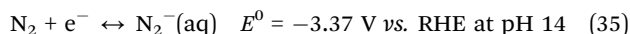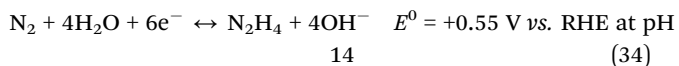
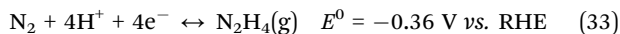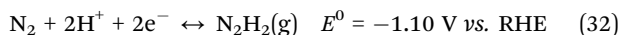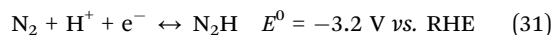**Fig. 4** NRR mechanisms on heterogeneous catalysts. (a) Dissociative mechanism and its (b) characteristic Gibbs free energy plot illustrating the minimum energy pathway on Ru nanoparticles (Ru-NPs). (c) Associative mechanism and its (d) characteristic Gibbs free energy plot illustrating the minimum energy pathway on Ru nanoparticles (Ru-NPs). Images (a)–(d) are reproduced with permission.[194] Copyright 2019, *Nat. Catal.* Comparison of (e) distal and (f) alternative associative mechanisms. Images (e) and (f) are reproduced with permission.[196] Copyright 2017, Elsevier.

farther from the catalyst surface is preferentially protonated (assuming an end-on coordination mode for the N_2 molecule) resulting in the yield of NH_3 and formation of a metal nitride (M–N) motif, which is later protonated to yield the second equivalent NH_3. This is classified as the distal associative pathway (Fig. 4(e)). On the other hand, the alternative route relates to the protonation of each N center alternately until an N center is completely hydrogenated to NH_3 and the N–N bond is severed (Fig. 4(f)).[196]

In both dissociative and associative mechanisms, electrochemical NRR involves a series of proton–electron transfer steps with the formation of multiple intermediates:[197]
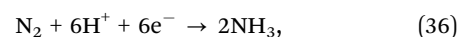
$$N_2 + H^+ + e^- \leftrightarrow N_2H \quad E^0 = -3.2 \text{ V } vs. \text{ RHE} \quad (31)$$

$$N_2 + 2H^+ + 2e^- \leftrightarrow N_2H_2(g) \quad E^0 = -1.10 \text{ V } vs. \text{ RHE} \quad (32)$$

$$N_2 + 4H^+ + 4e^- \leftrightarrow N_2H_4(g) \quad E^0 = -0.36 \text{ V } vs. \text{ RHE} \quad (33)$$

$$N_2 + 4H_2O + 6e^- \leftrightarrow N_2H_4 + 4OH^- \quad E^0 = +0.55 \text{ V } vs. \text{ RHE at pH } 14 \quad (34)$$

$$N_2 + e^- \leftrightarrow N_2^-(aq) \quad E^0 = -3.37 \text{ V } vs. \text{ RHE at pH } 14 \quad (35)$$

It can be deduced that in a neutral solution (pH = 0), reactions (31) and (32) are the most negative than H^+ reduction ($E^0 = 0$ V *vs.* SHE at pH = 0),[197] which implies that it is more difficult to form N_2H and N_2H_2 intermediates. However, in a strong alkaline solution (pH = 14), it is likely that reactions (31) and (35) will occur simultaneously, thus, limiting the formation of the intermediate N_2H. Besides, the lower redox potentials of the

$4e^-$-reduction (reaction (33)) and $6e^-$-reduction (reaction (34)) paths when compared to the $1e^-$-reduction and $2e^-$-reduction paths result from the weak bond strengths of the second and third bonds of the N_2 molecule. To date, a generally acceptable NRR mechanism is yet to be thoroughly elaborated upon due to the intricacies involving the formation of multiple intermediates and multi-step electron/proton transfer. Naturally, the NRR is achieved by means of nitrogenase enzymes in a contrary process to the Haber–Bosch process. One of the most reported nitrogenases are the FeMo nitrogenases[198] with the NRR undergoing an associative mechanism (with the N_2 molecule coordinating to a metal centre in the FeMo nitrogenase in the end-on mode). However, this is still highly debated to this day.[199]

Irrespective of the operating mechanism, it is evident that these enzymes are suitable catalysts for NH_3 production under ambient conditions in aqueous media with an exciting energy efficiency. Consequently, electrochemistry has appeared as an attractive approach adopting the HER of the water splitting process to produce H^+ and e^- for the reduction of nitrogen (from air). Renewable energy sources are also suitable to power the reaction operation. Similar to the water splitting process, the NRR mechanism also depends on the nature of the electrolyte. Depending on the nature of the electrolyte, the general reactions are as follows:

In an acidic condition:

At the cathode:

$$N_2 + 6H^+ + 6e^- \rightarrow 2NH_3, \quad (36)$$

At the anode:

$$3H_2O \rightarrow 3/2O_2 + 6H^+ + 6e^- \qquad (37)$$
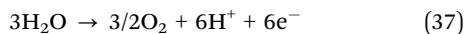
In an alkaline condition:

At the cathode:

$$N_2 + 6H_2O + 6e^- \rightarrow 2NH_3 + 6OH^- \qquad (38)$$

At the anode:

$$6OH^- \rightarrow 3/2O_2 + 3H_2O + 6e^- \qquad (39)$$

Overall reaction:

$$N_2 + 3H_2O \rightarrow 3/2O_2 + 2NH_3 \qquad (40)$$
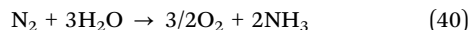
Firstly, the carbon footprint in the generation of ammonia is minimized. In addition, exploiting the intrinsic characteristics and flexibility of an electrochemical system increases the potential of pilot/large-scale NH_3 synthesis. Moreover, feasibility studies on a pilot scale are necessary for the successful commercialization of this process. From a techno-economic standpoint, the electrochemical NRR process saves more energy with an estimated 20% increased energy efficiency compared to the Haber–Bosch scheme, considering coal as the source of hydrogen.[200] However, this potential might be challenged by the limited depth of material knowledge and scale-up dynamics of current catalyst-development strategies.

3.1.2. Recent theoretical insight into NRR. Recently, the electrosynthesis of ammonia has been extensively supported fr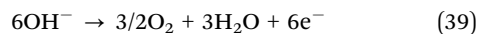om a theoretical perspective. Most importantly, these studies focus on material discovery for suppressing the HER process in favor of N_2 protonation.[195] With this issue under consideration, it is important to review related theoretical studies towards future schemes to enhance electrochemical NRR and retardation of the HER process.

A milestone study utilizing computational SHE via harmonic approximation and DFT calculations to investigate the reduction energetics for N_2 (ad-molecules and adatoms) on different transition metal surfaces in an acidic medium was conducted by Nørskov and co-workers in 2012.[201] By correlating the chemisorption energies with the reaction intermediates under the assumption that the change in free energy is proportional to the activation energy barrier in each elementary step, a volcano plot was obtained. The segmentation of the volcano plot into right and left legs indicates that the metals on each leg possess a weak and a strong N-binding energy, respectively. For instance, the metals on the left-leg (Sc, Y, Ti and Zr) have strong affinity for N-adatoms, which will facilitate significant synthesis of NH_3 relative to H_2, particularly at a bias of -1 V to -1.5 V (vs. SHE). At the top of the volcano plot are the most active metals for ammonia synthesis, which include Mo, Fe, Rh, and Ru. However, the faradaic efficiency (FE) of these metals is low owing to the substantial HER competition.[201] Also, the authors revealed that the defect-free surfaces of TMs are catalytically more active for NH_3 formation than their stepped counterparts due to the lower onset potential on the close-packed flat surfaces compared to the stepped surfaces.[201]

Generally, the production of NH_3 is simply catalyzed by pure transition metals (TMs). Still, the N-adsorption energies (ΔE) of these metals are insufficient relative to the ideal values within the range of -0.4 eV to -1.4 eV.[202] Contrarily, some early TMs (including Sc, Y, Ti and Zr) have displayed strong N-bonding within the bias range of -1 V to -1.5 V (vs. SHE). Nonetheless, these early TMs change their phase from metallic state to bulk nitrides, which hinders the potential of N_2 activation due to the widened d-band centers from the Fermi level.[202] For example, utilizing iron catalysts in NH_3 production gives rise to the formation of a Fe_4N-like structure, although it is unsure if the N-species is an ad-molecule or adatom.[203]

Pertaining to boosting the reduction of N_2 while simultaneously suppressing the HER process, Li and co-workers proposed an electron-deficient approach to retard the HER process in an alkaline medium under ambient conditions. Here, the authors boosted the NRR performance of Cu NPs with negligible catalytic activity via a local electron depletion effect using Mott–Schottky rectifying contact with a polyimide support. The electron-depleted Cu NPs considerably enhanced N_2 pre-adsorption leading to a better NH_3 yield. This approach of inciting an electron deficient surface offers a novel insight into the rational design of inexpensive NRR catalyst systems with high activity and selectivity.[204]

Moreover, early TMs are readily oxidized to form their respective oxides in their natural state which may alter their catalytic efficacy.[205] On this account, the performance of TM oxides was theoretically investigated towards electrosynthesis of NH_3 under ambient conditions. Skúlason and co-workers studied the potential of TM dioxides as NRR electrocatalysts and revealed that the (110) planes of ReO_2, NbO_2, and TaO_2 are the best suited for NH_3 synthesis given their reasonably low onset potentials of -0.57 V, -1.07 V and -1.21 V (vs. SHE), respectively.[206] The least overpotential was exhibited by IrO_2 (-0.36 V) but this catalyst preferentially adsorbs H-adatoms which will favor the HER process.[206]

Lately, the possible production of NH_3 using NbO_2 NPs as an electrocatalyst has been experimentally proven under ambient conditions.[207] This possibility is accredited to the electronic characteristics of NbO_2 which are alleged to promote NH_3 fixation.[188] Owing to the nature of Nb^{4+}, NbO_2 NPs possess an empty d-orbital that readily accepts electrons leading to a strong surficial bonding with N_2. In addition, the activation of N-admolecules/adatoms could be promoted by the back donation of the single d-electron from the Nb^{4+} cation. In this respect, the NbO_2 NPs attained an NH_3 yield rate of 11.6 μg h^{-1} mg$^{-1}_{cat.}$ with an FE of 32% at -0.60 (vs. RHE) and -0.65 (vs. RHE), respectively, when tested in a 0.05 M H_2SO_4 solution.[208] Similarly, other forms of niobium oxides have also shown potential applications as possible NRR electrocatalysts.[209,210] For example, our group demonstrated the effectiveness of Nb_2O_5 as an electrocatalyst for NH_3 production as both nanofibers[209] and nanowires.[210]

Nevertheless, metals have shown good potential for N_2 reduction under ambient conditions; it is worthwhile to mention that some metals and their respective oxides do not display

similar catalytic efficacy particularly at room temperature. This is somewhat related to their low conductivity[192] and in other cases, it is due to their strong affinity for hydrogen.[202] For the latter, typical examples are the late TMs which greatly enable the HER, thereby fettering the formation of NH_x intermediates.[202] Unlike these metals, some metals especially the middle TMs offer moderate binding energies for N-motifs, thus making them suitable candidates for N_2-to-NH_3 conversion.[211] Proceeding from this, it is likely that the best suited electrocatalyst can be designed by selecting the right materials with intrinsic NRR characteristics. Otherwise, it is necessary to adopt measures to promote the NRR performance of the catalyst system.

An effective scheme is to incorporate a second active center to facilitate the mechanistic spillover and hydrogenation of the activated N-motifs from the metal surface. For instance, Wang and co-workers proposed the use of LiH as a second active center to disrupt the NRR pathway on a TM or its nitride (TMN) by spilling over the activated N-motifs to its surface for direct hydrogenation. LiH is a powerful reducing agent which offers immediate H-species to bind with N-motifs to yield $LiNH_2$. Subsequently, $LiNH_2$ heterolytically splits to release H_2 and NH_3 with the regeneration of LiH. It should be emphasized that this rational scheme is an approach to improve the NRR performance of early and late 3d TMs under ambient conditions.[202] However, in realistic terms, the two active centers need to be appropriately separated.

Alternatively, HER-retarding strategies are equivalently being suggested for a successful headway in the NRR process. In this regard, a common approach is the use of electrocatalysts other than pure metals. The introduction of non-metal species on metals has shown remarkable results pertaining to NH_3 synthesis. A recent theoretical study involving metal nitrides as NRR electrodes suggests that VN and ZrN produced NH_3 at potentials of -0.51 V (vs. NHE) and -0.76 V (vs. NHE), respectively. These results were unachievable when the nitrides were veiled with H-adatoms.[205] Similarly, Abghoui and co-workers reported a parallel result for NbN and CrN.[212]

To date, there are no extensive computational and experimental studies investigating the efficacy of metal nitrides as catalysts for N_2-to-NH_3 conversion. However, Simonov and co-workers critically assessed the electrocatalytic activity of VN and Nb_4N_5 anchored on CC under various conditions.[213] Here, the authors concluded that polycrystalline VN and Nb_4N_5 are electrocatalytically inactive toward NH_3 synthesis regardless of the operating condition. Another related study involved the computational investigation of single TMs anchored on boron nitride (TM-BN) as a N_2 fixation electrocatalyst.[193] Of the investigated single TMs (Sc to Zn, Mo, Ru, Rh, Pd, and Ag), the highest electrocatalytic activity was witnessed on the defective Mo-BN nanosheet with a low overpotential of 0.19 V. The high spin-polarization, selective N_2H^*-motif stabilization and NH_2^*-motif destabilization are attributed for the high catalytic activity of the Mo-BN nanosheet for N_2-to-NH_3 conversion.[193]

Equally, it will be beneficial if similar theoretical studies are conducted on binary nitrides. For instance, Co_3Mo_3N is one the most active electrocatalysts for NH_3 synthesis[214] and was recently modeled for the conventional Haber–Bosch process.[215] On a broader perspective, extensive theoretical studies are required to understand the NRR mechanism over the numerously designed electrocatalysts. Despite the countless NRR electrocatalysts proposed from laboratory tests, their current status is still unclear due to the lack of in-depth theoretical studies. These studies, although limited, are mandatory for a thorough comprehension of the reaction mechanism. Even though DFT computations may suffice as a good theoretical approximation of the catalytic activity, kinetics and evaluation of the optimization scheme, the findings may not be precise experimentally. Therefore, the need for a thorough assessment of NRR electrocatalysts, supported by both experimental and theoretical studies, is crucial.

3.2. Electrocatalysts for NRR

An important milestone in NH_3 electrosynthesis was the establishment of NH_3 production in aqueous solution under ambient conditions from N_2 and H_2 via a back-to-back cell configuration by Furuya and Yoshiba in 1990.[14] Of the 26 cathodes studied, ZnSe was the most suitable for the reduction of N_2 with an NH_3 electrode area-normalized yield rate of 0.23 mol h^{-1} m^{-2}, attaining an FE of 1.3% at a potential of -1 V (vs. RHE).[14] Despite the high yield rate, the FE is relatively low and was attributed to the predominant cathodic reduction of H_2O at the high negative cell potential, particularly in an aqueous solution where the concentration of H_2O is relatively high. For this reason, the suppression of the HER is considered by most to be the utmost challenge confronting electrochemical NRR.

Moreover, the determination of N_2 production in NRR is more challenging than H_2 or O_2 production in water splitting due to the possible contamination from the ambient environment and low production rates.[216,217] Concretely, the ammonia detected may come from other routes beyond the NRR, such as ammonia contamination in the feeding gas, electrolyte and electrode surface, and decomposition or desorption from the catalyst itself, especially in the case of N-containing materials.[218] Thus, it is essential to measure and prove the reliability of obtained data of NH_3 amount. Suryanto, MacFarlane and co-workers[194] summarized the current steps and mis-steps towards NRR in terms of experimental methodology and catalyst selection, and proposed a protocol for rigorous experimentation. They discussed the protocols of NRR experiments in detail and proposed a five-step experimental protocol including gas purification, open circuit control measurements and parallel control experiments by ^{15}N-isotopic labelling experiments to exclude the ammonia contamination or catalyst decomposition issues for reliable proof of the occurrence of the electrochemical nitrogen reduction reaction drawing on Greenlee and co-workers.[216] A similar rigorous experimental protocol consisting of standardized control experiments and quantitative isotope measurements with ^{15}N gas is also proposed by Tang and Qiao[219] based on the Nature published, Chorkendorff and colleague's landmark study about the "true or false" issue in the electrochemical NRR research community in 2019.[220]

In this regard, only with careful validation of the nitrogen source can we evaluate the NRR performance of potential

Table 2 Summary of the performances of NRR electrocatalysts

Electrocatalysts	Electrolyte	NH$_3$ yield	FE (%)	Overpotential (V) vs. RHE	Ref.
Noble metals					
Ag film	0.1 M Na$_2$SO$_4$	1.27 µg h^{-1} cm^{-2}	7.36	−0.6	244
Ag nanosheets	0.1 M HCl	2.83 µg h^{-1} cm^{-2}	4.8	−0.6	232
Au flowers	0.1 M HCl	25.57 µg h^{-1} mg$^{-1}_{cat}$	6.05	−0.2	351
Au/TiO$_2$	0.1 M HCl	21.4 µg h^{-1} mg$^{-1}_{cat}$	8.11	−0.2	352
a-Au/CeOx-RGO	0.1 M HCl	8.3 µg h^{-1} mg$^{-1}_{cat}$	10.1	−0.2	353
Porous Au film on Ni foam	0.1 M Na$_2$SO$_4$	9.42 µg h^{-1} cm^{-2}	13.36	−0.2	226
Pd/C	0.1 M PBS	4.5 µg h^{-1} mg$^{-1}_{cat}$	8.2	0.1	228
Rh NPs/C	0.5 M Na$_2$SO$_4$	22.82 ± 1.49 µg h^{-1} mg$^{-1}_{cat.}$	∼0.1	−0.45	231
Rh$_2$Sb RNRs/C		228.85 ± 12.96 µg h^{-1} mg$^{-1}_{cat.}$	∼1.5		
Rh$_2$Sb SNRs/C		63.07 ± 4.45 µg h^{-1} mg$^{-1}_{cat.}$	∼0.4		
Ru$_1$ on N-doped carbon	0.05 M H$_2$SO$_4$	120.9 µg h^{-1} mg$^{-1}_{cat}$	29.6	−0.2	315
Non-noble metals					
Metallic substances					
Fe SA-N-C	0.1 M KOH	7.48 µg h^{-1} mg$^{-1}_{cat}$	56.55	0	354
Mo$_1$ on N-doped porous carbon	0.1 M KOH	34.0 ± 3.6 µg h^{-1} mg$^{-1}_{cat.}$	14.6 ± 1.6	−0.3	355
Metal oxides					
B-doped TiO$_2$	0.1 M Na$_2$SO$_4$	14.4 µg h^{-1} mg$^{-1}_{cat.}$	3.4	−0.8	274
C-TiO$_2$ nanoparticles	0.1 M Na$_2$SO$_4$	16.22 µg h^{-1} mg$^{-1}_{cat.}$	1.84	−0.7	273
Fe$_2$O$_3$	1.0 M KOH	0.46 µg h^{-1} cm^{-2}	6.04	−0.074	260
Fe$_2$O$_3$ nanorods	0.1 M Na$_2$SO$_4$	15.9 µg h^{-1} mg$^{-1}_{cat.}$	0.94	−0.8	265
Fe$_2$O$_3$/TiO$_2$	1.0 M KOH	16.52 µg h^{-1} mg$^{-1}_{cat.}$	0.31	−0.577	356
Nb$_2$O$_5$ nanowire array	0.1 M Na$_2$SO$_4$	9.67 µg h^{-1} cm^{-2}	2.26	−0.6	210
NbO$_2$ nanoparticles	0.05 M H$_2$SO$_4$	11.6 µg h^{-1} mg$^{-1}_{cat.}$ (−0.65 V vs. RHE)	32 (−0.6 V vs. RHE)	—	208
TiO$_2$ nanosheet array	0.1 M Na$_2$SO$_4$	5.62 µg h^{-1} cm^{-2}	2.5	−0.7	283
TiO$_2$-rGO	0.1 M Na$_2$SO$_4$	15.13 µg h^{-1} mg^{-1}	3.3	−0.9	272
Defective TiO$_2$ on Ti mesh	0.1 M HCl	7.59 µg h^{-1} cm^{-2}	9.17	−0.15	284
Fe/Fe$_3$O$_4$	0.1 M PBS	0.19 µg h^{-1} cm^{-2}	8.29	−0.3	267
FeOOH QDs-GS	0.1 M LiClO$_4$	27.3 µg h^{-1} mg$^{-1}_{cat.}$	14.6	−0.4	262
Metal chalcogenides					
CoS$_2$/NC	0.1 M HCl	17.45 µg h^{-1} mg$^{-1}_{cat.}$	4.6	−0.15	357
Fe$_3$S$_4$	0.1 M HCl	75.4 µg h^{-1} mg$^{-1}_{cat.}$	6.45	−0.4	358
Metal carbides					
Mo$_2$C nanorod	0.1 M HCl	95.1 µg h^{-1} mg$^{-1}_{cat.}$	8.13	−0.3	294
Mo$_2$C/C	0.5 M LiClO$_4$	11.3 µg h^{-1} mg$^{-1}_{cat.}$	7.8	−0.3	277
Ti$_3$C$_2$T$_x$ (T = F, OH) MXene nanosheets	0.1 M HCl	20.4 µg h^{-1} mg$^{-1}_{cat.}$	9.3	−0.4	270
Metal nitrides					
Fe–N/C hybrid	0.1 M KOH	34.83 µg h^{-1} mg$^{-1}_{cat.}$	9.28	−0.2	359
VN nanosheet array	0.1 M HCl	5.14 µg h^{-1} cm^{-2}	2.25	−0.5	297
VN nanoparticles	0.05 M H$_2$SO$_4$	20.2 µg h^{-1} cm^{-2}	6	−0.1	278
Metal phosphides					
CoP/CNs	0.1 M Na$_2$SO$_4$	48.9 µg h^{-1} mg$^{-1}_{cat.}$	8.7	−0.4	279
Ni$_2$P/N,P-C	0.1 M KOH	90.1 µg h^{-1} mg$^{-1}_{cat.}$	19.82	−0.2	280
	0.1 M HCl	34.4 µg h^{-1} mg$^{-1}_{cat.}$	17.21	—	
FeP$_2$ NP-rGO	0.5 M LiClO$_4$	35.26 µg h^{-1} mg$^{-1}_{cat.}$	21.99	−0.4	299
Metal-free electrocatalysts					
Defect-rich carbon cloth	0.1 M Na$_2$SO$_4$ 0.02 M H$_2$SO$_4$	15.9 µg h^{-1} cm^{-2}	6.92	−0.3	304
N-Doped highly disordered carbon	0.1 M KOH	57.8 µg h^{-1} cm^{-2}	10.2	−0.3	310
N and B co-doped carbon nanosheets	0.1 M HCl	7.75 µg h^{-1} mg$^{-1}_{cat.}$	13.79	−0.3	326
Oxygen-doped hollow carbon microtubes	0.1 M HCl	25.12 µg h^{-1} mg$^{-1}_{cat.}$	9.1	−0.8	324
Oxygen-doped carbon nanosheet	0.1 M HCl	20.15 µg h^{-1} mg$^{-1}_{cat.}$	4.97	−0.6	300
Polymeric carbon nitride	0.1 M HCl	8.09 µg h^{-1} mg$^{-1}_{cat.}$	11.59	−0.2	311
S-Doped carbon nanospheres	0.1 M Na$_2$SO$_4$	19.07 µg h^{-1} mg$^{-1}_{cat.}$	7.47	−0.7	360
P-Doped graphene	0.5 M LiClO$_4$	32.33 µg h^{-1} mg$^{-1}_{cat}$	20.82	−0.65	306
S-Doped graphene	0.1 M HCl	27.3 µg h^{-1} mg$^{-1}_{cat.}$ (−0.8 V vs. RHE)	11.5 (−0.6 V vs. RHE)	—	274
Elementals and their compounds					
B-Doped graphene	0.05 M H$_2$SO$_4$	9.8 µg h^{-1} cm^{-2}	10.8	−0.5	316
B$_4$C/CPE	0.1 M HCl	26.57 µg h^{-1} mg$^{-1}_{cat.}$	15.95	−0.75	328
Boron nitride (mesoporous)	0.1 M Na$_2$SO$_4$	18.2 µg h^{-1} mg$^{-1}_{cat.}$	5.5	−0.7	314
Black phosphorus nanosheets	0.01 M HCl	31.37 µg h^{-1} mg$^{-1}_{cat.}$ (−0.7 V vs. RHE)	5.07 (−0.6 V vs. RHE)	—	330

catalysts. Several key parameters related to the performance of the NRR, including electrolyte, ammonia formation rate (NH$_3$ yield), faradaic efficiency and overpotential (V) vs. RHE of reported catalysts for NRR, are listed in Table 2. It should be

pointed out that since the accuracy of the determinate NRR efficiency highly relies on the meticulous measurement of NH_3 amount and well controlled NRR experiments, it is necessary to refer to the original work and confirm the experimental protocols. A second party inspection of the results by using a well-accepted standard protocol will be helpful to filtrate the catalysts with reliable efficiency.

Furthermore, among the various research advances in electrochemical NRR, lithium-mediated nitrogen reduction has attracted much interest as it has been proven to be a good method to electrochemically synthesize ammonia in the past several years.[221] The lithium-mediated nitrogen electroreduction also demonstrated good reproducibility[219] but the process has so far been unstable, and the continuous deposition of lithium limits its practical applicability. The underlying mechanism of lithium-mediated NRR needs to be further investigated to ultimately contribute to green ammonia production and a sustainable society. Hence, the development of electrocatalysts for this purpose is crucial towards an effective NRR with high NH_3 yield.

3.2.1. Noble metal-based electrocatalysts

Au-Based electrocatalysts. Noble metal-based materials, as effective NRR electrocatalysts, have the potential for surficial interaction with N_2 through electron transfer, which is required to promote N_2-fixation.[222] Gold (Au)-based materials, having one of the most stable metallic configurations, are targeted as NRR electrocatalysts owing to their low HER activity. Under this circumstance, electrochemical fixation of N_2 is promoted,[223] although theoretical studies dispute this claim.[206,224] Yan and co-workers demonstrated the potential of a Au-based material (tetrahexahedral (THH) Au nanorods) as a heterogeneous NRR electrocatalyst under ambient conditions. Here, a stepped (730) facet (consisting of (210) and (310) sub-facets) of THH Au nanorods at room temperature and pressure yielded 1.648 $\mu g\ h^{-1}\ cm^{-2}$ of NH_3 and 0.102 $\mu g\ h^{-1}\ cm^{-2}$ of $N_2H_4 \cdot H_2O$ with a high FE (4.02%) at −0.2 V (*vs.* RHE) (Fig. 5(a) and (b)).[223] It was suggested that the stepped facets outperformed the flat planes due to the availability of more catalyst active sites for the adsorption and activation of N_2.[225]

To promote access to more active sites and enhance the NH_3 yield rate and selectivity, porous Au materials are suggested.[226] Wang and co-workers employed a micelle-assisted electrodeposition approach to directly synthesize a porous Au film on Ni foam as an NRR electrocatalyst. In 0.1 M Na_2SO_4 under ambient conditions, the porous Au film presented an NH_3 yield rate of 9.42 $\mu g\ h^{-1}\ cm^{-2}$ and an FE of 13.36% at −0.2 V (*vs.* RHE).[226] Nazemi and co-workers engineered hollow Au nanocages (Fig. 5(c)) of various pore size/density and Au content for the electrochemical synthesis of NH_3. It was demonstrated that the 715 nm pore size (38.3 Au-wt%) displayed the optimal performance with an NH_3 yield rate of 3.9 $\mu g\ cm^{-2}\ h^{-1}$ and a large FE of 30.2% (Fig. 5(d)). The observed improvement in catalytic activity is attributable to the nanoscale confinement of N_2 near the catalyst surface.[227]

Pd-Based electrocatalysts. Nowadays, neat palladium (Pd) has been argued to be not suitable as a catalyst for N_2-to-NH_3

conversion owing to the preferential affinity for hydrogen than nitrogen resulting in the hindrance of N_2 adsorption.[30] To circumvent this, strategic schemes to suppress the HER are advised. One of the strategies is adopting a hydrogen spillover phenomenon whereby the H-species are adsorbed on the catalyst and then spilled over to the adsorbed N_2 for hydrogenation to occur. By doing so, the kinetics for N_2-to-NH_3 conversion will be accelerated. Accordingly, hydrides were suggested with the potential of boosting surface N_2 hydrogenation *via* a hydrogen transfer mechanism.[234,235] However, the formation of Pd-hydrides requires the use of highly reducing agents which could result in difficult formation of hydrides.[236] In this case, studies have investigated the use of electrides as an alternative approach. Electrides are ionic compounds known for their ease of electron donation. Under this circumstance, their usage will provide electrons for the adsorbed N_2 while trapping excess electrons to produce the hydride.

Xin and co-workers highlighted this effect using Pd nanoparticles on a carbon black support (Pd/C), which can generate Pd-hydrides under specific potentials (Fig. 5(e) and (f)).[228] This mechanism allowed for the effective suppression of HER in 0.1 M PBS and hence facilitated the Grotthuss-like hydride transfer mechanism on α-PdH for the hydrogenation of N_2. The beneficial effect of PBS in promoting N_2 hydrogenation at −0.05 V (*vs.* RHE) (yield rate = 4.9 $\mu g\ h^{-1}\ mg^{-1}_{Pd}$) is twice the yield from 0.05 M H_2SO_4 (2.5 $\mu g\ h^{-1}\ mg^{-1}_{Pd}$) and 0.1 M NaOH (2.1 $\mu g\ h^{-1}\ mg^{-1}_{Pd}$). The controlled potential electrolysis on the Pd/C nanoparticles resulted in an NH_3 yield rate of ∼4.5 $\mu g\ h^{-1}\ mg^{-1}_{Pd}$ and a FE of 8.2% at 0.1 V (*vs.* RHE) (at a low overpotential of 56 mV), outperforming Au and Pt catalysts.[228]

Moreover, Pd catalysts can be modified for N_2-to-NH_3 transformation by integrating with other metals to produce alloys. For highly effective catalyst systems, Jacobsen and co-workers proposed the rational approach of forming alloys with elements from the different sides of the volcano plot. Specifically, integrating a metal with strong N_2 affinity with another with weak affinity is more likely to yield optimum ammonia synthesis.[237] On this account, Yan and co-workers developed an amorphous PdCu nanocluster on rGO for catalyzing NH_3 synthesis[229] based on the characteristics of amorphous Cu to promote the hydrogen-spillover mechanism.[238] In addition to the excellent electron transport property of rGO, this support promotes the dispersion and even distribution of the alloy nanoparticles, thereby preventing particle agglomeration (Fig. 5(g)). Based upon the above principle, the optimal $Pd_{0.2}Cu_{0.8}$ alloy nanoparticles significantly outperformed the individual components and displayed an NH_3 yield rate of 2.80 $\mu g\ h^{-1}\ mg^{-1}_{cat.}$ with a low FE of about 0.8% at −0.2 V (*vs.* RHE) in 0.1 M KOH (Fig. 5(h)).[229]

Ru-Based electrocatalysts. Ruthenium (Ru) is an exceptional catalyst for the synthesis of NH_3 *via* the conventional Haber–Bosch process.[239] Theoretically, it is revealed that Ru displays a lower N_2 adsorption energy and overpotential under both associative and dissociative mechanisms than other noble metals in the electrocatalytic synthesis of NH_3. Similar to other
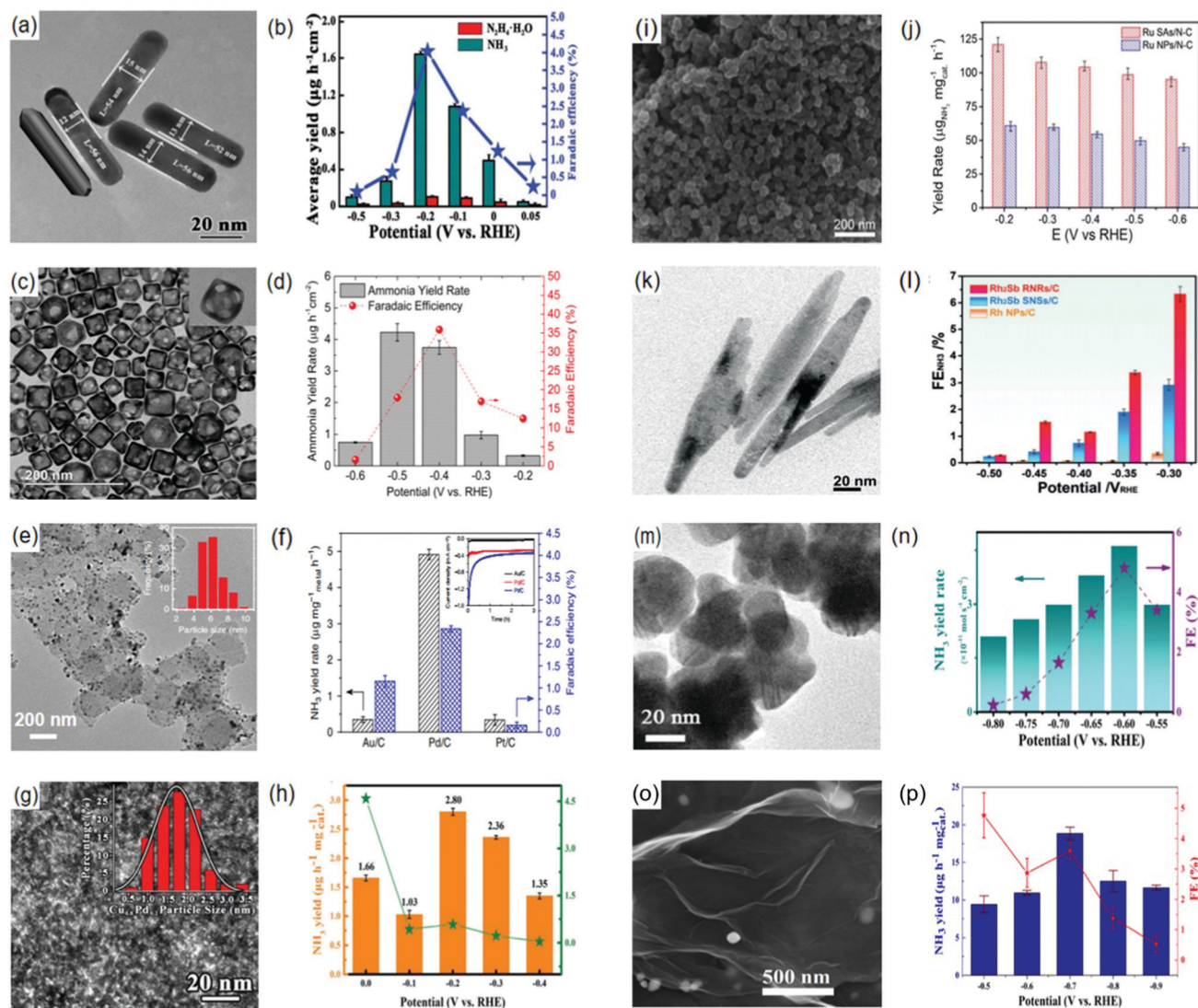
Fig. 5 (a) TEM image of Au nanorods with aspect ratio 4 ± 0.5. (b) Yield rate of ammonia (cyan), hydrazine hydrate (red) formation, and faradaic efficiency (blue) at each given potential. Panels (a) and (b) are reproduced with permission.[223] Copyright 2017, Wiley. (c) TEM image of hollow Au nanocages, and their (d) NH_3 yield rate and FE at different potentials in 0.5 M $LiClO_4$ aqueous solution. Panels (c) and (d) are reproduced with permission.[227] Copyright 2018, American Chemical Society. (e) TEM image of the Pd/C catalyst (inset: particle size distribution). (f) NH_3 yield rates and FE of the Pd/C catalyst in 0.05 M H_2SO_4, 0.1 M PBS and 0.1 M NaOH at −0.05 V (vs. RHE). Panels (e) and (f) are reproduced with permission.[228] Copyright 2018, Nature Communication. (g) STEM image of $Pd_{0.2}Cu_{0.8}$/rGO (inset: particle size distribution). (h) NH_3 yield rates and FE of the $Pd_{0.2}Cu_{0.8}$/rGO composite at different potentials in 0.1 M KOH. Panels (g) and (h) are reproduced with permission.[229] Copyright 2018, Wiley. (i) SEM image of Ru SAs/N–C. (j) yield rate of NH_3 production at different applied potentials on Ru SAs/N–C and Ru NPs/N–C. Panels (i) and (j) are reproduced with permission.[230] Copyright 2018, Wiley. (k) TEM image of Rh_2Sb SNRs. (l) FE in comparison to Rh_2Sb RNRs/C, Rh_2Sb SNRs/C, and Rh NPs/C at different potentials. Panels (k) and (l) are reproduced with permission.[231] Copyright 2020, Wiley. (m) TEM image of the Ag nanosheet, and its corresponding (n) NH_3 yield rate and FE at different potentials. Panels (m) and (n) are reproduced with permission.[232] Copyright 2018, Royal Society of Chemistry. (o) SEM image of Ag NPs–rGO, and its corresponding (p) NH_3 yield rate and FE at different potentials. Panels (o) and (p) are reproduced with permission.[233] Copyright 2020, Springer Nature Switzerland AG. Part of Springer Nature.

electrocatalysts, the HER impedes the NRR by decreasing the number of catalyst active sites due to the increased *H-coverage. This fact considerably affects the energy barrier for the first N_2 hydrogenation and desorption of *NH_2.[240] One of such modalities to promote the NRR activity of Ru-based electrocatalysts is the anchoring of Ru atoms on appropriate support structures such as N-doped carbon. For instance, Geng and co-workers demonstrated that Ru atoms anchored on

N-doped carbon (Ru SAs/N–C) attained a remarkably high NH_3 yield rate of 120.9 μg h^{-1} $mg^{-1}_{cat.}$ and 29.6% FE (Fig. 5(i) and (j)).[230] The reason behind this is that with the aid of the porous and defective N-doped carbon, the dispersion of isolated Ru atoms throughout the Ru SAs/N–C structure promoted the adequate coordination of Ru atoms by N atoms. Similarly, atomic Ru doped in Mo_2CTX MXene remarkably promoted the electrochemical N_2-to-NH_3 conversion.[241]

Rh-Based electrocatalysts. Based on several theoretical investigations, rhodium (Rh) can be considered as a promising NRR electrocatalyst as indicated by its position at the top of the volcano plot. So far, experimental studies have demonstrated various Rh nanostructures to be suitable for the electroreduction of N_2 to NH_3. This includes structures such as nanosheets,[242] nanoparticles,[231] nanowires[243] and nanorods.[231] For instance, Hou and co-workers recently reported that ultrathin Rh nanosheet nanoassemblies (Rh NNs) demonstrated an excellent NRR catalytic activity with a yield rate of 23.88 μg h^{-1} mg^{-1}_{cat} at −0.2 V (*vs.* RHE). Moreover, Rh NNs displayed good NH_3 selectivity without the formation of N_2H_4. The remarkable activity is attributed to the unique ultrathin two-dimensional nanosheet structure (*ca.* 1 nm), modified electronic construction and high SSA.[242]

To further improve the catalytic activity, schemes to modulate the surface roughness of the catalysts were considered. Adopting a facile hydrothermal approach, Zhang and co-workers synthesized a surface-rough Rh_2Sb nanorod on carbon (Rh_2Sb RNRs/C) and compared its NRR performance with that of a surface-smooth Rh_2Sb nanorod (Rh_2Sb SNRs/C) and Rh NPs/C. The NH_3 yield rates attained by these catalysts are 228.85 ± 12.96 μg h^{-1} mg^{-1}_{Rh}, 63.07 ± 4.45 μg h^{-1} mg^{-1}_{Rh} and 22.82 ± 1.49 μg h^{-1} mg^{-1}_{Rh}, respectively, at −0.45 V (*vs.* RHE), with 10 h stability witnessed by Rh_2Sb RNRs/C (Fig. 5(k) and (l)).[231] The superior catalytic activity by Rh_2Sb RNRs was attributed to the high-index facets which enhanced the adsorption and activation of N_2.

Ag-Based electrocatalysts. Among all the noble metals utilized as catalyst systems, silver (Ag) is the most promising candidate given that it is more abundant and offers the lowest cost relative to its catalytic activities. On this account, inquiry into its catalytic ability in the electrochemical synthesis of NH_3 has gained some attention. Our group conducted a pioneering study in this regard and revealed that Ag nanosheets are an efficient electrocatalyst for N_2 fixation to NH_3 with remarkable stability and selectivity under ambient conditions. When tested in 0.1 M HCl, the Ag nanosheets achieved a yield rate of 4.62 × 10^{-11} mol s^{-1} cm^{-2} and 4.8% FE at −0.60 V (*vs.* RHE) with 24 h stability (Fig. 5(m) and (n)).[232]

To further improve the NRR efficiency, measures to retard the HER are necessary. On this account, Ji and co-workers revealed that the adsorption of halide anions on the surface of porous Ag effectively assisted the suppression of HER. In this study, the authors fabricated a nanoporous bromide-derived Ag film on Ag foil (BD-Ag/AF) with adsorbed Br- anions by means of *in situ* electrochemical reduction of the AgBr film on Ag foil. When tested in 0.1 M Na_2SO_4, BD-Ag/AF attained an improved FE efficiency of 7.36% in comparison to 0.38% of the porous Ag film alone, and a yield rate of 2.07 × 10^{-11} mol s^{-1} cm^{-2} at −0.6 V (*vs.* RHE) with 20 h stability.[244]

Despite the remarkable stability, the harsh self-aggregation of small-sized Ag nanoparticles affects their activity in addition to decreasing the electronic conductivity. To this effect, employing conductive substrates such as RGO to boost the catalyst's conductive features while simultaneously enabling particle dispersion has been proven to enhance the activity of the N_2-to-NH_3 conversion. For instance, Li and co-workers fabricated a Ag nanoparticles-reduced graphene oxide hybrid (Ag NPs-rGO) as a high-efficiency electrocatalyst for the NRR. When tested in 0.1 M Na_2SO_4, Ag NPs-rGO achieved an NH_3 yield rate of 18.86 μg h^{-1} $mg^{-1}_{cat.}$ and 3.60% FE at −0.7 V (*vs.* RHE) (Fig. 5(o) and (p)), outperforming the Ag NPs under the same conditions (yield = 9.43 μg h^{-1} $mg^{-1}_{cat.}$ and FE = 2.25%).[233]

3.2.2. Non-noble metal based electrocatalysts

Metallic substance. Similar to noble metal based electrocatalysts, non-noble metals and their compounds have also shown good NRR activity and are considered as potential replacements for noble metal electrocatalysts. Molybdenum (Mo) is one of the many metallic elements with a strong affinity for N_2 adsorption, which is a preliminary characteristic for the NRR. The (110)-oriented Mo nanofilm has been proven to be an efficient catalyst under ambient conditions. Electrochemically, the (110)-oriented Mo nanofilm yielded NH_3 at a rate of 1.89 μg h^{-1} cm^{-2} and an FE of 0.72% at −0.49 V (*vs.* RHE) and 0.14 V (*vs.* RHE), respectively.[245] The low NH_3 yield was attributed to the strong Mo–N bonding making it difficult for the desorption of NH_3. To circumvent this, it is recommended to introduce higher electronegative non-metal atoms (such as N) into the Mo lattice which could potentially assist the reduction of electron charge transfer between the Mo and N-adatoms/admolecules.[205,246]

Because of the unique electronic structure and sluggish HER activity, bismuth (Bi) based materials demonstrate a high NRR performance. The ammonia yield of the fragmented Bi^0 nanoparticles was found to be 3.25 ± 0.08 μg cm^{-2} h^{-1} at −0.7 V *vs.* RHE with a faradaic efficiency of 12.11 ± 0.84% at −0.6 V *vs.* RHE.[247] Compared with Bi^0 nanoparticles, the three dimensional amorphous BiNi alloy showed an enhanced NRR activity. The NH_3 yield rate of this structure was 17.5 μg h^{-1} mg_{cat}^{-1} with a faradaic efficiency of 13.8% at −0.6 V *vs.* RHE. These two works indicate the significance of the electronic and geometric structure of the electrocatalysts in NRR.[248]

Another highly desirable metal material for the electrochemical N_2-to-NH_3 conversion is iron (Fe) given its important role as a catalyst system.[249] A typical example is its function as an earth-abundant and low-cost catalyst for NH_3 production in the industrial Haber–Bosch process.[250] In terms of biological N_2 fixation, Fe is also present in all three forms of nitrogenase enzymes (MoFe-, VFe-, and FeFe-nitrogenase).[251] Founded on this, several investigative studies have focused on developing Fe-based catalyst systems that can support the electrosynthesis of NH_3. First, theoretical evidence has revealed that Fe is one of the most promising NRR electrocatalysts among the available TMs.[201] Further studies have demonstrated the associated mechanism as the NRR pathway on Fe-based electrocatalysts such as Fe_2O_3 with the first protonation step being the rate-determining step.[252] Similar to all other metallic substances, Fe-based metal electrocatalysts display low NH_3 yield resulting from passivated electrocatalytic activity from aggregated Fe-species generated during the NRR.[202,203]

Metal hydroxides and oxides. As previously mentioned, Fe has shown a tremendous application as a catalyst system. Likewise, iron oxide based materials such as Fe_2O_3 have also presented good catalytic characteristics.[253,254] Experimental studies on Fe_2O_3 NPs over a Ni cathode have demonstrated a substantial NH_3 yield rate with a FE of nearly 35%, but at a high temperature of 200 °C.[253] Moreover, it was established that the yield rate of NH_3 is dependent on the Fe_2O_3 NPs. For instance, over a 100-fold increase in yield was witnessed within the same time frame when the Fe_2O_3 particle size was reduced from ~ 70 μm to 1–3 μm. However, for a further decrease to 10–30 nm, the NRR was too rapid and violent to be evaluated.[254]

In addition, the use of conductive supports has also demonstrated to improve the catalytic utilization of γ-Fe_2O_3 NPs. Anchoring γ-Fe_2O_3 NPs on porous CP resulted in an NH_3 yield rate of 0.9503 μg h^{-1} mg^{-1},[255] which is triple the yield from the Fe catalyst (0.3044 μg h^{-1} mg^{-1}).[188] Likewise with other TMs, the enhanced activity is related to the improved interface between the NPs and the carbon surface, which offers unique carbon sites for N_2 fixation.[256] Moreover, modulating the loading of the catalyst content on the support is suggested for optimal tuning of the NH_3 formation rate.[257]

The nature of the electrolyte is another factor of great importance for the effective performance of NRR electrocatalysts. Generally, N_2 fixation in a molten salt is associated with high temperatures requiring a high energy input. On this account, investigative studies have demonstrated the catalytic efficacy of Fe-based catalysts in different electrolytes such as N_2-saturated ionic liquids ([C4mpyr], [eFAP] and [$P_{6,6,6,14}$][eFAP]) (Fig. 6(a) and (b))[258] or N_2-saturated alkaline electrolytes (Fig. 6(c) and (d)).[255] In these studies, the high solubility of N_2 in the ionic liquids enabled the high NRR activity.

The reaction of Fe_2O_3 in an alkaline aqueous solution is represented by reaction (41).[259] In this case, the generated $Fe(OH)_2$ could lead to the passivation of Fe_2O_3, which affects the activity on the surface of Fe_2O_3.[260] However, based on reaction (42), $Fe(OH)_2$ can also be converted to FeOOH in an alkaline solution.

$$Fe_2O_3 + 3H_2O + 2e^- \rightarrow 2Fe(OH)_2 + 2OH^- \quad (41)$$

$$2Fe(OH)_2 + 2OH^- \rightarrow FeOOH + H_2O + e^- \quad (42)$$
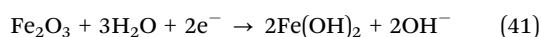
Recent findings have shown that β-FeOOH nanorods can also facilitate NRR but in 0.5 M $LiClO_4$ solution under atmospheric conditions with a high NH_3 yield rate of 23.32 μg h^{-1} mg^{-1}cat. and an FE of 6.7% at –0.75 V (*vs.* RHE) and –0.70 V (*vs.* RHE), respectively.[261] Similarly, our group demonstrated a higher NH_3 yield rate of 27.3 μg h^{-1} mg$_{cat.}^{-1}$ and 14.6% FE at –0.4 V (*vs.* RHE) while using FeOOH quantum dot decorated graphene sheets (FeOOH QDs-GSs) under ambient conditions.[262] Salazar-Villalpando and coworkers revealed that proton adsorption on this surface is suppressed by the presence of halide anions resulting in the boosting of catalytic activity.[263] On this account, Zhu and co-workers assessed the catalytic characteristic of fluorine-doped β-FeOOH nanorods (β-FeO(OH,F)/CP). Under this circumstance, the presence of the F atom enhanced

the electrocatalytic NRR performance of β-FeOOH nanorods by reducing the overpotential. Moreover, the authors concluded using DFT calculations that the lowering of the overpotential and improved activity result from the reduction in the reaction energy barrier by the F atom.[264] Hence, this approach is highly favorable to enhance Fe-based electrocatalysts for NRR processes involving neutral solutions. Xiang and coworkers established that Fe_2O_3 catalysts can activate the NRR process in a neutral medium.[265] However, it was reported that Fe_2O_3 reduced to other Fe-species such as Fe_3O_4 and Fe at large negative potentials. Remarkably, Fe_3O_4 possesses higher electronic conductivity than Fe_2O_3, demonstrating the potential to function as a superior catalyst system.[266] Recent studies have supported this claim by presenting Fe/Fe_3O_4 as a suitable NRR electrocatalyst in 0.1 M PBS under atmospheric conditions.[267] It is noteworthy that the PBS electrolyte was selected in this case due to its ability to effectively suppress the HER.[268] Due to the co-occurrence of Fe and Fe_3O_4, an actual electrochemical mechanism of these Fe_3O_4 catalysts is still unclear. Subsequent studies investigating the properties of Fe-based compounds towards N_2 fixation revealed that compound centers that possess high-spin polarization can better function effectively as active centers to promote nitrogen uptake and activation at low temperatures.[269] Besides, studies have shown that the Fe_3O_4 nanorod is also a viable electrocatalyst for NH_3 synthesis under ambient conditions.[270]

Owing to their strong affinity towards N-adatoms/admolecules than H-adatoms, Ti and its oxides are also highly considered as catalyst systems for electrochemical NH_3 synthesis. However, when acting alone, Ti-based materials have low NRR activity owing to their poor electronic conductivity.[271] To circumvent this, Ti-based catalysts are supported on conductive substrates such as RGO (TiO_2-rGO). When tested in a neutral solution (0.1 M Na_2SO_4), an ammonia yield rate of 15.13 μg h^{-1} mg^{-1}cat. and 3.3% FE at −0.90 V (*vs.* RHE) were observed over TiO_2-rGO (Fig. 6(e) and (f)).[272]

Moreover, C-doping has shown great potential for improving the electro-conducting state of TiO_2.[281] When doped with carbon, C-doped TiO_2 NPs displayed a high NH_3 yield rate of 16.22 μg h^{-1} mg^{-1}cat. and a FE of 1.84% at –0.7 V *vs.* RHE in 0.1 M Na_2SO_4 (Fig. 6(g) and (h)).[273] Compared to the effect of C-dopant, B-dopants as an electron deficient atom could enrich the positively charged centers for N_2 adsorption and activation (Fig. 6(i) and (j)). B-doped TiO_2 produced NH_3 at a rate of 14.4 μg h^{-1} mg^{-1}cat. at −0.8 V *vs.* RHE in 0.1 M Na_2SO_4,[274] which was slightly lower than that of C-doped TiO_2 NPs.[273] However, the former demonstrated a higher FE of about 3.4% when compared to the 1.84% of the latter. The variation in the activity was related to the transitioning of the semiconducting phase of TiO_2 into a semi-metal state due to the appropriate B-doping resulting in the transfer of more electrons to expedite N_2 activation. Also, the introduction of B-dopant resulted in the formation of O-vacant defects on the TiO_2 surface which enabled the trapping of electrons at the vacant active sites for severing the N≡N bond.[274]

In view of the presence of defects, it is conceived that the occurrence of O-vacancies of NRR electrocatalysts can result in
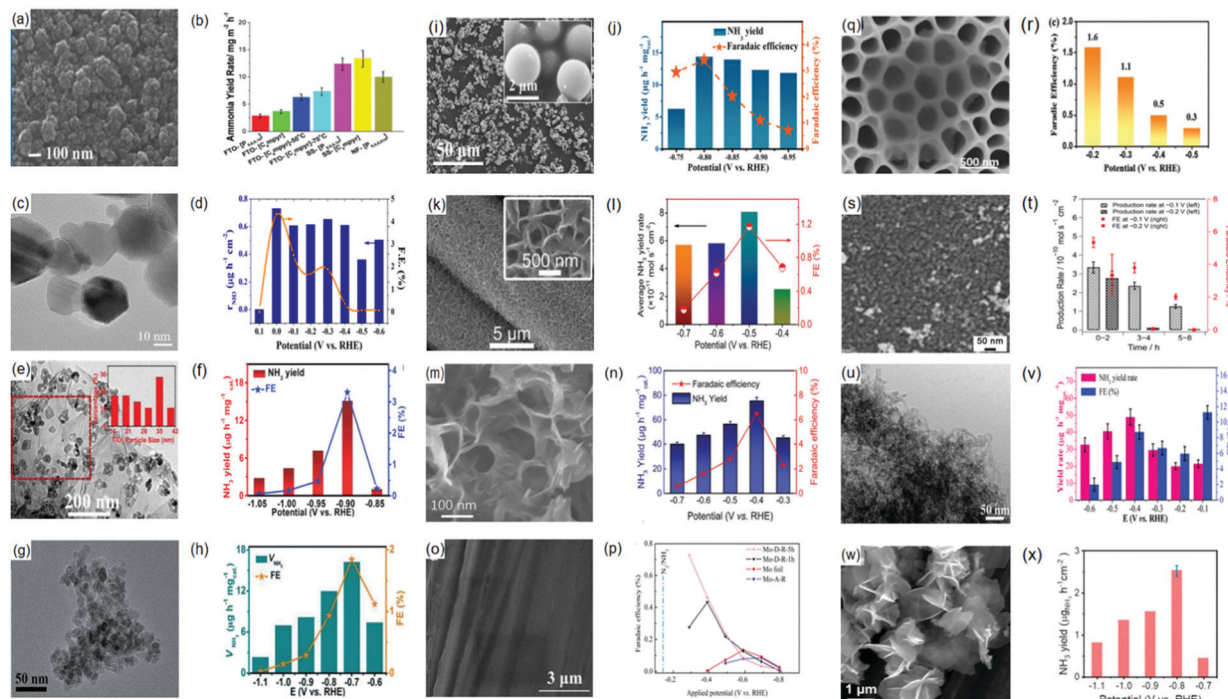
Fig. 6 (a) SEM image of the Fe-based catalyst and the corresponding (b) NH_3 yield rate on different electrodes and ionic liquids at -0.8 V (vs. NHE). Images (a) and (b) are reproduced with permission.[258] Copyright 2017, Royal Society of Chemistry. (c) TEM image of γ-Fe_2O_3 NPs, and the corresponding (d) NH_3 yield rate and FE at different potentials in N_2-saturated 0.1 M KOH. Images (c) and (d) are reproduced with permission.[255] Copyright 2017, American Chemical Society. (e) TEM image of TiO_2-rGO (inset: the particle size distribution of TiO_2) and its corresponding (f) NH_3 yield rate and FE at different potentials in 0.1 M Na_2SO_4. Images (e) and (f) are reproduced with permission.[272] Copyright 2018, Royal Society of Chemistry. (g) TEM image of C-TiO_2 NP and its corresponding (h) NH_3 yield rate and FE at different potentials in 0.1 M Na_2SO_4. Images (g) and (h) are reproduced with permission.[273] Copyright 2019, Royal Society of Chemistry. (i) SEM image of B-TiO_2 and its corresponding (j) NH_3 yield rate and FE at different potentials in 0.1 M Na_2SO_4. Images (i) and (j) are reproduced with permission.[274] Copyright 2019, American Chemical Society. (k) SEM image of MoS_2/CC and its corresponding (l) NH_3 yield rate and FEs at different potentials. Images (k) and (l) are reproduced with permission.[275] Copyright 2018, Wiley. (m) SEM image of Fe_3S_4 nanosheets and their corresponding (n) NH_3 yield rate and FEs at different potentials. Images (m) and (n) are reproduced with permission.[276] Copyright 2020, Wiley. (o) SEM image of the (110)-oriented Mo nanofilm and its corresponding (p) FE at different potentials. Images (o) and (p) are reproduced with permission.[245] Copyright 2017, Royal Society of Chemistry. (q) SEM image of Mo_2C/C nanosheets and their corresponding (r) FE at different potentials. Images (q) and (r) are reproduced with permission.[277] Copyright 2018, Wiley. (s) SEM image of VN nanoparticles. (t) Time-dependent production rate and faradaic efficiency at -0.1 V and -0.2 V for 8 h tests, respectively. Images (s) and (t) are reproduced with permission.[278] Copyright 2018, American Chemical Society. (u) TEM image of CoP/CNs and their corresponding (v) NH_3 yield rate and FE at different potentials. Images (u) and (v) are reproduced with permission.[279] Copyright 2019, Royal Society of Chemistry. (w) SEM image and (x) NH_3 formation rates at different potentials of Bi NSs. Images (w) and (x) are reproduced with permission.[280] Copyright 2020, Royal Society of Chemistry.

the generation of H^+ defects which can trap electrons for the activation of N_2.[282] For instance, Zhang and co-workers highlighted the significant role of O-vacant sites in the N_2-to-NH_3 conversion over TiO_2. Here, a yield rate of 5.62 μg h^{-1} cm^{-2} with 2.5% FE was achieved at -0.7 V vs. RHE while utilizing defective TiO_2 in 0.1 M Na_2SO_4.[283] In other studies, the presence of O-vacancies was credited for the increased activity over TiO_2 to 7.59 μg h^{-1} cm^{-2} from 1.04 μg h^{-1} cm^{-2} for the perfect TiO_2 in an acidic medium. Moreover, an increase in FE was also observed from 0.95% to 9.17% under ambient conditions.[284]

Metal chalcogenides. Following the significant role of S and Mo in nitrogenases for N_2 fixation, studies have shown that the presence of S atoms can enhance the NRR activity of Mo.[275] In addition to this, the preliminary study on the electroreduction of NH_3 by Furuya and Yoshiba in 1990 revealed that metal

chalcogenides (comprising of sulfides and selenides) displayed best NRR activity, with ZnSe being the most suitable for the reduction of N_2.[14] However, the FE was relatively low and was attributed to the relative competition of the HER. In this case again, suppressing the HER activity is a challenge to be confronted. Hence, the development of this set of electrocatalysts is crucial towards an effective NRR with high NH_3 yield.

Recently, Sun and co-workers reported the effectiveness of MoS_2 nanosheets grown on carbon cloth (Fig. 6(k)) to serve as an NRR electrocatalyst yielding NH_3 at a rate of 4.945 μg $h^{-1}cm^{-2}$ with 1.17% FE at -0.5 V (vs. RHE) in 0.1 M Na_2SO_4 solution (Fig. 6(l)).[275] Regarding the NRR performance of MoS_2, Suryanto and co-workers related the suppression of HER to the enriched N_2 binding sites partly resulting from the occurrence of isolated S-vacancy defects, which served as centers for hydrogenation.[285]

Theoretically, Abghoui and co-workers investigated the NRR potential of several TM sulphides via a DFT computational

study. After structural optimization, computational results revealed that RuS_2 is the most active among all examined model catalysts that could catalyze the N_2-to-NH_3 conversion at potentials around −0.3 V through the associative mechanism. NbS, CrS, TiS, and VS are also promising NRR catalyst systems with both associative and dissociative mechanisms at overpotentials ranging from 0.7 to 1.1 V.[286] In addition to these sulfides, metal selenides have also demonstrated good NRR activity under ambient conditions. Recent development has fabricated selenium vacancy rich $ReSe_2$@carbonized bacterial cellulose as an active electrocatalyst to attain an NH_3 formation rate of 28.3 μg h^{-1} cm^{-2} with 42.5% FE at −0.25 V (*vs.* RHE) (Fig. 6(m) and (n)).[276]

Metal carbides. Another suitable candidate as an efficient NRR electrocatalyst is metal carbides (also known as TM carbides, TMCs). Apparently, the adsorption and activation of N_2 depend on the electronic structure of the constituting elements of the electrocatalyst. Elements with unoccupied d-orbitals are more suited to interchange electrons with N-admolecules, which will enable N_2 activation. Besides the noble metals that offer these rare abilities, TMCs are predicted to display a similar concept due to the presence of unoccupied d-orbitals.[287] Coupled with this, the hybridized orbitals between the TM (sp-orbital) and the carbide (s-orbital) will facilitate more back-donation to the π orbitals of N_2, thereby enhancing N_2 fixation.

As mentioned earlier, a well-known metal carbide with high catalytic activity is molybdenum carbide (Mo_2C) which has displayed strong affinity towards electron-rich compounds and activation of the HER.[288,289] When compared to the conventional Mo electrocatalysts (Fig. 6(o) and (p)),[245] Mo_2C nanodots displayed a significant improvement in NH_3 yield and efficiency (Fig. 6(q) and (r)). In addition to the inactivation of spilled over H-adatoms by the inlaid structure, other factors that contributed to the improved ammonia yield include enhanced N_2 adsorption and activation on the enriched size-promoted active sites and the reduction of H-coverage on the catalyst surface. Despite the good NRR performance, the occurrence of a high HER activity was observed.[277] To overcome this limitation, it was suggested that inducing C-vacancy defects is likely to fortify the metal–C ratio in order to retard the accumulation of H-adatoms and thereby evolution of H_2.[290]

Recently, a new family of two-dimensional (2D) TM carbides and carbonitrides, also known as MXenes ($TM_{n+1}X_n$ (n = 1–3, and X = C and/or N)), have presented good catalytic activity towards the electrosynthesis of NH_3.[262,291] These compounds have specific structural characteristics given that their lattice TMs are exposed on both sides of the 2D layers and mostly terminated by F, O and/or OH groups with the general formula $TM_{n+1}N_mX_n$ (N = F, OH, and/or O).[292] Given their nascent discovery, thorough investigative studies on their mechanism are unknown. However, it is alleged that O- and OH-terminated MXenes are the most catalytically viable given their stability and remarkable charge distribution. In addition, theoretical evidence has revealed that the O-terminated MXenes are active

centers for HER which can be exploited to retard the HER process.[291]

Based on quantum theory, the synergistic coupling effect of TMs and the integrated C-atom resulting in the unique hybridization of their orbitals enables the TMCs to behave as catalysts with electron-enriched characteristics.[287] Specifically, there is a shift in the d-band of the TM upon the integration of the TM and C atoms, which will facilitate its hybridization with the C s-orbital resulting in electron-enriched orbitals that can offer more electrons to severe the π-orbitals of N_2.[277] Theoretical studies to this effect have revealed the resultant low activation energy (0.32 and 0.39 eV *vs.* SHE) for the N_2-to-NH_3 conversion on V_3C_2 and Nb_3C_2, respectively.[293]

To gain insights into the NRR mechanistic pathway on TMCs, Shao and co-workers investigated the N_2-fixation mechanism on MXenes. It was reported that the overall NRR energy is decided by electron transfer between the TMC and N_2. Specifically, the donation and reception of more electrons from the TMCs are likely to indicate an exothermic and endothermic reaction, respectively. Hence, for an effective N_2-to-NH_3 conversion, more exothermic reaction, an extended N–N bond and substantial charge transfer are required. Based on this, mechanism-guided prediction shows that Mo_2C and W_2C are more suitable for electrosynthesis of NH_3.[222] Subsequent experimental studies validated this claim by demonstrating that Mo_2C nanorods yielded NH_3 at a remarkable rate of 95.1 μg h^{-1} mg$^{-1}_{cat}$ and 8.13% FE at −0.3 V (*vs.* RHE) in 0.1 M HCl.[294] Another reported TMC for NH_3 synthesis is the F- and OH-terminated $Ti_3C_2N_x$ (N = F, OH) nanosheets which displayed a yield rate of 20.4 μg h^{-1} mg$^{-1}_{cat.}$ and 9.3% FE at −0.4 V (*vs.* RHE).[270]

Metal nitrides. Similar to TMCs, metal nitrides (also known as TMNs) are fabricated by integrating the N-atom into the skeletal structure of the TM resulting in the d-band contraction with an electronic structure similar to that of noble metals.[295] Owing to the large distinction in electronegativity between the N atom and the TMs, TMNs possess enriched acid–base active centers resulting from the enhanced distribution of electron charges. The availability of the distributed active centers makes TMNs suitable candidates for NH_3 electrosynthesis.

Like the TMs, TMNs can also enable the synthesis of NH_3 by the direct reduction of the incorporated N atom, thereby creating a N-vacancy on the surface of the TMN catalyst which can also be repaired *via* N_2 adsorption.[215] Nonetheless, this pathway may be hindered by the competitive adsorption of other species other than N_2 and consequently preventing the regeneration of the catalyst. On this account, two major conditions are necessary for the design of these catalysts. These conditions should include the repair and regeneration of the vacancies and a minimal overpotential.

In recent studies, theoretical evidence has presented the preferential repair of the vacant sites by N-atoms rather than H^+, O^{2-}, or OH^- species owing to the strong energetics between these sites towards N-adatoms.[296] The N-adatom adsorption energies vary with the different facets of the TMNs. Upon optimization,

calculation results revealed that the rock-salt (RS) structures with (100) facets of the nitrides of V and Zr are the most favorable catalyst systems for high yield of N_2 fixation at low overpotentials, while the nitrides of V and Cr are more suited for high efficiencies owing to low H_2 generation.[205] Besides, the (111) facet of the RS for MnN, VN and CrN also demonstrated a low overpotential towards N_2-to-NH_3 conversion. Nevertheless, MnN is preferentially attacked by other species other than N_2 and thereby its performance as a NRR electrocatalyst is hindered.[295]

Founded on these theoretical calculations, several experimental studies have been conducted on VN as a suitable NRR electrocatalyst with more active centers for a high yield and conversion efficiency of N_2-to-NH_3. These studies include the evaluation of the VN nanosheet array on Ti mesh,[297] VN NPs (Fig. 6(s) and (t))[278] and VN nanowire array (on CC).[298] Using the trackable $^{15}N_2$ species as the feed gas, it was evident that the NRR route on VN followed the Mars–van Krevelen (MvK) mechanism with the lattice N-atom partaking in the formation of $^{14}NH_3$ and $^{15}NH_3$, and subsequent healing of the vacant site thereafter created.[278]

Metal phosphides. Among the myriads of catalyst systems for N_2-fixation under ambient conditions, transition metal phosphides (TMPs) have shown good potential in this regard given their high catalytic efficacy, earth-abundance and low-cost. In addition to this, it is stipulated that the positively charged metal sites of the TMPs serve as the active centers for N_2 adsorption and activation, while the adjacent negatively charged P-motifs are sites for proton anchoring *via* H-bonding. This electronic modulating effect of phosphorus has attracted research attention towards its adoption to boost the intrinsic characteristics of NRR electrocatalysts.

Experimentally, Zhang and co-workers investigated the potential of CoP NPs synthesized *via* the pyrolysis-phosphorization method as NRR electrocatalysts under ambient conditions. Here, the authors demonstrated that the as-synthesized CoP/CNs yielded NH_3 at a rate of 48.9 µg h^{-1} mg$^{-1}_{cat}$ and 8.7% FE at -0.4 V (*vs.* RHE) in 0.1 M Na_2SO_4 with an associative distal mechanism (Fig. 6(u) and (v)).[279] Recently, Zhang and co-workers also revealed the significant role of support effects in the modulation of surficial electronic characteristics of Ni_2P NPs.[280] In this study, Ni_2P NPs supported on N,P co-doped CNs (Ni_2P/N,P-C) were tested in alkaline, acidic and neutral solutions under ambient conditions. The Ni_2P/N,P-C catalyst displayed an excellent catalytic activity in all electrolytes with the highest performance witnessed in 0.1 M KOH with a yield rate of 90.1 µg h^{-1} mg^{-1} and 19.82% FE at -0.2 V (*vs.* RHE). In 0.1 M HCl, a yield rate of 34.4 µg h^{-1} mg^{-1} and 17.21% FE were witnessed (Fig. 6(w) and (x)).[280] The high activity of Ni_2P/N,P-C was attributed to the appropriate modulating effect of the N,P-C substrate to trap and distribute electrons. Following the establishment of the unusual role of phosphorus in modulating the NRR activity of catalyst systems and the importance of support effects, we demonstrated the high NRR performance of the FeP_2 NP-RGO hybrid. When tested in 0.5 M $LiClO_4$, an NH_3 yield rate of 35.26 µg h^{-1} mg$^{-1}_{cat}$ and a high FE of 21.99% at -0.4 V

(*vs.* RHE) were witnessed.[299] Theoretical evidence shows that the FeP_2 offers enriched active sites, higher N_2 adsorption energy and a retarding effect for the HER than FeP.

3.2.3. Metal-free electrocatalysts. As mentioned earlier, TMs are suitable catalytic candidates for electrochemical NRR due to their intrinsic electronic structure with electron interchangeability between the σ and π orbitals of the N_2 molecule. Despite this, most TMs are incompetent to strongly bond with N_2, and hence cannot aid towards the desirable level of N_2 activation. Moreover, it is argued that the electrons in the d-orbital assist the interaction with H which promotes the HER. From an environmental standpoint, the probable release of TMs to the environment during the catalytic process partly dissuades the potential application of this set of catalysts. Under these circumstances, metal-free materials are highly attractive as electrochemical catalysts for N_2-to-NH_3 conversion.[300] Relative to TMs, metal-free electrocatalysts are enriched with valence electrons and show weak H_2 adsorption capacity, which render them suitable for N_2 fixation.[161]

Carbon-based electrocatalysts. Carbon-based electrocatalysts are one of the favorable alternatives for metal-based NRR electrocatalysts owing to their low HER selectivity,[301,302] unfavorable H_2 formation at the C edge site[303] and high electrical conductivity and electrochemical stability.[300] Also, these unique electrocatalysts easily offer to back-donate their copious π electrons to the π orbitals of N_2 leading to the activation of N-admolecules. Nonetheless, pristine carbon-based materials still have a low NRR catalytic activity owing to the inert nature of the π electrons. To circumvent these shortcomings, approaches to modulate the NRR activity of carbon-based electrocatalysts could include defect introduction[304] and heteroatom doping.[305,306] Numerous studies have revealed that the activation of N-admolecules on a defect-rich carbon structure is easily enabled on the defective sites. To promote these defective sites on the surface of carbon-based materials, N, B, O and S-dopants are the most commonly used dopants. However, a recent study revealed a remarkably high NRR activity (NH_3 yield rate = 32.33 µg h^{-1} mg$^{-1}_{cat}$ and FE of 20.82% at 0.65 V *vs.* RHE) on P-doped graphene in 0.5 M $LiClO_4$ under ambient conditions (Fig. 7(a) and (b)). It was revealed that the P-dopant fostered graphene re-stacking which created more defect sites in the structure.[306]

N-Dopant. To activate the π electrons of carbon-based electrocatalysts, the lone-pair electrons of the N-atom readily conjugate with π electrons, thereby making it an effective approach to enhance the NRR activity on carbon-based materials.[307] In other words, N-doped carbon materials could generate additional Lewis pairs that can readily activate N_2 and H_2 molecules.[308] Coupled with this, N-doped carbon materials are easily polarizable such that they promote adsorption of N_2 and electron/mass transfer.[186]

Recently, experimental studies have involved incorporating N-dopant into C-based structures that exhibit remarkable NRR activity. Song and co-workers demonstrated an NH_3 yield rate 97.18 ± 7.13 mg h^{-1} cm^{-2} with $11.56 \pm 0.85\%$ FE at -1.19 V
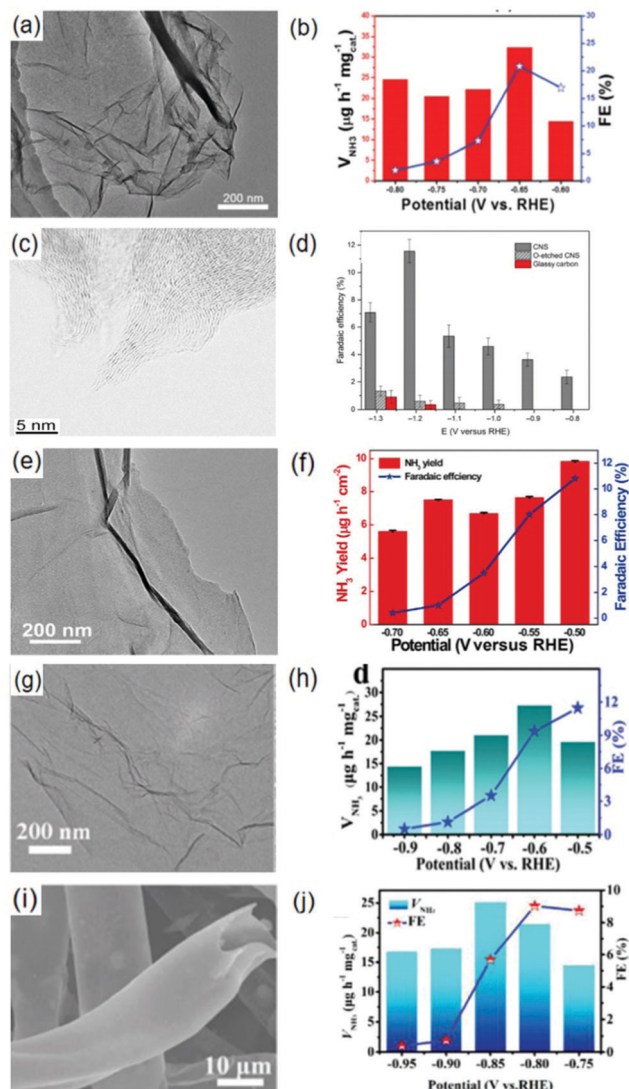
Fig. 7 (a) TEM image of P-doped graphene and its corresponding (b) NH_3 yield rate and FE at different potentials. Panels (a) and (b) are reproduced with permission.[306] Copyright 2020, Royal Society of Chemistry. (c) Aberration-corrected STEM image of N-doped carbon nanospikes and their corresponding (d) FE at different potentials. Panels (c) and (d) are reproduced with permission.[301] Copyright 2018, American Association for the Advancement of Science. (e) TEM image of B-doped graphene and its corresponding (f) NH_3 yield rate and FE at different potentials. Panels (e) and (f) are reproduced with permission.[316] Copyright 2018, Elsevier. (g) TEM image of S-doped graphene and its corresponding (h) NH_3 yield rate and FE at different potentials. Panels (g) and (h) are reproduced with permission.[323] Copyright 2019, Royal Society of Chemistry. (i) TEM image of O-doped hollow carbon microtubes and their corresponding (j) NH_3 yield rate and FE at different potentials. Panels (i) and (j) are reproduced with permission.[324] Copyright 2019, Royal Society of Chemistry.

(vs. RHE) over N-doped carbon nanospikes in 0.25 M $LiClO_4$ (Fig. 7(c) and (d)).[301] The sharp spike structure of the electrocatalyst provided a dense distribution of electrons at its tips, which promoted the dissolution of N_2.

Liu and co-workers further revealed that the NRR performance of the N-doped carbon material can be regulated by adjusting the pyridinic and pyrrolic N content in N-doped porous carbon (NPC).[186] Most importantly, the pyridinic N atom in NPC partakes in the formation of NH_3 resulting in the generation of N-vacancies that can serve as active centers for further activation of N-admolecules.[309]

However, this is most effective in alkaline solutions as NPC undergoes severe HER in acidic electrolytes.[310] Other reported N-doped carbon-based NRR catalysts include polymeric carbon nitride (PCN) with an enhanced spatial electron transfer due to the induced N-vacancies.[311,312]

B-Dopant. Similar to N-dopants, B-dopants have also shown great capacity to activate the π electrons of carbon-based electrocatalysts. Moreover, boron is a notable single atom catalyst for the electrochemical N_2-to-NH_3 transformation. In addition to their successful NRR performance,[313,314] B-dopants like N-dopants have equally attracted great attention as a means to modulate the NRR activity of carbon-based electrocatalysts.[315,316]

Boron is an electron deficient atom with four valence electrons in the sp-orbitals, which bonds uniquely with the electronic structure of C.[317] The hybridized electronic structure between these two atoms results in the generation of unoccupied orbitals that can accept lone-pair electrons from N_2. Simultaneously, the occupied 2p-orbitals can back donate electrons to the π orbitals of N-admolecules. Above all, B-atoms can retard the HER by prohibiting the binding of Lewis acids in an acidic medium.[316,318,319]

Despite the good electronic structure, this set of electrocatalysts still suffer from high HER activity and instability of adsorbed N_2, therefore requiring appropriate schemes to strengthen it.[315] In this regard, optimizing the content of B-dopant has been shown to mitigate this shortcoming. For example, B-doped graphene exhibited an optimum NRR activity at a B-dopant content of 6.2% with a yield rate of 9.8 μg h^{-1} cm^{-2} and a high FE of 10.8% at −0.5 V (vs. RHE) in 0.05 M H_2SO_4 solution (Fig. 7(e) and (f)).[316] As mentioned earlier, S plays a significant role in the biological synthesis of NH_3 by means of nitrogenase enzymes.[320] Nonetheless, the low electrical conductivity of S[321] impedes its application in the electrocatalytic NRR. To circumvent this, the adoption of conductive supports such as RGO has been proposed as a suitable mechanism for boosting the electrical conductivity of S. For example, the S-doped dots-graphene nanohybrid demonstrated a good NH_3 synthesis rate of 28.56 μg h^{-1} $mg^{-1}_{cat.}$ and 7.07% FE at −0.85 V (vs. RHE) in 0.5 M $LiClO_4$.[322] Similar to other dopants, the S atom also possesses a modulating effect to tune the NRR activity for carbon-based materials. A typical example of this effect is portrayed in the NRR performance of graphene in 0.1 M HCl under ambient conditions. Prior to S-doping, the NRR activity on graphene resulted in an NH_3 yield rate of 6.25 μg h^{-1} $mg^{-1}_{cat.}$ and a low FE of 0.52%. However, after S-doping, a significant boost in the activity was observed with an NH_3 yield rate of 27.3 μg h^{-1} $mg^{-1}_{cat.}$ and a high FE of 11.5% under similar conditions (Fig. 7(g) and (h)).[323]

O-Dopant. Similar to S atoms, O atoms possess the same electronic structure and have displayed good potential to

improve the electrocatalytic activity of carbon-based materials. In the same manner as S atoms, O-doping can trigger the activity of the inert π electrons of the carbon-based materials via O–C interactions. An example of this is demonstrated over an amorphous O-doped carbon nanosheet (CN) with a high NH_3 yield rate of 20.15 µg h^{-1} mg$^{-1}_{cat.}$ and a FE of 4.97% at −0.6 V (vs. RHE) in 0.1 M HCl.[300] Likewise, O-doped hollow carbon microtubes revealed a superior NRR performance with a yield of 25.12 µg h^{-1} mg$^{-1}_{cat.}$ and 9.1% FE at −0.85 V (vs. RHE) and −0.80 V (vs. RHE) in 0.1 M HCl, respectively (Fig. 7(i) and (j)).[324]

Elementals and their derivatives. TMs are highly recommended for NRR electrocatalysis but their selectivity towards ammonia synthesis is low. Other alternatives to replace this set of catalyst systems are the elementals and their compounds owing to their low-coordinated atoms.[277] Moreover, elemental catalysts are reported to significantly retard the HER based on the structural effect as the H-motifs are preferentially adsorbed on specific sites on the catalyst.[325] Supported by this ensemble effect, the suppression of the HER can be controlled.

A notable elemental catalyst for electrochemical reduction of N_2 is boron (B) and its compounds particularly boron nitride (BN), which have been proven to offer good NRR activity as electrocatalysts,[313,314] despite theoretical studies suggesting that B–N pairs in h-BN are inactive towards N_2-to-NH_3 conversion.[326] For instance, Zhang and co-workers experimentally demonstrated the electrocatalytic efficacy of the B nanosheet to attain an NH_3 yield rate of 13.22 µg h^{-1} mg$_{cat}^{-1}$ and 4.04% FE in 0.1 M Na_2SO_4.[327] Also, at high B concentration, the boron carbide (B_4C) nanosheet attained a high NH_3 yield rate of 26.57 µg h^{-1} cm^{-2} and a high FE of 15.95% at −0.75 V (vs. RHE). Fortunately, the catalyst displayed remarkable stability and selectivity towards NH_3 formation.[328]

Similarly, theoretical evidence has demonstrated the possibility of a monolayer phosphorus (P) catalyst system to catalyze N_2-to-NH_3 conversion.[329] From an experimental perspective, few-layered black P (BP) nanosheets were used to produce NH_3 with a high yield rate of 31.37 µg h^{-1} mg$^{-1}_{cat.}$ and 5.07% FE at −0.7 V (vs. RHE) and −0.6 V (vs. RHE), respectively. In addition, the authors also revealed that the active sites for the adsorption and activation of N_2 were more favorable on the zigzag and diff-zigzag edges of the BP nanosheets. On these nanosheets, computational analysis indicated that only the edges of the catalyst structure could facilitate electron donation during the NRR, which limited the performance of the catalyst.[330] To circumvent this, anchoring a single-atom Fe on the monolayer P was shown to vary the charge distribution and promote electron interchangeability at the edge of the catalyst system.[329]

In summary, advancements in the catalyst systems to enable efficient electrochemical N_2-to-NH_3 conversion under ambient conditions have been substantial. An ideal catalyst system should facilitate the adsorption and activation of N_2 in order to promote the NRR kinetics. Where necessary, tailoring the catalysts' electronic structure (by defect engineering, heteroatom doping, surface functionalization and interface engineering) can

enhance their intrinsic NRR characteristics. More specifically, enriching the NRR active sites/centers (size and shape modification, utilizing supports with high surface area and conductivity, and anchoring single-atoms on the catalyst system) while suppressing that of the HER is the most direct means of enhancing the N_2 reduction activity.[331] Generally, the HER has a lower overpotential enabling it to be preferentially selected over NH_3 formation; hence, the need for HER-retarding strategies such as the use of functional composite catalysts is recommended.[332,333] In addition, the electrolyte selection, stability improvement and cost-competitiveness are still the important research aspects deserving attention in order to develop competitive NRR technologies towards practicality. For a brief overview, Table 2 summarizes the recent NRR electrocatalysts and their catalytic activity, providing insights into the chemical understanding of efficient electrocatalysts for NRR.

4. Valuable fuels and chemicals via CO_2 reduction reaction

Conversion of CO_2 as part of carbon capture and utilization (CCU) technologies has received increased interest in the past couple of decades, especially in view of favourable prospects related to positive impact on the global climate change and renewable electricity production.[334,335] Research in this field has mainly focused on fundamental and mechanistic conversion of CO_2 to valuable fuels and chemicals through a variety of technologies including biochemical,[336] thermochemical,[337] photochemical[338] and electrochemical[339] reduction of CO_2. Among these technologies, electrocatalytic CO_2 reduction reaction (CRR) has attracted greater attention by virtue of its mild operating conditions and great potential to scale up.[340–343] Although significant progress is experienced in this field, there are still major challenges, which hinder the understanding of CRR.[344]

Pioneering studies on CRR involving different metals was initiated by Hori and co-workers more than thirty years ago.[11,345] However, large-scale implementation of CRR technology is still at its infant stage because, in contrast to fundamental CRR studies, the research to understand CRR from an industrial perspective and efforts to develop an industrial/commercial CO_2 electrolyzer are scarce. Due to the commercial limitations, CRR still suffers from lack of mechanistic understanding of the kinetics and thermodynamic challenges. Specifically, the C=O double bond of the CO_2 molecule possesses a high bonding energy (750 kJ mol^{-1}) when compared to the binding energies of the C–C bond (336 kJ mol^{-1}), C–H bond (411 kJ mol^{-1}) and C–O bond (327 kJ mol^{-1}) of conventional hydrocarbons. Hence, in the absence of an external support, it is energetically unfavourable to dissociate CO_2 to generate organic compounds.[346] It is therefore necessary to utilize catalyst systems to lower the energy barrier, stabilize major intermediates and facilitate reaction kinetics.

Moreover, based on the utilized catalyst system and operating condition, a wide range of reduced products can be generated
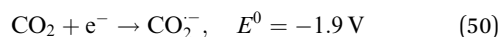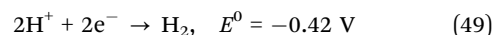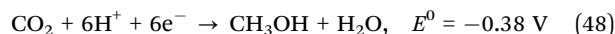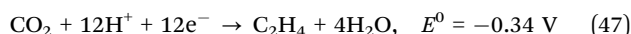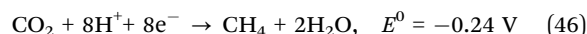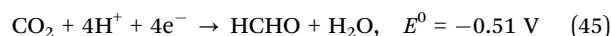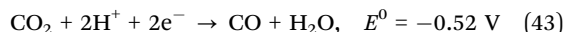
from the CRR including carbon monoxide (CO), formate/formic acids ($HCOO^-$/$HCOOH$), methane (CH_4), methanol (CH_3OH), ethane (C_2H_4), ethanol (C_2H_5OH) and so on. Principally, this is established by the reaction mechanism at a given condition and most importantly, the working electrocatalyst.[347,348] In essence, it is a considerable challenge to mechanistically tune the reaction to enhance a particular product selectivity.[349] Furthermore, this shortcoming is compounded by the kinetically competitive HER, as was also notable in the NRR and water splitting process. As an outcome, the rational design and development of catalyst systems for the electroreduction of CO_2 are highly necessary.

4.1. Electrochemistry of CO_2 reduction reaction (CRR)

4.1.1. Fundamentals of CRR. CRR is a multi-step transformation process consisting of two-, four-, six-, or eight-electron reaction pathways (Fig. 8(a))[350] to primarily synthesize formate ($HCOO^-$) or formic acid ($HCOOH$) (Fig. 8(b)), carbon monoxide (CO) (Fig. 8(c)), methane (CH_4), ethylene (C_2H_4), ethanol (C_2H_5OH) (Fig. 8(d)), etc.[341] The reaction kinetics is governed by the electrocatalyst, operating condition (pressure, temperature and pH) and electrolytic solution, irrespective of the thermodynamics involved. Primarily, the operating conditions influence the kinetics by altering the CO_2 solubility in the electrolytic solution, which is mainly favoured at high CO_2 partial pressure and low temperatures. In view of all these, the CRR occurs at the interface of the electrocatalyst-containing electrode and the CO_2-saturated aqueous solution. The electrocatalyst, preferably constituted of earth-abundant materials, and the electrolytic solution play an essential role in establishing the CRR mechanism and kinetics. Thus far, several research studies are focused on developing high-performance and less expensive electrocatalysts, particularly heterogeneous electrocatalysts, to optimize the CRR efficiency based on the reaction mechanism and kinetics.[361,362]

Conventionally, the process of heterogeneous electrocatalysis entails CO_2 adsorption on the electrocatalyst surface, electron/mass transport to severe the C–O bond with the generation of C–H bonds, structural transformation and desorption of the reduced products from the electrocatalyst surface and subsequent diffusion into the electrolytic solution.[363] The employed electrocatalyst and the applied electrode potential bias are one of the major factors that influence these processes and promote product selectivity.

From a thermodynamic point of view, a generally accepted CRR mechanism (pH 7 in aqueous solution (vs. SHE), 25 °C, 1 atm, and 1 M concentration of other solutes) for the primary products is illustrated below:

$$CO_2 + 2H^+ + 2e^- \rightarrow CO + H_2O, \quad E^0 = -0.52 \text{ V} \quad (43)$$

$$CO_2 + 2H^+ + 2e^- \rightarrow HCOOH, \quad E^0 = -0.61 \text{ V} \quad (44)$$

$$CO_2 + 4H^+ + 4e^- \rightarrow HCHO + H_2O, \quad E^0 = -0.51 \text{ V} \quad (45)$$

$$CO_2 + 8H^+ + 8e^- \rightarrow CH_4 + 2H_2O, \quad E^0 = -0.24 \text{ V} \quad (46)$$

$$CO_2 + 12H^+ + 12e^- \rightarrow C_2H_4 + 4H_2O, \quad E^0 = -0.34 \text{ V} \quad (47)$$

$$CO_2 + 6H^+ + 6e^- \rightarrow CH_3OH + H_2O, \quad E^0 = -0.38 \text{ V} \quad (48)$$

$$2H^+ + 2e^- \rightarrow H_2, \quad E^0 = -0.42 \text{ V} \quad (49)$$

$$CO_2 + e^- \rightarrow CO_2^{\bullet-}, \quad E^0 = -1.9 \text{ V} \quad (50)$$

It is evident from reactions (43)–(48) that the CRR equilibrium potentials are analogous to that for the HER (reaction (49)). Realistically, this also corresponds with the formation of H_2 as the principal by-product for the CRR process in aqueous solutions. Moreover, owing to the diminutive distinction between the thermodynamic potentials of each product (reaction (43)–(48)), it is apparent that the selectivity of desired products is challenging. This is further compounded by the enormous energy (electrode potential) requirement to drive the CRR process, as indicated in reaction (50).[364]

This reaction (reaction (50)) is the first CRR step and incites the large overpotential required to activate the reaction processes. In this step, a key intermediate $CO_2^{\bullet-}$ is formed by the first electron transfer to a CO_2 molecule with a large overpotential of -1.90 V (vs. SHE) due to the energy required to bend the linear CO_2 molecule to a radical anion.[346] Subsequently, the formed $CO_2^{\bullet-}$ radical instantaneously reacts with several H^+-coupled multiple-electron-transfer reactions to yield the reduced products. However, in practice, these intermediate reactions can be hindered as the OER occurs simultaneously with the CRR at the anode. To circumvent this, the cathode and anode compartments in the CO_2 electrolytic cell are separated by means of an ion exchange membrane to avoid the oxidation of CRR products but promote the corresponding ion transfer.[365]

4.1.2. Recent theoretical insight into CRR. The electroreduction of CO_2 generally results in the synthesis of three basic products: $HCOOH$/$HCOO^-$, CO and other higher hydrocarbons such as CH_4, C_2H_4, and C_2H_5OH.[347,366] Based on this
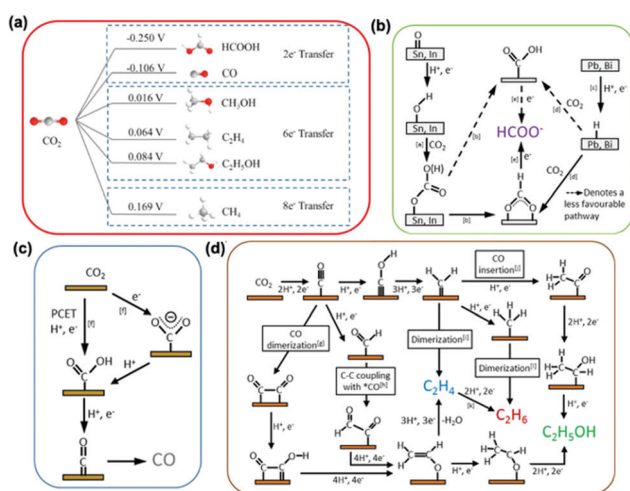

Fig. 8 (a) CO_2 reduction processes and the corresponding standard redox potentials, E^0 (vs. SHE, V) for aqueous solutions. Reproduced with permission.[350] Copyright 2014, Elsevier. CRR mechanisms to generate (b) formate, (c) CO, and (d) C_2H_4, C_2H_6 and C_2H_5OH, initiated from CO adsorption. Reproduced with permission.[341] Copyright 2018, Elsevier.

classification, theoretical insights into understanding the CRR mechanism are dependent on the specific reduced products.

Pertaining to the formation of formates or formic acids, theoretical investigations into the CRR over post-transition metals have been widely conducted.[367,368] With regard to formate formation, studies have revealed that the oxide layer of metal oxides plays a significant role in the formate production, as illustrated in Fig. 8(b).[369] Spectroscopic analysis supported by DFT calculations suggests that the initial steps of formate production arise from the formation of surface-bound carbonate or bicarbonate intermediates from the adsorption of CO_2 on the surficial O-motifs or OH-motifs, respectively.[367,370] Sequentially, the formed bicarbonate species is reduced to either *COOH or *OCHO, with the latter being more thermodynamically favourable.[371,372]

Unlike some metals, the generation of formates does not occur *via* surface-bound carbonates/bicarbonates. A notable example is Pb electrodes where DFT calculations have suggested that formate formation proceeds by means of direct hydrogenation of CO_2 by H-adatoms.[368,373] Likewise, theoretical and experimental investigation on Bi-based electrocatalysts confirms the absence of surface-bound carbonates toward the formation of formates over Bi dendrites.[374] However, both studies agree that the *OCHO intermediate is more thermodynamically viable for formate generation. Moreover, Yoo and co-workers demonstrated using DFT calculations on several modelled metal surfaces that *COOH and *H are highly correlated in their free energies. Unlike the correlation between *OCHO and *H, it is unlikely that the formation of formic acid will occur without the HER occurring along with. Based on the findings, the authors predicted that Ag and Pb are the most promising monometallic electrocatalysts with high FE for the production of HCOOH *via* CRR.[375]

Regarding the electrosynthesis of CO using CRR, several studies depict this reaction to proceed *via* the *COOH intermediate.[340] In this case, two possible pathways are proposed. The first involves the single step proton-coupled electron transfer (PCET), while the second route is the formation of the $CO_2^{\bullet-}$ radical *via* single electron transfer and subsequent protonation to *COOH.[376] Fig. 8(c) illustrates the two mechanistic routes. Irrespective of the mechanistic route, theoretical studies have shown a good correlation in the binding energies between *COOH and *CO, and *H and *CO on some metals,[377] and between *COOH and *CO, and *COOH and *H over a variety of other metals.[375] On this account, it is necessary that the development of electrocatalysts should consider schemes to optimize the surficial stabilization of *COOH without promoting the HER and influencing CO desorption. In this regard, further studies have revealed that the unsaturated coordinative sites such as the edges and corners are more promising sites for CO generation *via* CRR.[377,378] Experimental validation of this concept is demonstrated in the mechanistic studies on Ag[379] and Au.[380] Here, the nanostructured catalyst systems possessed more active sites with unsaturated coordination than their metal foil analogues.

About the electrosynthesis of C_2 products and other hydrocarbons *via* CRR (Fig. 8(d)), investigative studies on Cu and its compounds have been widely conducted. This has resulted in numerous proposed mechanisms, particularly for the different reduced products.[381–388] Owing to this, it is unlikely to completely discuss each mechanistic insight without derailing from the scope of this study. Hence, this study will only review the theoretical insight for the electrosynthesis of C_2H_4. Kindly refer to the relevant literature above for further insights into other reduced products.

One of such mechanistic routes is the dimerization of *CO, which was suggested to occur over the Cu(100) electrode. In this respect, studies have demonstrated both experimentally and computationally that the formation of C_2H_4 occurs shortly after the rate of CO generation has peaked. In addition, it was revealed that the onset potential for the generation of C_2H_4 is more negative when compared to that for CO. These findings were common on three different Cu(100, 111 and 110) surfaces.[389] Subsequently, computational studies have revealed that *CO dimerisation is more favourable on the Cu(100) facets despite the commonality in the reaction dynamics.[390] Moreover, C_2H_4 formation is hindered with an increase in CO coverage, which lowers the energy barrier. Compared to the Cu(111) facet, Cu(100) exhibited a favourable potential to synthesize C_2 products from CRR due to the presence of under-coordinated Cu sites, which is likely to enable the C–C coupling effect.

4.2. Electrocatalysts of CRR

It is established that the major parameters that hinder the industrial implementation of CRR are the selectivity, activity and stability,[391] and each of these factors can be improved by focusing on the nature of the electrocatalyst, electrolytic solution and operating conditions.[344] So far, the adopted CRR electrocatalysts include both heterogeneous and homogeneous metal based electrocatalysts consisting of earth-abundant TMs.[361,362] Moreover, carbon-based electrocatalysts have also shown great potential as an efficient catalyst system for the electroreduction of CO_2 to different reduced products.[392]

4.2.1 Metal electrocatalysts. Over time, heterogeneous metal electrocatalysts have been widely employed for the electrochemical reduction of CO_2. The nature of these electrocatalysts has varied from their bulk form to nanostructures and from single atoms to 2D- and 3D-electrocatalysts. In most cases, the formation of the key intermediate $CO_2^{\bullet-}$ is considered as the rate-determining step for electrochemical reduction of CO_2. Hence, the employed electrocatalyst should enable the stabilization of this intermediate to attain high CRR performance.

Previously, research studies have demonstrated that depending on the reaction intermediates being formed and the final reduced products, crystalline bulk metals are classified into three: (i) earth-abundant TMs (such as Zn, Sn, Pb and Bi) that can generate HCOOH/HCOO⁻ *via* the outer-sphere mechanism as a result of the weak binding with the $CO_2^{\bullet-}$ intermediate (Fig. 8(b)); (ii) noble-metal based catalyst systems such as Au, Ag and Pd that have a strong affinity towards the *COOH intermediate resulting in its further reduction to generate the weakly bound *CO intermediate. Subsequently, CO is

desorbed from the surface emerging as the main product (Fig. 8(c));[361] (iii) Cu-based electrocatalysts which have demonstrated to be the only catalyst system to bind and transform the *CO intermediate into other products.[393–395] In order words, Cu is the only catalyst system with the potential to facilitate CRR involving more than two electrons ($2e^-$) transfer with significant FE.[396] Specifically, at low and high overpotentials, $2e^-$-transfer products (such as H_2, CO, HCOOH) and multi e^--transfer products (such as CH_4, C_2H_4) are generated, respectively.

As witnessed in previous sections, suppressing the HER has been one of the focal points of most electrochemical reduction of small molecules. Similarly, attention towards retarding this reaction process is also necessary to achieve high selectivity of CRR products. On this account, schemes are employed to enhance the catalytic activity of catalyst systems, which can be reached by utilizing metal alloys, metal oxides, nanostructured metals and chalcogenides that offer enriched active centers for CO_2 adsorption and activation.[397–399] For instance, utilizing nanostructured Ag oxide as a CRR electrocatalyst has demonstrated a high CO selectivity of about 80% (0.49 V overpotential), which is considerably higher than the 4% selectivity of the Ag alone catalyst under similar conditions. The improved activity and selectivity were attributed to the strong *COOH stability on the active sites of the metal oxide.[400]

Most importantly, experimental evidence has shown that the surface nature, morphology and size of the catalyst system are influential towards the product distribution over the electrocatalysts. For instance, amorphous Cu NPs have been proven to have superior CRR activity and selectivity towards HCOOH and C_2H_5OH over the crystalline counterpart with 37% and 22% FE, respectively, at -1.4 V (vs. Ag/AgCl). The improved performance was ascribed to the enriched defective sites as a result of irregularity in the surface structure in the amorphous form (Fig. 9(a) and (b)).[401] Sequel to this, Hwang and co-workers adopted a mix of Cu states in anodized Cu(AN-Cu) as a more stable and highly selective CRR electrocatalyst for the generation of C_2H_4. The improved selectivity of C_2H_4 over CH_4 was attributed to the electrochemical reduction environment enabled by the mixed valence of the O–Cu combination catalysts (Fig. 9(c) and (d)).[399] Likewise, Rosa M. et al. tuned copper's morphology and oxidation state by pulsed CO_2 electrolysis and the production of C_{2+} products was enhanced with 76% FE at -1.0 V (vs. RHE). According to quasi in situ XPS results, they found that the improved efficiency of the Cu catalyst was due to the cooperation of Cu(I) species and continuous regeneration of defects which would promote C–C coupling pathways.[402]

Relative to single metals, hybrid or alloy metals have shown to offer improved CRR performance due to the potential to modulate the binding energy of specific intermediates on the catalyst surface.[403,404] For instance, Hoang and co-workers demonstrated the synthesized CuAg alloy film to be a more stable and efficient CRR electrocatalyst for C_2H_4 and C_2H_5OH production with a FE reaching nearly 60% and 25%, respectively, at -0.7 V (vs. RHE).[404] Elsewhere, it was elucidated that the integrating Ag and Cu atoms resulted in the occurrence of compressive strain around Cu atoms that promoted the product selectivity.[405] Given the tunable effect of Cu towards the bonding of CO-motifs and selective reduction of other intermediates, several Cu-based hybrids or alloys are developed for efficient CRR electrocatalysts.[405–407]

Most importantly, it is worth mentioning that despite the beneficial effects of these metals on the CRR performance, the activity and selectivity can be significantly influenced by the metal content. For instance, Ma and co-workers revealed that the product selectivity during the electroreduction of CO_2 using Cu-based alloys is highly affected by the Cu content.[408] Therefore, an optimization of the metal content is required for an optimal performance of CO_2 conversion. In addition, investigative studies towards the discovery of alloys with a suitable coupling effect in order to promote efficient and highly selective CRR performance are encouraged. To this effect, Zhang and co-workers examined the CRR activity of several Sn-based bimetallic catalysts towards the formation of HCOOH. The experimental results demonstrated that Ag–Sn and Cu–Sn are the most favourable for HCOOH production with a FE of 88.3% and 87.4%, respectively, when tested in 0.5 M NaHCO₃.[409]

In addition to Cu, other earth-abundant TMs (such as Ni, Co, Zn, Bi and In) and their compounds have demonstrated remarkable potential as CRR electrocatalysts.[71,339,410,411] For instance, Pan and co-workers demonstrated that an engineered Co-N₅ catalytic site using a modified Stöber method is a highly efficient CRR electrocatalyst for CO production with FE > 99% at -0.73 and -0.79 V vs. RHE (Fig. 9(h)).[412] Similarly, a carbon-anchored N-derived Zn catalyst (ZnN₄/C) demonstrated high CRR selectivity and stability towards CO production with a FE of $\sim$95% and >75 h stability at an onset overpotential of 24 mV.[413] And FeN₄ sites in Fe–N–C catalysts were also obtained from the ZIF-8 which achieved 25 mA cm^{-2} at 0.8 V (vs. RHE) and FE was above 90% for CO in a wide potential.[414] For these electrocatalysts, experimental and theoretical results reveal that the Zn–N₄, Co–N₅ and Fe–N₄ catalytic sites facilitated the activation of CO_2 and direct COOH* formation. However, the product formed via In-based catalysts is different from those of Fe, Co, and Zn based electrocatalysts which would convert CO_2 to formate. Recently, Yin's group synthesized In–N–C via In-doped ZIF-8 and the atomically dispersed structure demonstrated a high CRR performance with a turnover frequency of 26 771 h^{-1} at -0.99 V (vs. RHE) and the maximum FE for formate was around 80%. Since In was atomically dispersed in the structure, the intermediate *OCHO was formed on isolated In sites which affected the formate formation.[339]

Furthermore, to enrich the distribution of active sites, enabling a large catalyst surface area can feature catalytic active centers to improve the CRR performance. On this account, a myriad of 2D materials including nanosheets and nanofilms of metals, metal oxides and chalcogenides have portrayed good CRR activity and selectivity.[415–417] The versatility of 2D electrocatalysts originates from their unique electronic structure and stability. In addition, they offer the beneficial features of both
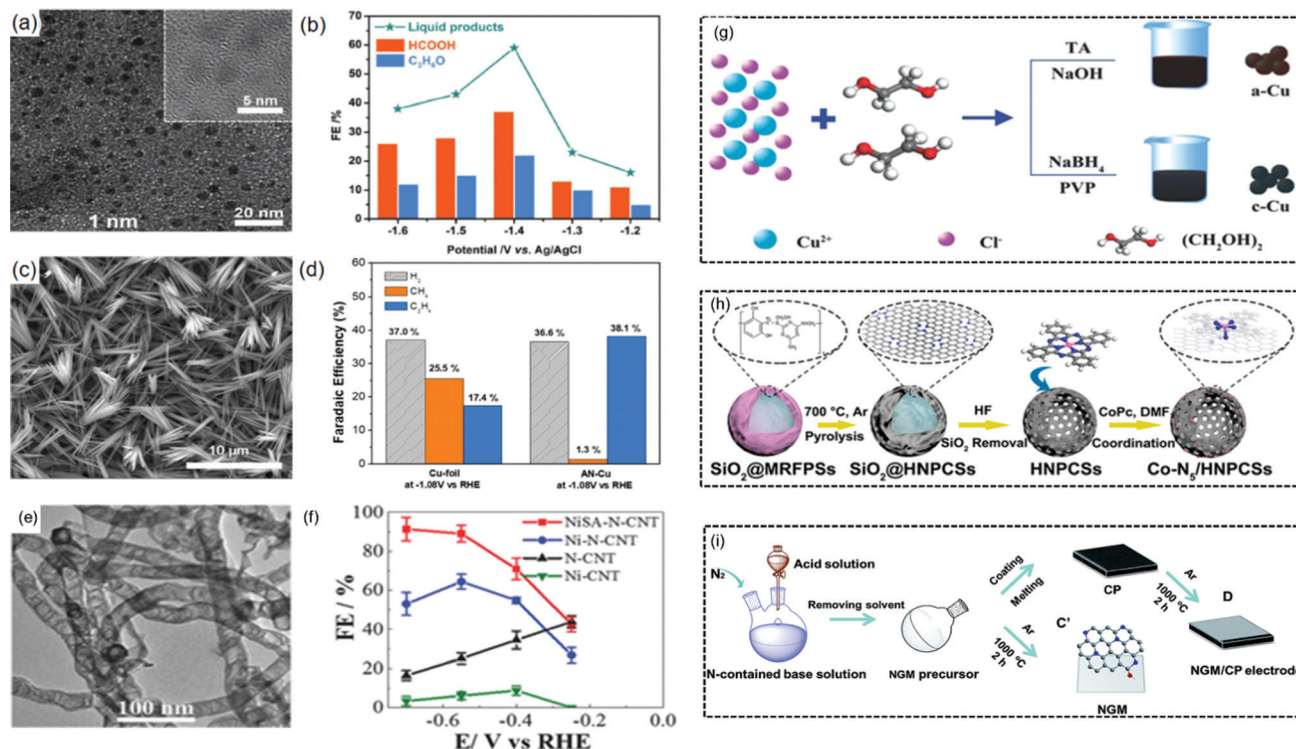
Fig. 9 (a) TEM image of amorphous Cu NPs and their (b) FE for liquid products at each given potential for 2 h. Panels (a) and (b) are reproduced with permission.[401] Copyright 2018, Wiley. (c) HRTEM image of Cu(AN-Cu) and its (d) FE for HER and hydrocarbon selectivity in comparison to Cu-foil. Panels (c) and (d) are reproduced with permission.[399] Copyright 2018, American Chemical Society. (e) TEM image of NiSA-N-CNTs. (f) Faradaic efficiency of CO for NiSA-N-CNTs, Ni-N-CNTs, N-CNTs, and Ni-CNTs at −0.28, −0.40, −0.55, and −0.70 V. Panels (e) and (f) are reproduced with permission.[413] Copyright 2018, Wiley. (g) Schematic illustration of the formation process of a-Cu and c-Cu.[401] Copyright 2018, Wiley. (h) Schematic illustration of the formation of Co-N$_5$/HNPCSs.[412] Copyright 2018, American Chemical Society. (i) Schematic illustration of the procedures to prepare NGM and NGM/CP electrodes.[348] Copyright 2016, Royal Society of Chemistry.

heterogeneous and molecular electrocatalysts.[418,419] For instance, Gao and co-workers evaluated the HCOO formation potential during CRR on two different Co-based catalytic sites. The authors revealed that surface Co atoms on the atomically thin layers displayed a higher activity and selectivity at lower overpotentials than surface Co atoms on the bulk samples. The improved activity was due to the partial oxidation of the atomic layers leading to a stable current density of 10 mA cm^{-2} and a FE of 90% at 0.24 V (vs. RHE) with 40 h stability.[386] And very recently, Cao et al. fabricated thin bismuthene (Bi-ene) with a few layers which displayed a high selectivity with FE of nearly 100% from −0.83 V to −1.18 V (vs. RHE). Based on DFT analysis and the result of in situ ATR-IR spectra, the product formate was finally obtained from the OCHO* intermediate.[417]

Moreover, tailoring the intrinsic electronic structure of the electrocatalyst can benefit the CRR selectivity. Here, Xu and co-workers revealed that the partial charge delocalization in the MoSeS monolayer resulted in the tuning of the d-band electronic structure by the lengthened Mo-Se and shortened Mo-S bonds. This alteration in the electronic structure favoured the stabilization of the COOH* intermediate and facilitated the CO desorption step, which was considered as the rate-determining step. Based on this finding, the MoSeS monolayer achieved a remarkably high FE of 45.2% for the CRR towards CO

formation, when compared to independent chalcogenides, MoSe$_2$ and MoS$_2$ monolayers, with 30.5% and 16.6%, respectively at −1.15 V vs. RHE.[420]

4.2.2. Molecular electrocatalysts. The application of molecular electrocatalysts for CRR has been recently investigated with emphasis on noble metals (such as Pd, Re and Ru) and earth-abundant TMs (such as Co, Fe, Mn and Ni).[339,362,421,422] Here, the CRR process is triggered by the potential-induced change in the oxidation state of the metals or the incorporated ligands.[344] However, this depends on the metal–ligand cooperativity, which has been interestingly favoured by the metals mentioned above. Hence, the metal–ligand interaction has become a fundamental factor for regulating the catalytic behavior of molecular electrocatalysts. Several molecular electrocatalysts have been developed for the CRR process. Recent developments on this, their applications and mechanistic investigations are reviewed in the literature.[361] Despite the wide range of molecular electrocatalysts developed for the production of CO and HCOOH/HCOO$^-$, extensive studies focusing on the efficient production of the multi e$^-$-transfer (>2e$^-$) products such as HCHO, CH$_3$OH, and CH$_4$ are limited. An example of a commonly applied molecular electrocatalyst for the electroreduction of CO$_2$ is the polypyridyl TM complexes.[421] Generally, this set of electrocatalysts possess high CRR efficiency towards CO

generation with more promising activity in aprotic solvents. Besides, given the low solubility of CO_2 in aqueous solutions these brands of electrocatalysts are seldom used in aqueous electrolytes.[423]

Another major disadvantage of molecular electrocatalysts is the poor recyclability and stability of the catalyst systems.[424] Exploiting recent advancements in ligand mobilization, newly developed hybrid catalysts anchored on conductive supports have demonstrated more extended CRR stability.[425,426] For instance, Wang and co-workers appended the Co^{II} quaterpyridine complex $[Co(qpy)]^{2+}$ on the surface of multi-walled CNTs to catalyze the electroreduction of CO_2 to generate CO in water at pH 7.3. Experimental results revealed that the hybrid complex attained 100% selectivity and 100% FE with a current density of 0.94 mA cm^{-2} at -0.35 V (vs. RHE). Moreover, a current density of 9.3 mA cm^{-2} at an overpotential of only 340 mV was sustained for 89 095 catalytic cycles.[426]

In addition to the activity and selectivity, it is also pertinent to have an in-depth understanding of the mechanistic CRR pathway on each molecular electrocatalyst. A detailed insight into this is well documented in the literature.[421] Generally, the CRR mechanism can be investigated by studying the formation of intermediates using quantum chemical simulations along with electroanalytical tools and spectroscopy (such as Fourier transform infrared spectroscopy (FTIR)-spectroelectrochemistry (SEC) and UV-vis-SEC).[361,421]

4.2.3. Carbon-based electrocatalysts. Given the advantages of carbon-based electrocatalysts as stipulated in previous sections, this set of catalytic materials are also considered for catalysing the electrochemical reduction of CO_2.[355,427] Among the most prominent features of these electrocatalysts, the enabled assembly of the C atoms into diverse structures and dimensions with high chemical and mechanical strength differentiates them from others.[348] On this account, common carbon materials with intrinsic properties to support the CRR include CNTs, carbon nanofibers (CNFs), nanoporous carbon, graphene, diamond and graphene dots. More importantly, these catalysts are also doped with heteroatoms such as N,[428,429] B,[430,431] P,[432,433] S[434] and F[403] to further enhance the CRR activity and selectivity.[392]

The electrocatalytic performance of the heteroatom-doped carbon-based catalyst systems partially depends on the electronic structure of the heteroatoms in comparison to the positively charged C atoms.

In this case, the selectivity of a specific reduced product strongly depends on the active site's affinity towards the corresponding intermediate motifs. This is quite different from the conventional pristine carbon materials. Specifically, CRR reduced products involving the 2e$^-$-transfer (CO and HCOO$^-$) are typically generated over the carbon-based electrocatalyst. However, other products involving multiple e$^-$-transfer are also formed over the carbon-based electrocatalyst but with a particular composition and/or morphology.

Concerning heteroatom N-dopants, the activation of the CRR over carbon-based electrocatalysts occurs on the N-dopant.[435–437] Sun and co-workers revealed that the N-motif on the N-doped

carbon electrode enhanced the catalytic activity of the graphene-like carbon with high selectivity for CH_4 (93.5%) at -1.4 V vs. SHE (Fig. 9(i)).[348] Similarly, Duan and co-authors revealed by both theoretical and experimental studies that the pyridinic N-dopant is the most active site for the electro-reduction of CO_2 to CO.[392] More importantly, incorporating N-species into the carbon framework of the electrocatalyst has also been demonstrated to favour specific product selectivity. Wu and co-workers synthesized C_2H_4 for the first time as the major product from the CRR over a metal-free electrocatalyst. Here, 31% FE was achieved at a potential of -0.75 V (vs. RHE) over N-doped graphene quantum dots (NGQDs) in 1 M KOH.[438]

Another example involves the generation of C_2H_5OH from the electroreduction of CO_2 over metal-free N-doped mesoporous carbon with a high FE of 77% at -0.56 V (vs. RHE). As mentioned earlier, the morphology of the electrocatalyst also plays a significant role in the CRR catalytic activity. In this study, Song and co-workers also demonstrated that the cylindrical structure of the N-doped mesoporous carbon enhanced the C–C coupling effect, which resulted in the high selectivity for C_2H_5OH while suppressing the CO formation with the potential range of -0.4 to -1.0 V. Also, experimental verification depicts that the cylindrical construct of the electrocatalyst aided the easy transport of electrons which is responsible for the enhanced C–C coupling effect.[439] Besides N-dopants, other common dopants employed to improve the CRR performance of carbon-based electrocatalysts include B,[430,440] P,[432,433] S[434] and F.[403] Detailed description of the CRR activity of these catalysts and other notable CRR electrocatalysts is summarized in Table 3.

Aside from the metal-free dopants, metal-doping on the carbon-based electrocatalysts has also been studied.[441–443] For instance, Cheng and co-workers investigated a class of TMs that were atomically dispersed on N-doped CNTs (MSA-N-CNTs, where M = Ni, Co, NiCo, CoFe, and NiPt) using a new multistep pyrolysis approach. Among these materials, NiSA-N-CNTs demonstrated the most suitable CRR activity and selectivity towards CO production, achieving a turnover frequency (TOF) of 11.7 s^{-1} and an FE of 89% at -0.55 V (vs. RHE), with FE being two orders of magnitude higher than that of Ni nanoparticles supported on CNTs (Fig. 9(e) and (f)).[413]

Moreover, it was shown that the introduction of metal-based atoms could enhance both the efficiency and selectivity of the CRR process towards the production of C_2 hydrocarbons. Jiao and co-workers proposed a molecular scaffolding approach for synthesizing a carbon-based complex with synergistic active sites to promote the CRR. It was underscored that Cu, probed on graphitic carbon nitride (g-C_3N_4), served as a molecular scaffold to regulate the electronic structure of Cu. Compared to the Cu(111) surface, the prepared Cu–C_3N_4 complex is enriched with active centers that enabled CO_2 activation and further reduction to generate C_2 products. Theoretical evidence relates the good catalytic performance of the complex to the strong affinity of C-bound and O-bound intermediates to Cu and g-C_3N_4, respectively.[447]

In summary, CRR reduces CO_2 which is different from NRR that reduces N_2, but the perspective strategies as

Table 3 Summary of the performances of CRR electrocatalysts

Electrocatalyst	CRR product	Electrolyte	Faradaic efficiency (FE)	Current density at FE max (mA cm^{-2})	Overpotential	Ref.
Metal electrocatalysts						
Ag–Sn	HCOO$^-$	0.5 M NaHCO$_3$	88.3%	21.3	−0.94 V *vs.* RHE	409
Cu–Sn	HCOO$^-$	0.5 M NaHCO$_3$	87.4%	23.6	−0.99 V *vs.* RHE	409
Oxidized Co^{4-} atom-thick layer	HCOO$^-$	0.1 M Na$_2$SO$_4$	90%	10	1.24 V *vs.* RHE	386
Amorphous Cu NPs	HCOOH and C$_2$H$_5$OH	0.1 M KHCO$_3$	37% (HCOOH), 22% (C$_2$H$_5$OH)	∼4.2	−1.4 V *vs.* RHE	401
Cu(I) species	C$_2$H$_4$, C$_2$H$_5$OH and *n*-propanol	0.1 M KHCO$_3$	76% (total)	—	−1.0 V *vs.* RHE	402
Co–N$_5$	CO	0.2 M NaHCO$_3$	99.2%	6.2	−0.73 V *vs.* RHE	412
N,P-Co-doped carbon aerogels	CO	0.5 m [Bmim]PF6/MeCN	99.1%	143.6	−2.4 V *vs.* Ag/AgCl	444
[Co(qpy)]$^{2+}$	CO	0.5 M NaHCO$_3$	100%	0.94	−0.35 V *vs.* RHE	426
MoSeS	CO	[Emim]BF$_4$ (4 mol% [Emim])	45.2%	—	−1.15 V *vs.* RHE	420
MoSe$_2$			30.5%	—		
MoS$_2$			16.6%	—		
ZnN$_4$/C	CO	0.5 M KHCO$_3$	95%	4.8	−0.43 V *vs.* RHE	413
FeN$_4$/C	CO	0.1 M KHCO$_3$	90%	25	−0.8 V *vs.* RHE	414
In–N–C	Formate	0.5 M KHCO$_3$	∼80%	24.5	−1.1 V *vs.* RHE	339
AN–Cu	C$_2$H$_4$	0.1 M KHCO$_3$	38.1%	7.3	−1.08 V *vs.* RHE	399
CuAg alloy	C$_2$H$_4$ C$_2$H$_5$OH	1 M KOH	60% 25%	300	−0.7 V *vs.* RHE	404
Bi-ene	Formate	0.5 M KHCO$_3$	∼100%	72.0	−1.18 V *vs.* RHE	417
Carbon electrocatalysts						
PEI-NCNT	HCOO$^-$	0.1 M KHCO$_3$	85%	7.2	−1.8 V *vs.* SCE	428
PEI-NGCNT	HCOO$^-$	0.1 M KHCO$_3$	87%	9.5	−1.8 V *vs.* SCE	428
N-Doped graphene	HCOO$^-$	0.5 M KHCO$_3$	73%	7.5	−0.84 V *vs.* RHE	429
NCNT	HCOO$^-$ and CO	0.1 M KHCO$_3$	59% (HCOO-), 2% (CO)	3.0	−1.8 V *vs.* SCE	428
N-Doped nanodiamond	HCOO$^-$ and CH$_3$COO$^-$	0.5 M NaHCO$_3$	91.8% (total)	∼1.0	−1.0 V *vs.* RHE	445
N doped porous carbon	CO	0.5 M KHCO$_3$	98.4%	3.01	−0.55 V *vs.* RHE	446
B-Doped diamond	HCHO and HCOOH	CH$_3$OH	74% (HCHO), ∼15% (HCOOH)	—	−1.7 V *vs.* Ag/AgCl	430
B-Doped diamond	HCHO and HCOOH	0.1 M NaHCO$_3$	53.9% (HCHO), 26.1% (HCOOH)	—	−1.0 V *vs.* RHE	440
B-Doped diamond	HCOO$^-$ and CO	0.5 M KCl	94.7% (HCOO-), 0.6% (CO)	2.0	—	431
N-Doped graphene foam	CO and HCOO$^-$	0.1 M KHCO$_3$	85% (CO), 3% (HCOO-)	1.8	−0.58 V *vs.* RHE	437
F-Doped carbon	CO	0.1 M NaClO$_4$	∼90%	∼0.24	−0.62 V *vs.* RHE	403
P-Doped onion-like carbon	CO	0.5 M NaHCO$_3$	81%	*j* co ∼ 4.9	−0.90 V *vs.* SHE	433
S,N-Doped CNFs	CO	0.1 M KHCO$_3$	94%	∼100	−0.7 V *vs.* RHE	434
N,P-Fullerene-like carbon	CO	0.5 M NaHCO$_3$	83.30%	*j* co ∼ 8.52	−0.52 V *vs.* RHE	432
NiSA-N-CNTs	CO	0.5 M KHCO$_3$	91.3%	23.5	−0.7 V *vs.* RHE	413
NGQDs	CO, HCOO$^-$, CH$_4$, C$_2$H$_4$, C$_2$H$_5$OH, CH$_3$COO$^-$ and C$_3$H$_7$OH	1 M KOH	90% (total)	—	−0.75 V *vs.* RHE	438
N-Doped graphene-like carbon	CH$_4$ and CO	[Bmim]BF$_4$	93.5% (CH$_4$), 4.2% (CO)	—	−1.4 V *vs.* SHE	348
N-Doped mesoporous carbon	C$_2$H$_5$OH	0.1 M KHCO$_3$	77%	—	−0.56 V *vs.* RHE	439
B,N-Doped nanodiamond	C$_2$H$_5$OH	0.1 M NaHCO$_3$	93.20%	—	−1.0 V *vs.* RHE	440

discussed above for NRR are still laterally referenceable for CRR. Additionally, the unique characteristic for CRR lies in its product diversity, including C$_1$, C$_2$ and C$_{3+}$ carbon based products. This proffers unlimited research space, while bringing with complex challenges at the same time. From this point, the *in situ* microscopy and spectroscopy techniques will offer the robust research tools for CRR to better explore the intermediates during redox reactions and hence to enable the control on customized reaction pathways for target carbon products.

5. Conclusion and outlook

In recent years, the prospective goal to develop sustainable pathways for fuels and chemicals has given rise to the

advancements in electrocatalyst design and development. In this review, we extensively discussed the recent advances in electrocatalysis-enabled transformation of earth-abundant water, nitrogen and carbon dioxide with the sustainable goal of establishing environmentally sensible circulation of energy and materials.[445,448,449]

First, the fundamental principles, mechanistic pathways, recent theoretical concepts and the energetics underlying each electrocatalytic reaction (e.g. water splitting, N_2 reduction reaction and CO_2 reduction reaction) were initially studied to reveal the common and distinct challenges. Second, the performances of known catalyst systems pertaining to each reaction were discussed, reflecting on the different outcomes and mechanistic understanding of catalyst design principles for developing enhanced electrocatalysts. Specifically, the current status of available metal and metal-free electrocatalysts for the reactions based on a common set of figures of merit, namely yield rate, faradaic efficiency, overpotential, current density, and stability, was explored in detail. In addition, it was found that the practical implementation of each reaction and its electrocatalysts known to date is hindered by the occurrence of different adsorbed intermediates and the accompanying energies, which alters the catalytic activity and stability. For instance, the poor performance of a myriad of NRR electrocatalysts is due to the occurrence of HER which competitively consumes abundant electrons and protons to form H_2 against the formation of NH_3. This circumstance intensified the challenge in the limited depth of material knowledge and scale-up dynamics of current catalyst-development strategies. Accordingly, a new strategy in the development of catalyst systems is required to counter these constraints with a special emphasis on modulating the catalytic efficiency, selectivity and stability. Moreover, another design strategy is to construct a self-supported 3D catalyst architecture that promotes larger number of active sites and improves electrical contact. This approach may include doping, chemical functionalization, alloying or defect introduction, as well as the synthesis method and conditions. Furthermore, the need to elucidate the kinetics and reaction barriers at the electrolyte–electrode interface, together with the modalities of electron/proton transfer cannot be over-exaggerated. In this regard, one of the main conclusions is that an integrated scheme is required to strengthen both experimental and theoretical insightful tools towards the design, synthesis, characterization and testing of practical catalyst systems. In spite of significant progress made as discussed above, there are still many challenges ahead in the development of electrocatalysts for overall water splitting, CO_2 reduction and N_2 reduction reactions and further efforts are also required to elucidate other factors that can expedite the advancements. Prospective research studies in this regard can focus on the following points.

(1) An in-depth understanding of the related mechanism for each reaction is critically sought. This would in turn provide a knowledge-driven scheme for the design and development of efficient catalysts by optimizing computational studies towards the reaction mechanism. Specifically, investigation into the mechanism can guide structural modification, electronic reconfiguration and prevention of catalyst active site degradation during cycling. In addition, theoretical calculations can discern at an atomic level the competitive interactions hindering high yield in each reaction, e.g. the competitive interaction between NRR and HER in the electrocatalytic synthesis of ammonia. Most reported computational studies are based on simplified models and hence lack accurate prediction of the actual kinetics and reaction mechanisms under given operating conditions.

(2) Morphology-engineered catalyst systems have demonstrated high performance efficacy and stability in the considered electrocatalytic processes.[450,451] On this account, the catalyst with abundant active sites can be fabricated into specific configurations (such as layers, 3D, nanowires and nanotubes) in order to improve the catalyst's physiochemical properties. By doing so, the porosity and number of accessible active sites are increased, hence facilitating species adsorption, activation and electron diffusion. For instance, heteroatom doping and modulation of the composition of the catalyst alter the electronic structure of active sites so as to optimize the intrinsic activity of bifunctional HER–OER catalysts. In the case of NRR, the catalytic activity is highly dependent on the transfer of electrons, which was observed to be more effective in some special structures such as sharp spikes known to concentrate the electric field at the spikes. Hence, it is necessary to optimize the structure with respect to the morphology to end up in enhanced catalysis.

(3) Generally, extensive integration of computational and experimental studies in the design of catalyst systems is lacking, particularly in the fabrication methods for the engineered catalysts. Most reported studies in this regard are theory-based with little or no detailing of experimental schemes to effectuate the newly developed catalyst active sites. Ideally, to integrate all mechanistic information demands a rigorous standardization of experimental setups and procedures, in-depth understanding beyond surficial catalyst interactions and a multi-scale modeling involving all these aspects.

(4) Thorough knowledge-based studies on the above outlooks are essential mainly for the development of novel or improved electrocatalysts. Thereupon, the development of functional composites with better catalytic activity and stability is not far-fetched.[452] For instance, various heteroatom-doped functional carbon-based materials have displayed exceptional potential towards overall water splitting due to their tunable structure, available active sites and durability in alkaline/acidic electrolytes. Another example is the adoption of the zeolitic imidazolate encapsulated catalyst, which has the potential to suppress HER in the NRR process by absorbing H-atoms. In summary, the optimization of these advanced functional materials is vital for the practical application of these processes.

(5) In addition to the optimization of composite catalysts, measures can be adopted to expedite this process via accelerating catalyst discovery. Due to advancements in machine learning and material genome databases, accelerating catalyst discovery by high-throughput assessment and non-supervised analytical

techniques such as AI algorithms, aided with the identification of key synthetic parameters, is realistic.[453,454] Moreover, the state-of-the-art computer-aided robotic and automated facilities enable autonomous catalyst synthesis, characterization and performance evaluation, which could significantly boost the discovery of advanced catalysts for electrochemical conversion of water, nitrogen, carbon dioxide and the other molecules.[455] This critical review with more than 500 references along with groups of expertise helped to lay the foundation in this research field.

(6) Although optimizing the operating cell was not covered in detail in this study, it is worth mentioning here for future research studies. The practical application of the electrocatalytic conversion of earth-abundant molecules goes beyond the understanding of the surficial interactions on the electrocatalysts. Knowledge of the electrolytic cells and optimal operating conditions is equally vital. For instance, NH_3 is theoretically reduced and detected at the cathode. However, this is not the case practically as a significant amount of NH_3 is observed to crossover to the anode, which could be oxidized and subsequently reduce the yield of NH_3. Therefore, the need for the design and optimization of the cell is necessary to circumvent such occurrences.

(7) In view of the technical advancement in this field, researchers underscore the importance of developing more resolute legal and techno-economic frameworks that can successfully promote sustainable solutions by internalizing environmental costs. Overall, a level of parallelism between the technological, economic and legal aspects of these technologies at the initial stage of development and coordinated efforts based on a long-term view should be established. This is valuable for the practical exploitation and commercial extension of these electrochemical conversion processes. However, despite the promising laboratory-based efficiencies, particularly for the most important reaction (HER), the processes are still long way away from practical application. Recent advancements lack feasibility tests on a pilot scale for the highly efficient electrocatalysts designed to date. In addition, it is envisaged that even with the accelerated advancement in electrocatalyst development, conventionally manufactured electrocatalysts may likely exhibit a better economy of scale, hence discouraging the implementation of sensible catalyst schemes.

Conflicts of interest

There are no conflicts to declare.

Acknowledgements

References

1 S. Chen, S. S. Thind and A. Chen, *Electrochem. Commun.*, 2016, **63**, 10–17.

2 Z. J. Schiffer and K. Manthiram, *Joule*, 2019, **1**, 10–14.

3 Z. W. Seh, J. Kibsgaard, C. F. Dickens, I. Chorkendorff, J. K. Nørskov and T. F. Jaramillo, *Science*, 2017, **355**, eaad4998.

4 F. Naseem, P. Lu, J. Zeng, Z. Lu, Y. H. Ng, H. Zhao, Y. Du and Z. Yin, *ACS Nano*, 2020, **14**, 7734–7759.

5 J. Hwang, R. R. Rao, L. Giordano, Y. Katayama, Y. Yu and Y. Shao-Horn, *Science*, 2017, **358**, 751–756.

6 A. J. Martín and J. Pérez-Ramírez, *Joule*, 2019, **3**, 2602–2621.

7 H. Lu, J. Tournet, K. Dastafkan, Y. Liu, Y. H. Ng, S. K. Karuturi, C. Zhao and Z. Yin, *Chem. Rev.*, 2021, **121**, 10271–10366.

8 W. Kreuter and H. Hofmann, *Int. J. Hydrogen Energy*, 1998, **23**, 661–666.

9 J. Jordan and P. T. Smith, *Proc. Chem. Soc.*, 1960, 246–247.

10 S. Meshitsuka, M. Ichikawa and K. Tamaru, *J. Chem. Soc., Chem. Commun.*, 1974, 158–159.

11 Y. Hori, A. Murata and R. Takahashi, *J. Chem. Soc., Faraday Trans. 1*, 1989, **85**, 2309–2326.

12 H. Yoshio, K. Katsuhei and S. Shin, *Chem. Lett.*, 1985, **15**, 897–898.

13 H. Yoshio, K. Katsuhei, M. Akira and S. Shin, *Chem. Lett.*, 1986, 897–898.

14 N. Furuya and H. Yoshiba, *J. Electroanal. Chem. Interfa. Electrochem.*, 1990, **291**, 269–272.

15 J. Liu, D. Zhu, Y. Zheng, A. Vasileff and S.-Z. Qiao, *ACS Catal.*, 2018, **8**, 6707–6732.

16 M. S. Dresselhaus and I. L. Thomas, *Nature*, 2001, **414**, 332–337.

17 J. A. Turner, *Science*, 2004, **305**, 972.

18 Q. Liu, Z. Pu, A. M. Asiri, A. H. Qusti, A. O. Al-Youbi and X. Sun, *J. Nanopart. Res.*, 2013, **15**, 2057.

19 J. Tian, N. Cheng, Q. Liu, W. Xing and X. Sun, *Angew. Chem., Int. Ed.*, 2015, **54**, 5493–5497.

20 M. G. Walter, E. L. Warren, J. R. McKone, S. W. Boettcher, Q. Mi, E. A. Santori and N. S. Lewis, *Chem. Rev.*, 2010, **110**, 6446–6473.

21 M. Gong, D.-Y. Wang, C.-C. Chen, B.-J. Hwang and H. Dai, *Nano Res.*, 2016, **9**, 28–46.

22 Y. Wu, M. Chen, Y. Han, H. Luo, X. Su, M.-T. Zhang, X. Lin, J. Sun, L. Wang, L. Deng, W. Zhang and R. Cao, *Angew. Chem., Int. Ed.*, 2015, **54**, 4870–4875.

23 A. Fujishima and K. Honda, *Nature*, 1972, **238**, 37–38.

24 J. Wang, W. Cui, Q. Liu, Z. Xing, A. M. Asiri and X. Sun, *Adv. Mater.*, 2016, **28**, 215–230.

25 S. Zhang, S. E. Saji, Z. Yin, H. Zhang, Y. Du and C.-H. Yan, *Adv. Mater.*, 2021, **33**, 2005988.

26 J. Wang, X. Yue, Y. Yang, S. Sirisomboonchai, P. Wang, X. Ma, A. Abudula and G. Guan, *J. Alloys Compd.*, 2020, **819**, 153346.

27 Y. Ji, L. Yang, X. Ren, G. Cui, X. Xiong and X. Sun, *ACS Sustainable Chem. Eng.*, 2018, **6**, 9555–9559.

28 B. M. Hunter, H. B. Gray and A. M. Müller, *Chem. Rev.*, 2016, **116**, 14120–14136.

29 J. Zhang, H. Zhou, X. Liu, J. Zhang, T. Peng, J. Yang, Y. Huang and S. Mu, *J. Mater. Chem. A*, 2016, **4**, 15870–15879.

30 C. G. Morales-Guio, L.-A. Stern and X. Hu, *Chem. Soc. Rev.*, 2014, **43**, 6555–6569.

31 X. Zou and Y. Zhang, *Chem. Soc. Rev.*, 2015, **44**, 5148–5180.

32 S. Trasatti, *J. Electroanal. Chem. Int. Electrochem.*, 1972, **39**, 163–184.

33 S. Anantharaj, S. R. Ede, K. Sakthikumar, K. Karthick, S. Mishra and S. Kundu, *ACS Catal.*, 2016, **6**, 8069–8097.

34 Y. Shi and B. Zhang, *Chem. Soc. Rev.*, 2016, **45**, 1529–1541.

35 X. Chang, T. Wang, Z.-J. Zhao, P. Yang, J. Greeley, R. Mu, G. Zhang, Z. Gong, Z. Luo, J. Chen, Y. Cui, G. A. Ozin and J. Gong, *Angew. Chem., Int. Ed.*, 2018, **57**, 15415–15419.

36 T. Shinagawa, A. T. Garcia-Esparza and K. Takanabe, *Sci. Rep.*, 2015, **5**, 13801.

37 Y. Yan, B. Y. Xia, B. Zhao and X. Wang, *J. Mater. Chem. A*, 2016, **4**, 17587–17603.

38 N. T. Suen, S. F. Hung, Q. Quan, N. Zhang, Y. J. Xu and H. M. Chen, *Chem. Soc. Rev.*, 2017, **46**, 337–365.

39 J. Rossmeisl, Z. W. Qu, H. Zhu, G. J. Kroes and J. K. Nørskov, *J. Electroanal. Chem.*, 2007, **607**, 83–89.

40 I. C. Man, H.-Y. Su, F. Calle-Vallejo, H. A. Hansen, J. I. Martínez, N. G. Inoglu, J. Kitchin, T. F. Jaramillo, J. K. Nørskov and J. Rossmeisl, *ChemCatChem*, 2011, **3**, 1159–1165.

41 R. L. Doyle and M. E. G. Lyons, *Photoelectrochemical Solar Fuel Production: From Basic Principles to Advanced Devices*, Springer International Publishing, Cham, 2016, pp. 41–104.

42 Y. Matsumoto and E. Sato, *Mater. Chem. Phys.*, 1986, **14**, 397–426.

43 J. Tymoczko, V. Colic, A. Ganassin, W. Schuhmann and A. S. Bandarenka, *Catal. Today*, 2015, **244**, 96–102.

44 X. Liu and L. Dai, *Nat. Rev. Mater.*, 2016, **1**, 16064.

45 R. Paul, L. Zhu, H. Chen, J. Qu and L. Dai, *Adv. Mater.*, 2019, **31**, 1806403.

46 H. Wang, H.-W. Lee, Y. Deng, Z. Lu, P.-C. Hsu, Y. Liu, D. Lin and Y. Cui, *Nat. Commun.*, 2015, **6**, 7261.

47 K. Liu, F. Wang, P. He, T. A. Shifa, Z. Wang, Z. Cheng, X. Zhan and J. He, *Adv. Energy Mater.*, 2018, **8**, 1703290.

48 Y.-N. Zhu, C.-Y. Cao, W.-J. Jiang, S.-L. Yang, J.-S. Hu, W.-G. Song and L.-J. Wan, *J. Mater. Chem. A*, 2016, **4**, 18470–18477.

49 X. Miao, D. Qu, D. Yang, B. Nie, Y. Zhao, H. Fan and Z. Sun, *Adv. Mater.*, 2018, **30**, 1704740.

50 J. Mao, J. Iocozzia, J. Huang, K. Meng, Y. Lai and Z. Lin, *Energy Environ. Sci.*, 2018, **11**, 772–799.

51 L. Li, P. Wang, Q. Shao and X. Huang, *Chem. Soc. Rev.*, 2020, **49**, 3072–3106.

52 Z. Zhou, Z. Pei, L. Wei, S. Zhao, X. Jian and Y. Chen, *Energy Environ. Sci.*, 2020, **13**, 3185–3206.

53 B. Kim, T. Kim, K. Lee and J. Li, *ChemElectroChem*, 2020, 7, 3578–3589.

54 S. Anantharaj and V. Aravindan, *Adv. Energy Mater.*, 2020, **10**, 1902666.

55 R. Wu, B. Xiao, Q. Gao, Y. R. Zheng, X. S. Zheng, J. F. Zhu, M. R. Gao and S. H. Yu, *Angew. Chem., Int. Ed. Engl.*, 2018, **57**, 15445–15449.

56 J. Yu, J. Dai, Q. He, D. Zhao, Z. Shao and M. Ni, *Mater. Rep.: Energy*, 2021, **1**, 100024.

57 J. Tian, Q. Liu, A. M. Asiri and X. Sun, *J. Am. Chem. Soc.*, 2014, **136**, 7587–7590.

58 Y. Lee, J. Suntivich, K. J. May, E. E. Perry and Y. Shao-Horn, *J. Phys. Chem. Lett.*, 2012, **3**, 399–404.

59 Y. Xu and B. Zhang, *Chem. Soc. Rev.*, 2014, **43**, 2439–2450.

60 Y. Li, Y. Sun, Y. Qin, W. Zhang, L. Wang, M. Luo, H. Yang and S. Guo, *Adv. Energy Mater.*, 2020, **10**, 1903120.

61 J. Feng, F. Lv, W. Zhang, P. Li, K. Wang, C. Yang, B. Wang, Y. Yang, J. Zhou, F. Lin, G.-C. Wang and S. Guo, *Adv. Mater.*, 2017, **29**, 1703798.

62 J. Park, S. Choi, A. Oh, H. Jin, J. Joo, H. Baik and K. Lee, *Nanoscale Horiz.*, 2019, **4**, 727–734.

63 M. Jahan, Z. Liu and K. P. Loh, *Adv. Funct. Mater.*, 2013, **23**, 5363–5372.

64 Z. Xing, Q. Liu, A. M. Asiri and X. Sun, *Adv. Mater.*, 2014, **26**, 5702–5707.

65 M. S. Xie, B. Y. Xia, Y. Li, Y. Yan, Y. Yang, Q. Sun, S. H. Chan, A. Fisher and X. Wang, *Energy Environ. Sci.*, 2016, **9**, 1687–1695.

66 Y. Zhu, H.-C. Chen, C.-S. Hsu, T.-S. Lin, C.-J. Chang, S.-C. Chang, L.-D. Tsai and H. M. Chen, *ACS Energy Lett.*, 2019, **4**, 987–994.

67 A. Lasia and A. Rami, *J. Electroanal. Chem. Interfacial Electrochem.*, 1990, **294**, 123–141.

68 Y. Liang, X. Sun, A. M. Asiri and Y. He, *Nanotechnology*, 2016, **27**, 12LT01.

69 B. C. M. Martindale and E. Reisner, *Adv. Energy Mater.*, 2016, **6**, 1502095.

70 C. Tang, N. Cheng, Z. Pu, W. Xing and X. Sun, *Angew. Chem., Int. Ed.*, 2015, **54**, 9351–9355.

71 C. Zhao, X. Dai, T. Yao, W. Chen, X. Wang, J. Wang, J. Yang, S. Wei, Y. Wu and Y. Li, *J. Am. Chem. Soc.*, 2017, **139**, 8078–8081.

72 N. Yang, C. Tang, K. Wang, G. Du, A. M. Asiri and X. Sun, *Nano Res.*, 2016, **9**, 3346–3354.

73 L. Yang, H. Qi, C. Zhang and X. Sun, *Nanotechnology*, 2016, **27**, 23LT01.

74 T. Liu, L. Xie, J. Yang, R. Kong, G. Du, A. M. Asiri, X. Sun and L. Chen, *ChemElectroChem*, 2017, **4**, 1840–1845.

75 W. Lu, T. Liu, L. Xie, C. Tang, D. Liu, S. Hao, F. Qu, G. Du, Y. Ma, A. M. Asiri and X. Sun, *Small*, 2017, **13**, 1700805.

76 T. Liu, Y. Liang, Q. Liu, X. Sun, Y. He and A. M. Asiri, *Electrochem. Commun.*, 2015, **60**, 92–96.

77 P. Jiang, Q. Liu, Y. Liang, J. Tian, A. M. Asiri and X. Sun, *Angew. Chem., Int. Ed.*, 2014, **53**, 12855–12859.

78 F. Gloaguen, J. D. Lawrence and T. B. Rauchfuss, *J. Am. Chem. Soc.*, 2001, **123**, 9476–9477.

79 S.-K. Lee, S. D. George, W. E. Antholine, B. Hedman, K. O. Hodgson and E. I. Solomon, *J. Am. Chem. Soc.*, 2002, **124**, 6180–6193.

80 D. Gao, R. Liu, J. Biskupek, U. Kaiser, Y.-F. Song and C. Streb, *Angew. Chem., Int. Ed.*, 2019, **58**, 4644–4648.

81 S. Chao, Z. Bai, Q. Cui, H. Yan, K. Wang and L. Yang, *Carbon*, 2015, **82**, 77–86.

82 X. Zou, X. Huang, A. Goswami, R. Silva, B. R. Sathe, E. Mikmeková and T. Asefa, *Angew. Chem., Int. Ed.*, 2014, **53**, 4372–4376.

83 X. Lu and C. Zhao, *Nat. Commun.*, 2015, **6**, 6616.

84 R. D. L. Smith, M. S. Prévot, R. D. Fagan, S. Trudel and C. P. Berlinguette, *J. Am. Chem. Soc.*, 2013, **135**, 11580–11586.

85 C. Tang, A. M. Asiri, Y. Luo and X. Sun, *ChemNanoMat*, 2015, **1**, 558–561.

86 C. Tang, Z. Pu, Q. Liu, A. M. Asiri and X. Sun, *Electrochim. Acta*, 2015, **153**, 508–514.

87 L.-L. Feng, G. Yu, Y. Wu, G.-D. Li, H. Li, Y. Sun, T. Asefa, W. Chen and X. Zou, *J. Am. Chem. Soc.*, 2015, **137**, 14023–14026.

88 W. Zhou, X.-J. Wu, X. Cao, X. Huang, C. Tan, J. Tian, H. Liu, J. Wang and H. Zhang, *Energy Environ. Sci.*, 2013, **6**, 2921–2924.

89 Z. Pu, Y. Luo, A. M. Asiri and X. Sun, *ACS Appl. Mater. Interfaces*, 2016, **8**, 4718–4723.

90 J. Shi, J. Hu, Y. Luo, X. Sun and A. M. Asiri, *Catal. Sci. Technol.*, 2015, **5**, 4954–4958.

91 C. Wang, M. Zhu, Z. Cao, P. Zhu, Y. Cao, X. Xu, C. Xu and Z. Yin, *Appl. Catal., B*, 2021, **291**, 120071.

92 Z. Fang, L. Peng, H. Lv, Y. Zhu, C. Yan, S. Wang, P. Kalyani, X. Wu and G. Yu, *ACS Nano*, 2017, **11**, 9550–9557.

93 J. Yang, C. Lei, H. Wang, B. Yang, Z. Li, M. Qiu, X. Zhuang, C. Yuan, L. Lei, Y. Hou and X. Feng, *Nanoscale*, 2019, **11**, 17571–17578.

94 C. Wei, C. Liu, L. Gao, Y. Sun, Q. Liu, X. Zhang and J. Guo, *J. Alloys Compd.*, 2019, **796**, 86–92.

95 W. Fang, D. Liu, Q. Lu, X. Sun and A. M. Asiri, *Electrochem. Commun.*, 2016, **63**, 60–64.

96 D. Kong, J. J. Cha, H. Wang, H. R. Lee and Y. Cui, *Energy Environ. Sci.*, 2013, **6**, 3553–3558.

97 M. A. Lukowski, A. S. Daniel, F. Meng, A. Forticaux, L. Li and S. Jin, *J. Am. Chem. Soc.*, 2013, **135**, 10274–10277.

98 T. Wang, J. Zhuo, K. Du, B. Chen, Z. Zhu, Y. Shao and M. Li, *Adv. Mater.*, 2014, **26**, 3761–3766.

99 D. Kong, H. Wang, J. J. Cha, M. Pasta, K. J. Koski, J. Yao and Y. Cui, *Nano Lett.*, 2013, **13**, 1341–1347.

100 W. F. Chen, C. H. Wang, K. Sasaki, N. Marinkovic, W. Xu, J. T. Muckerman, Y. Zhu and R. R. Adzic, *Energy Environ. Sci.*, 2013, **6**, 943–951.

101 T. A. Shifa, F. Wang, K. Liu, K. Xu, Z. Wang, X. Zhan, C. Jiang and J. He, *Small*, 2016, **12**, 3802–3809.

102 Y. Sun, C. Liu, D. C. Grauer, J. Yano, J. R. Long, P. Yang and C. J. Chang, *J. Am. Chem. Soc.*, 2013, **135**, 17699–17702.

103 A. Ambrosi, C. K. Chua, A. Bonanni and M. Pumera, *Chem. Rev.*, 2014, **114**, 7150–7188.

104 S. Peng, L. Li, X. Han, W. Sun, M. Srinivasan, S. G. Mhaisalkar, F. Cheng, Q. Yan, J. Chen and S. Ramakrishna, *Angew. Chem., Int. Ed.*, 2014, **53**, 12594–12599.

105 C. Zequine, S. Bhoyate, F. Wang, X. Li, K. Siam, P. K. Kahol and R. K. Gupta, *J. Alloys Compd.*, 2019, **784**, 1–7.

106 Z. Peng, D. Jia, A. M. Al-Enizi, A. A. Elzatahry and G. Zheng, *Adv. Energy Mater.*, 2015, **5**, 1402031.

107 D. Kong, H. Wang, Z. Lu and Y. Cui, *J. Am. Chem. Soc.*, 2014, **136**, 4897–4900.

108 Q. Liu, J. Shi, J. Hu, A. M. Asiri, Y. Luo and X. Sun, *ACS Appl. Mater. Interfaces*, 2015, **7**, 3877–3881.

109 Y.-F. Xu, M.-R. Gao, Y.-R. Zheng, J. Jiang and S.-H. Yu, *Angew. Chem., Int. Ed.*, 2013, **52**, 8546–8550.

110 M.-R. Gao, J.-X. Liang, Y.-R. Zheng, Y.-F. Xu, J. Jiang, Q. Gao, J. Li and S.-H. Yu, *Nat. Commun.*, 2015, **6**, 5982.

111 M.-R. Gao, Y.-F. Xu, J. Jiang, Y.-R. Zheng and S.-H. Yu, *J. Am. Chem. Soc.*, 2012, **134**, 2930–2933.

112 M.-R. Gao, X. Cao, Q. Gao, Y.-F. Xu, Y.-R. Zheng, J. Jiang and S.-H. Yu, *ACS Nano*, 2014, **8**, 3970–3978.

113 H. Liang, F. Meng, M. Cabán-Acevedo, L. Li, A. Forticaux, L. Xiu, Z. Wang and S. Jin, *Nano Lett.*, 2015, **15**, 1421–1427.

114 D. Liu, Q. Lu, Y. Luo, X. Sun and A. M. Asiri, *Nanoscale*, 2015, **7**, 15122–15126.

115 J. Zhang, T. Wang, D. Pohl, B. Rellinghaus, R. Dong, S. Liu, X. Zhuang and X. Feng, *Angew. Chem., Int. Ed.*, 2016, **55**, 6702–6707.

116 F. Du, L. Shi, Y. Zhang, T. Li, J. Wang, G. Wen, A. Alsaedi, T. Hayat, Y. Zhou and Z. Zou, *Appl. Catal., B*, 2019, **253**, 246–252.

117 Y. V. Kaneti, Y. Guo, N. L. W. Septiani, M. Iqbal, X. Jiang, T. Takei, B. Yuliarto, Z. A. Alothman, D. Golberg and Y. Yamauchi, *Chem. Eng. J.*, 2021, **405**, 126580.

118 N. L. W. Septiani, Y. V. Kaneti, K. B. Fathoni, K. Kani, A. E. Allah, B. Yuliarto, Nugraha, H. K. Dipojono, Z. A. Alothman, D. Golberg and Y. Yamauchi, *Chem. Mater.*, 2020, **32**, 7005–7018.

119 P. Bhanja, Y. Kim, B. Paul, J. Lin, S. M. Alshehri, T. Ahamad, Y. V. Kaneti, A. Bhaumik and Y. Yamauchi, *ChemCatChem*, 2020, **12**, 2091–2096.

120 N. L. W. Septiani, Y. V. Kaneti, K. B. Fathoni, Y. Guo, Y. Ide, B. Yuliarto, X. Jiang, Nugraha, H. K. Dipojono, D. Golberg and Y. Yamauchi, *J. Mater. Chem. A*, 2020, **8**, 3035–3047.

121 M. W. Kanan and D. G. Nocera, *Science*, 2008, **321**, 1072.

122 M. W. Kanan, Y. Surendranath and D. G. Nocera, *Chem. Soc. Rev.*, 2009, **38**, 109–114.

123 S. Cobo, J. Heidkamp, P.-A. Jacques, J. Fize, V. Fourmond, L. Guetaz, B. Jousselme, V. Ivanova, H. Dau, S. Palacin, M. Fontecave and V. Artero, *Nat. Mater.*, 2012, **11**, 802–807.

124 L. Song, S. Zhang, X. Wu and K. Wang, *Vacuum*, 2015, **112**, 12–16.

125 J. A. Cecilia, A. Infantes-Molina, E. Rodríguez-Castellón and A. Jiménez-López, *Appl. Catal., B*, 2009, **92**, 100–113.

126 W. Li, D. Xiong, X. Gao and L. Liu, *Chem. Commun.*, 2019, **55**, 8744–8763.

127 A. Dutta and N. Pradhan, *J. Phys. Chem. Lett.*, 2017, **8**, 144–152.

128 J. Xu, J. Li, D. Xiong, B. Zhang, Y. Liu, K.-H. Wu, I. Amorim, W. Li and L. Liu, *Chem. Sci.*, 2018, **9**, 3470–3476.

129 E. J. Popczun, C. G. Read, C. W. Roske, N. S. Lewis and R. E. Schaak, *Angew. Chem., Int. Ed.*, 2014, **53**, 5427–5430.

130 Z. Huang, Z. Chen, Z. Chen, C. Lv, M. G. Humphrey and C. Zhang, *Nano Energy*, 2014, **9**, 373–382.

131 J. F. Callejas, C. G. Read, E. J. Popczun, J. M. McEnaney and R. E. Schaak, *Chem. Mater.*, 2015, **27**, 3769–3774.

132 Z. Huang, Z. Chen, Z. Chen, C. Lv, H. Meng and C. Zhang, *ACS Nano*, 2014, **8**, 8121–8129.

133 L. Feng, H. Vrubel, M. Bensimon and X. Hu, *Phys. Chem. Chem. Phys.*, 2014, **16**, 5917–5921.

134 T. Liu, D. Liu, F. Qu, D. Wang, L. Zhang, R. Ge, S. Hao, Y. Ma, G. Du, A. M. Asiri, L. Chen and X. Sun, *Adv. Energy Mater.*, 2017, **7**, 1700020.

135 Z. D. Wei, A. Z. Yan, Y. C. Feng, L. Li, C. X. Sun, Z. G. Shao and P. K. Shen, *Electrochem. Commun.*, 2007, **9**, 2709–2715.

136 L.-A. Stern, L. Feng, F. Song and X. Hu, *Energy Environ. Sci.*, 2015, **8**, 2347–2351.

137 C. Tang, R. Zhang, W. Lu, Z. Wang, D. Liu, S. Hao, G. Du, A. M. Asiri and X. Sun, *Angew. Chem., Int. Ed.*, 2017, **56**, 842–846.

138 M. Ledendecker, S. Krick Calderón, C. Papp, H.-P. Steinrück, M. Antonietti and M. Shalom, *Angew. Chem., Int. Ed.*, 2015, **54**, 12361–12365.

139 G.-F. Chen, T. Y. Ma, Z.-Q. Liu, N. Li, Y.-Z. Su, K. Davey and S.-Z. Qiao, *Adv. Funct. Mater.*, 2016, **26**, 3314–3323.

140 Q. Liu, J. Tian, W. Cui, P. Jiang, N. Cheng, A. M. Asiri and X. Sun, *Angew. Chem., Int. Ed.*, 2014, **53**, 6710–6714.

141 Y. Yan, B. Y. Xia, X. Ge, Z. Liu, A. Fisher and X. Wang, *Chem. – Eur. J.*, 2015, **21**, 18062–18067.

142 C. G. Read, J. F. Callejas, C. F. Holder and R. E. Schaak, *ACS Appl. Mater. Interfaces*, 2016, **8**, 12798–12803.

143 T. A. Shifa, K. Yusupov, G. Solomon, A. Gradone, R. Mazzaro, E. Cattaruzza and A. Vomiero, *ACS Catal.*, 2021, **11**, 4520–4529.

144 D. J. Ham and J. S. Lee, *Energies*, 2009, **2**, 873–899.

145 W.-F. Chen, J. T. Muckerman and E. Fujita, *Chem. Commun.*, 2013, **49**, 8896–8909.

146 P. Chen, K. Xu, Z. Fang, Y. Tong, J. Wu, X. Lu, X. Peng, H. Ding, C. Wu and Y. Xie, *Angew. Chem., Int. Ed.*, 2015, **54**, 14710–14714.

147 K. Xu, P. Chen, X. Li, Y. Tong, H. Ding, X. Wu, W. Chu, Z. Peng, C. Wu and Y. Xie, *J. Am. Chem. Soc.*, 2015, **137**, 4119–4125.

148 Q. Zhang, Y. Wang, Y. Wang, A. M. Al-Enizi, A. A. Elzatahry and G. Zheng, *J. Mater. Chem. A*, 2016, **4**, 5713–5718.

149 B. Cao, G. M. Veith, J. C. Neuefeind, R. R. Adzic and P. G. Khalifah, *J. Am. Chem. Soc.*, 2013, **135**, 19186–19192.

150 W.-F. Chen, K. Sasaki, C. Ma, A. I. Frenkel, N. Marinkovic, J. T. Muckerman, Y. Zhu and R. R. Adzic, *Angew. Chem., Int. Ed.*, 2012, **51**, 6131–6135.

151 X. Jia, Y. Zhao, G. Chen, L. Shang, R. Shi, X. Kang, G. I. N. Waterhouse, L.-Z. Wu, C.-H. Tung and T. Zhang, *Adv. Energy Mater.*, 2016, **6**, 1502585.

152 M. C. Weidman, D. V. Esposito, Y.-C. Hsu and J. G. Chen, *J. Power Sources*, 2012, **202**, 11–17.

153 E. C. Weigert, D. V. Esposito and J. G. Chen, *J. Power Sources*, 2009, **193**, 501–506.

154 L. Liao, S. Wang, J. Xiao, X. Bian, Y. Zhang, M. D. Scanlon, X. Hu, Y. Tang, B. Liu and H. H. Girault, *Energy Environ. Sci.*, 2014, **7**, 387–392.

155 H. Vrubel and X. Hu, *Angew. Chem., Int. Ed.*, 2012, **51**, 12703–12706.

156 B. Wang, X. Wu, X. Zhang, G. Pang and S. Li, *New J. Chem.*, 2020, **44**, 1147–1156.

157 J.-S. Li, L.-X. Kong, Z. Wu, S. Zhang, X.-Y. Yang, J.-Q. Sha and G.-D. Liu, *Carbon*, 2019, **145**, 694–700.

158 Z.-Y. Wu, W.-B. Ji, B.-C. Hu, H.-W. Liang, X.-X. Xu, Z.-L. Yu, B.-Y. Li and S.-H. Yu, *Nano Energy*, 2018, **51**, 286–293.

159 C. Tang and S.-Z. Qiao, *Matter*, 2019, **1**, 1454–1455.

160 J. Zhang, L. Qu, G. Shi, J. Liu, J. Chen and L. Dai, *Angew. Chem., Int. Ed.*, 2016, **55**, 2230–2234.

161 Y. Zheng, Y. Jiao, Y. Zhu, L. H. Li, Y. Han, Y. Chen, A. Du, M. Jaroniec and S. Z. Qiao, *Nat. Commun.*, 2014, **5**, 3783.

162 R. Wu, J. Zhang, Y. Shi, D. Liu and B. Zhang, *J. Am. Chem. Soc.*, 2015, **137**, 6983–6986.

163 J. Lai, S. Li, F. Wu, M. Saqib, R. Luque and G. Xu, *Energy Environ. Sci.*, 2016, **9**, 1210–1214.

164 S. Chen, J. Duan, M. Jaroniec and S. Z. Qiao, *Angew. Chem., Int. Ed.*, 2013, **52**, 13567–13570.

165 X. Sun, F. Liu, X. Chen, C. Li, J. Yu and M. Pan, *Electrochim. Acta*, 2019, **307**, 206–213.

166 Y. Sun, B. Huang, Y. Li, Y. Xing, M. Luo, N. Li, Z. Xia, Y. Qin, D. Su, L. Wang and S. Guo, *Chem. Mater.*, 2019, **31**, 8136–8144.

167 J. Ding, Q. Shao, Y. Feng and X. Huang, *Nano Energy*, 2018, **47**, 1–7.

168 P. W. Menezes, C. Panda, S. Garai, C. Walter, A. Guiet and M. Driess, *Angew. Chem., Int. Ed.*, 2018, **57**, 15237–15242.

169 X. Wang, F. Li, W. Li, W. Gao, Y. Tang and R. Li, *J. Mater. Chem. A*, 2017, **5**, 17982–17989.

170 Y. Liu, S. Jiang, S. Li, L. Zhou, Z. Li, J. Li and M. Shao, *Appl. Catal., B*, 2019, **247**, 107–114.

171 Y. Guo, X. Zhou, J. Tang, S. Tanaka, Y. V. Kaneti, J. Na, B. Jiang, Y. Yamauchi, Y. Bando and Y. Sugahara, *Nano Energy*, 2020, **75**, 104913.

172 Y. Gong, Z. Yang, Y. Lin, T. Zhou, J. Li, F. Jiao and W. Wang, *Dalton Trans.*, 2019, **48**, 7025.

173 F. Li, R. Xu, Y. Li, F. Liang, D. Zhang, W.-F. Fu and X.-J. Lv, *Carbon*, 2019, **145**, 521–528.

174 X. Wang, W. Li, D. Xiong and L. Liu, *J. Mater. Chem. A*, 2016, **4**, 5639–5646.

175 A. Chunduri, S. Gupta, O. Bapat, A. Bhide, R. Fernandes, M. K. Patel, V. Bambole, A. Miotello and N. Patel, *Appl. Catal., B*, 2019, **259**, 118051.

176 P. W. Menezes, A. Indra, I. Zaharieva, C. Walter, S. Loos, S. Hoffmann, R. Schlögl, H. Dau and M. Driess, *Energy Environ. Sci.*, 2019, **12**, 988–999.

177 R. Zhang, J. Huang, G. Chen, W. Chen, C. Song, C. Li and K. Ostrikov, *Appl. Catal., B*, 2019, **254**, 414–423.

178 A. Wu, Y. Xie, H. Ma, C. Tian, Y. Gu, H. Yan, X. Zhang, G. Yang and H. Fu, *Nano Energy*, 2018, **44**, 353–363.

179 J. Xing, Y. Li, S. Guo, T. Jin, H. Li, Y. Wang and L. Jiao, *Electrochim. Acta*, 2019, **298**, 305–312.

180 M. A. R. Anjum, M. H. Lee and J. S. Lee, *ACS Catal.*, 2018, **8**, 8296–8305.

181 L. Hui, Y. Xue, B. Huang, H. Yu, C. Zhang, D. Zhang, D. Jia, Y. Zhao, Y. Li, H. Liu and Y. Li, *Nat. Commun.*, 2018, **9**, 5309.

182 R. Matsuoka, R. Sakamoto, K. Hoshiko, S. Sasaki, H. Masunaga, K. Nagashio and H. Nishihara, *J. Am. Chem. Soc.*, 2017, **139**, 3145–3152.

183 G. Li, Y. Li, H. Liu, Y. Guo, Y. Li and D. Zhu, *Chem. Commun.*, 2010, **46**, 3256–3258.

184 H.-Y. Si, Q.-X. Deng, L.-C. Chen, L. Wang, X.-Y. Liu, W.-S. Wu, Y.-H. Zhang, J.-M. Zhou and H.-L. Zhang, *J. Alloys Compd.*, 2019, **794**, 261–267.

185 R. F. Service, *Science*, 2014, **345**, 610.

186 Y. Liu, Y. Su, X. Quan, X. Fan, S. Chen, H. Yu, H. Zhao, Y. Zhang and J. Zhao, *ACS Catal.*, 2018, **8**, 1186–1191.

187 I. Dybkjaer, *Ammonia, catalysis and manufacture* ed. A. Nielsen, Springer, Heidelberg, 1995, pp. 199–308.

188 R. Zhao, H. Xie, L. Chang, X. Zhang, X. Zhu, X. Tong, T. Wang, Y. Luo, P. Wei, Z. Wang and X. Sun, *EnergyChem*, 2019, **1**, 100011.

189 C. J. M. van der Ham, M. T. M. Koper and D. G. H. Hetterscheid, *Chem. Soc. Rev.*, 2014, **43**, 5183–5191.

190 H. J. M. van Grinsven, L. Bouwman, K. G. Cassman, H. M. van Es, M. L. McCrackin and A. H. W. Beusen, *J. Environ. Qual.*, 2015, **44**, 356–367.

191 R. Qin, P. Liu, G. Fu and N. Zheng, *Small Methods*, 2018, **2**, 1700286.

192 Q. Li, L. He, C. Sun and X. Zhang, *J. Phys. Chem. C*, 2017, **121**, 27563–27568.

193 J. Zhao and Z. Chen, *J. Am. Chem. Soc.*, 2017, **139**, 12480–12487.

194 B. H. R. Suryanto, H.-L. Du, D. Wang, J. Chen, A. N. Simonov and D. R. MacFarlane, *Nat. Catal.*, 2019, **2**, 290–296.

195 D. Wang, L. M. Azofra, M. Harb, L. Cavallo, X. Zhang, B. H. R. Suryanto and D. R. MacFarlane, *ChemSusChem*, 2018, **11**, 3416–3422.

196 M. A. Shipman and M. D. Symes, *Catal. Today*, 2017, **286**, 57–68.

197 X. Guo, H. Du, F. Qu and J. Li, *J. Mater. Chem. A*, 2019, **7**, 3531–3543.

198 T. Spatzal, M. Aksoyoglu, L. Zhang, S. L. A. Andrade, E. Schleicher, S. Weber, D. C. Rees and O. Einsle, *Science*, 2011, **334**, 940.

199 L. C. Seefeldt, B. M. Hoffman and D. R. Dean, *Annu. Rev. Biochem.*, 2009, **78**, 701–722.

200 K. Kugler, B. Ohs, M. Scholz and M. Wessling, *Phys. Chem. Chem. Phys.*, 2014, **16**, 6129–6138.

201 E. Skúlason, T. Bligaard, S. Gudmundsdóttir, F. Studt, J. Rossmeisl, F. Abild-Pedersen, T. Vegge, H. Jónsson and J. K. Nørskov, *Phys. Chem. Chem. Phys.*, 2012, **14**, 1235–1245.

202 P. Wang, F. Chang, W. Gao, J. Guo, G. Wu, T. He and P. Chen, *Nat. Chem.*, 2017, **9**, 64–70.

203 G. Ertl, *Catal. Rev.*, 1980, **21**, 201–223.

204 D. Senthil Raja, H.-W. Lin and S.-Y. Lu, *Nano Energy*, 2019, **57**, 1–13.

205 Y. Abghoui, A. L. Garden, V. F. Hlynsson, S. Björgvinsdóttir, H. Ólafsdóttir and E. Skúlason, *Phys. Chem. Chem. Phys.*, 2015, **17**, 4909–4918.

206 Á. B. Höskuldsson, Y. Abghoui, A. B. Gunnarsdóttir and E. Skúlason, *ACS Sustainable Chem. Eng.*, 2017, **5**, 10327–10333.

207 L. Huang, J. Wu, P. Han, A. M. Al-Enizi, T. M. Almutairi, L. Zhang and G. Zheng, *Small Methods*, 2019, **3**, 1800386.

208 M. Zhu, Q. Shao, Y. Qian and X. Huang, *Nano Energy*, 2019, **56**, 330–337.

209 J. Han, Z. Liu, Y. Ma, G. Cui, F. Xie, F. Wang, Y. Wu, S. Gao, Y. Xu and X. Sun, *Nano Energy*, 2018, **52**, 264–270.

210 W. Kong, Z. Liu, J. Han, L. Xia, Y. Wang, Q. Liu, X. Shi, Y. Wu, Y. Xu and X. Sun, *Inorg. Chem. Front.*, 2019, **6**, 423–427.

211 C. Ling, Y. Ouyang, Q. Li, X. Bai, X. Mao, A. Du and J. Wang, *Small Methods*, 2019, **3**, 1800376.

212 Y. Abghoui, A. L. Garden, J. G. Howalt, T. Vegge and E. Skúlason, *ACS Catal.*, 2016, **6**, 635–646.

213 H.-L. Du, T. R. Gengenbach, R. Hodgetts, D. R. MacFarlane and A. N. Simonov, *ACS Sustainable Chem. Eng.*, 2019, **7**, 6839–6850.

214 C. J. H. Jacobsen, *Chem. Commun.*, 2000, 1057–1058.

215 C. D. Zeinalipour-Yazdi, J. S. J. Hargreaves and C. R. A. Catlow, *J. Phys. Chem. C*, 2015, **119**, 28368–28376.

216 L. F. Greenlee, J. N. Renner and S. L. Foster, *ACS Catal.*, 2018, **8**, 7820–7827.

217 S. E. Saji, H. Lu, Z. Lu, A. Carroll and Z. Yin, *Small Methods*, 2021, **5**, 2000694.

218 W. Guo, K. Zhang, Z. Liang, R. Zou and Q. Xu, *Chem. Soc. Rev.*, 2019, **48**, 5658–5716.

219 C. Tang and S.-Z. Qiao, *Joule*, 2019, **3**, 1573–1575.

220 S. Z. Andersen, V. Čolić, S. Yang, J. A. Schwalbe, A. C. Nielander, J. M. McEnaney, K. Enemark-Rasmussen, J. G. Baker, A. R. Singh, B. A. Rohr, M. J. Statt, S. J. Blair, S. Mezzavilla, J. Kibsgaard, P. C. K. Vesborg, M. Cargnello, S. F. Bent, T. F. Jaramillo, I. E. L. Stephens, J. K. Nørskov and I. Chorkendorff, *Nature*, 2019, **570**, 504–508.

221 S. Z. Andersen, M. J. Statt, V. J. Bukas, S. G. Shapel, J. B. Pedersen, K. Krempl, M. Saccoccio, D. Chakraborty, J. Kibsgaard, P. C. K. Vesborg, J. Nørskov and I. Chorkendorff, *Energy Environ. Sci.*, 2020, **13**, 4291–4300.

222 M. Shao, Y. Shao, W. Chen, K. L. Ao, R. Tong, Q. Zhu, I. N. Chan, W. F. Ip, X. Shi and H. Pan, *Phys. Chem. Chem. Phys.*, 2018, **20**, 14504–14512.

223 D. Bao, Q. Zhang, F.-L. Meng, H.-X. Zhong, M.-M. Shi, Y. Zhang, J.-M. Yan, Q. Jiang and X.-B. Zhang, *Adv. Mater.*, 2017, **29**, 1604799.

224 J. H. Montoya, C. Tsai, A. Vojvodic and J. K. Nørskov, *ChemSusChem*, 2015, **8**, 2180–2186.

225 Á. Logadóttir and J. K. Nørskov, *J. Catal.*, 2003, **220**, 273–279.

226 H. Wang, H. Yu, Z. Wang, Y. Li, Y. Xu, X. Li, H. Xue and L. Wang, *Small*, 2019, **15**, 1804769.

227 M. Nazemi and M. A. El-Sayed, *J. Phys. Chem. Lett.*, 2018, **9**, 5160–5166.

228 J. Wang, L. Yu, L. Hu, G. Chen, H. Xin and X. Feng, *Nat. Commun.*, 2018, **9**, 1795.

229 M.-M. Shi, D. Bao, S.-J. Li, B.-R. Wulan, J.-M. Yan and Q. Jiang, *Adv. Energy Mater.*, 2018, **8**, 1800124.

230 Z. Geng, Y. Liu, X. Kong, P. Li, K. Li, Z. Liu, J. Du, M. Shu, R. Si and J. Zeng, *Adv. Mater.*, 2018, **30**, 1870301.

231 N. Zhang, L. Li, J. Wang, Z. Hu, Q. Shao, X. Xiao and X. Huang, *Angew. Chem.*, 2020, **59**, 8066–8071.

232 H. Huang, L. Xia, X. Shi, A. M. Asiri and X. Sun, *Chem. Commun.*, 2018, **54**, 11427–11430.

233 X. Li, H. Xie and J. Mao, *J. Mater. Sci.*, 2020, **55**, 5203–5210.

234 F. Akagi, T. Matsuo and H. Kawaguchi, *Angew. Chem., Int. Ed.*, 2007, **46**, 8778–8781.

235 T. Shima, S. Hu, G. Luo, X. Kang, Y. Luo and Z. Hou, *Science*, 2013, **340**, 1549.

236 Y. Kobayashi, Y. Tang, T. Kageyama, H. Yamashita, N. Masuda, S. Hosokawa and H. Kageyama, *J. Am. Chem. Soc.*, 2017, **139**, 18240–18246.

237 C. J. H. Jacobsen, S. Dahl, B. S. Clausen, S. Bahn, A. Logadottir and J. K. Nørskov, *J. Am. Chem. Soc.*, 2001, **123**, 8404–8405.

238 C. I. Ezeh, X. Yang, J. He, C. Snape and X. M. Cheng, *Ultrason. Sonochem.*, 2018, **42**, 48–56.

239 R. Schlögl, *Angew. Chem., Int. Ed.*, 2003, **42**, 2004–2008.

240 S. Back and Y. Jung, *Phys. Chem. Chem. Phys.*, 2016, **18**, 9161–9166.

241 W. Peng, M. Luo, X. Xu, K. Jiang, M. Peng, D. Chen, T. S. Chan and Y. Tan, *Adv. Energy Mater.*, 2020, **10**, 2001364.

242 J. Hou, M. Yang and J. Zhang, *Nanoscale*, 2020, **12**, 6900–6920.

243 A. P. Leontiev, O. A. Brylev and K. S. Napolskii, *Electrochim. Acta*, 2015, **155**, 466–473.

244 L. Ji, X. Shi, A. M. Asiri, B. Zheng and X. Sun, *Inorg. Chem.*, 2018, **57**, 14692–14697.

245 D. Yang, T. Chen and Z. Wang, *J. Mater. Chem. A*, 2017, **5**, 18967–18971.

246 I. Matanović, F. H. Garzon and N. J. Henson, *Phys. Chem. Chem. Phys.*, 2014, **16**, 3014–3026.

247 D. Yao, C. Tang, L. Li, B. Xia, A. Vasileff, H. Jin, Y. Zhang and S. Z. Qiao, *Adv. Energy Mater.*, 2020, **10**, 2001289.

248 Z. Fang, P. Wu, Y. Qian and G. Yu, *Angew. Chem., Int. Ed.*, 2021, **60**, 4275–4281.

249 T. J. Del Castillo, N. B. Thompson and J. C. Peters, *J. Am. Chem. Soc.*, 2016, **138**, 5341–5350.

250 J. S. Anderson, J. Rittle and J. C. Peters, *Nature*, 2013, **501**, 84–87.

251 T. M. Buscagan, P. H. Oyala and J. C. Peters, *Angew. Chem., Int. Ed.*, 2017, **56**, 6921–6926.

252 M.-T. Nguyen, N. Seriani and R. Gebauer, *Phys. Chem. Chem. Phys.*, 2015, **17**, 14317–14322.

253 S. Licht, B. Cui, B. Wang, F.-F. Li, J. Lau and S. Liu, *Science*, 2014, **345**, 637.

254 F.-F. Li and S. Licht, *Inorg. Chem.*, 2014, **53**, 10042–10044.

255 J. Kong, A. Lim, C. Yoon, J. H. Jang, H. C. Ham, J. Han, S. Nam, D. Kim, Y.-E. Sung, J. Choi and H. S. Park, *ACS Sustainable Chem. Eng.*, 2017, **5**, 10986–10995.

256 S. Chen, S. Perathoner, C. Ampelli, C. Mebrahtu, D. Su and G. Centi, *Angew. Chem., Int. Ed.*, 2017, **56**, 2699–2703.

257 S. Chen, S. Perathoner, C. Ampelli, C. Mebrahtu, D. Su and G. Centi, *ACS Sustainable Chem. Eng.*, 2017, **5**, 7393–7400.

258 F. Zhou, L. M. Azofra, M. Ali, M. Kar, A. N. Simonov, C. McDonnell-Worth, C. Sun, X. Zhang and D. R. MacFarlane, *Energy Environ. Sci.*, 2017, **10**, 2516–2520.

259 B. T. Hang and D. H. Thang, *J. Alloys Compd.*, 2016, **655**, 44–49.

260 X. Cui, C. Tang, X.-M. Liu, C. Wang, W. Ma and Q. Zhang, *Chem. – Eur. J.*, 2018, **24**, 18494–18501.

261 X. Zhu, Z. Liu, Q. Liu, Y. Luo, X. Shi, A. M. Asiri, Y. Wu and X. Sun, *Chem. Commun.*, 2018, **54**, 11332–11335.

262 X. Zhu, J. Zhao, L. Ji, T. Wu, T. Wang, S. Gao, A. A. Alshehri, K. A. Alzahrani, Y. Luo, Y. Xiang, B. Zheng and X. Sun, *Nano Res.*, 2020, **13**, 209–214.

263 K. Ogura, J. R. Ferrell, A. V. Cugini, E. S. Smotkin and M. D. Salazar-Villalpando, *Electrochim. Acta*, 2010, **56**, 381–386.

264 X. Zhu, Z. Liu, H. Wang, R. Zhao, H. Chen, T. Wang, F. Wang, Y. Luo, Y. Wu and X. Sun, *Chem. Commun.*, 2019, **55**, 3987–3990.

265 X. Xiang, Z. Wang, X. Shi, M. Fan and X. Sun, *ChemCatChem*, 2018, **10**, 4530–4535.

266 X. Tang, R. Jia, T. Zhai and H. Xia, *ACS Appl. Mater. Interfaces*, 2015, **7**, 27518–27525.

267 L. Hu, A. Khaniya, J. Wang, G. Chen, W. E. Kaden and X. Feng, *ACS Catal.*, 2018, **8**, 9312–9319.

268 X. P. Wang, Y. Hu and J. Chen, *Int. Arch. Photogramm. Remote Sens. Spatial Inf. Sci.*, 2018, **XLII-3**, 1795–1798.

269 X.-F. Li, Q.-K. Li, J. Cheng, L. Liu, Q. Yan, Y. Wu, X.-H. Zhang, Z.-Y. Wang, Q. Qiu and Y. Luo, *J. Am. Chem. Soc.*, 2016, **138**, 8706–8709.

270 J. Zhao, L. Zhang, X.-Y. Xie, X. Li, Y. Ma, Q. Liu, W.-H. Fang, X. Shi, G. Cui and X. Sun, *J. Mater. Chem. A*, 2018, **6**, 24031–24035.

271 W. Li, Y. Bai, Y. Li, C. Liu, K.-Y. Chan, X. Feng and X. Lu, *J. Mater. Chem.*, 2012, **22**, 4025–4031.

272 X. Zhang, Q. Liu, X. Shi, A. M. Asiri, Y. Luo, X. Sun and T. Li, *J. Mater. Chem. A*, 2018, **6**, 17303–17306.

273 K. Jia, Y. Wang, Q. Pan, B. Zhong, Y. Luo, G. Cui, X. Guo and X. Sun, *Nanoscale Adv.*, 2019, **1**, 961–964.

274 Y. Wang, K. Jia, Q. Pan, Y. Xu, Q. Liu, G. Cui, X. Guo and X. Sun, *ACS Sustainable Chem. Eng.*, 2019, **7**, 117–122.

275 L. Zhang, X. Ji, X. Ren, Y. Ma, X. Shi, Z. Tian, A. M. Asiri, L. Chen, B. Tang and X. Sun, *Adv. Mater.*, 2018, **30**, 1800191.

276 F. Lai, W. Zong, G. He, Y. Xu, H. Huang, B. Weng, D. Rao, J. A. Martens, J. Hofkens, I. P. Parkin and T. Liu, *Angew. Chem., Int. Ed.*, 2020, **59**, 13320–13327.

277 H. Cheng, L.-X. Ding, G.-F. Chen, L. Zhang, J. Xue and H. Wang, *Adv. Mater.*, 2018, **30**, 1803694.

278 X. Yang, J. Nash, J. Anibal, M. Dunwell, S. Kattel, E. Stavitski, K. Attenkofer, J. G. Chen, Y. Yan and B. Xu, *J. Am. Chem. Soc.*, 2018, **140**, 13387–13391.

279 S. Zhang, W. Gong, Y. Lv, H. Wang, M. Han, G. Wang, T. Shi and H. Zhang, *Chem. Commun.*, 2019, **55**, 12376–12379.

280 M. Yuan, H. Zhang, D. Gao, H. He, Y. Sun, P. Lu, S. Dipazir, Q. Li, L. Zhou, S. Li, Z. Liu, J. Yang, Y. Xie, H. Zhao and G. Zhang, *J. Mater. Chem. A*, 2020, **8**, 2691–2700.

281 J. Shao, W. Sheng, M. Wang, S. Li, J. Chen, Y. Zhang and S. Cao, *Appl. Catal., B*, 2017, **209**, 311–319.

282 I. A. Amar, R. Lan, J. Humphreys and S. Tao, *Catal. Today*, 2017, **286**, 51–56.

283 R. Zhang, X. Ren, X. Shi, F. Xie, B. Zheng, X. Guo and X. Sun, *ACS Appl. Mater. Interfaces*, 2018, **10**, 28251–28255.

284 L. Yang, T. Wu, R. Zhang, H. Zhou, L. Xia, X. Shi, H. Zheng, Y. Zhang and X. Sun, *Nanoscale*, 2019, **11**, 1555–1562.

285 B. H. R. Suryanto, D. Wang, L. M. Azofra, M. Harb, L. Cavallo, R. Jalili, D. R. G. Mitchell, M. Chatti and D. R. MacFarlane, *ACS Energy Lett.*, 2019, **4**, 430–435.

286 Y. Abghoui, S. B. Sigtryggsson and E. Skúlason, *ChemSusChem*, 2019, **12**, 4265–4273.

287 R. Michalsky, Y.-J. Zhang, A. J. Medford and A. A. Peterson, *J. Phys. Chem. C*, 2014, **118**, 13026–13034.

288 X. Xu, F. Nosheen and X. Wang, *Chem. Mater.*, 2016, **28**, 6313–6320.

289 Y. Shi, Y. Yang, Y.-W. Li and H. Jiao, *ACS Catal.*, 2016, **6**, 6790–6803.

290 I. Matanovic and F. H. Garzon, *Phys. Chem. Chem. Phys.*, 2018, **20**, 14679–14687.

291 G. Gao, A. P. O'Mullane and A. Du, *ACS Catal.*, 2017, **7**, 494–500.

292 M. Naguib, M. Kurtoglu, V. Presser, J. Lu, J. Niu, M. Heon, L. Hultman, Y. Gogotsi and M. W. Barsoum, *Adv. Mater.*, 2011, **23**, 4248–4253.

293 L. M. Azofra, N. Li, D. R. MacFarlane and C. Sun, *Energy Environ. Sci.*, 2016, **9**, 2545–2549.

294 X. Ren, J. Zhao, Q. Wei, Y. Ma, H. Guo, Q. Liu, Y. Wang, G. Cui, A. M. Asiri, B. Li, B. Tang and X. Sun, *ACS Cent. Sci.*, 2019, **5**, 116–121.

295 Y. Abghoui and E. Skúlason, *Catal. Today*, 2017, **286**, 69–77.

296 Y. Abghoui and E. Skúlason, *J. Phys. Chem. C*, 2017, **121**, 6141–6151.

297 R. Zhang, Y. Zhang, X. Ren, G. Cui, A. M. Asiri, B. Zheng and X. Sun, *ACS Sustainable Chem. Eng.*, 2018, **6**, 9545–9549.

298 X. Zhang, R.-M. Kong, H. Du, L. Xia and F. Qu, *Chem. Commun.*, 2018, **54**, 5323–5325.

299 X. Zhu, T. Wu, L. Ji, Q. Liu, Y. Luo, G. Cui, Y. Xiang, Y. Zhang, B. Zheng and X. Sun, *Chem. Commun.*, 2020, **56**, 731–734.

300 H. Huang, L. Xia, R. Cao, Z. Niu, H. Chen, Q. Liu, T. Li, X. Shi, A. M. Asiri and X. Sun, *Chem. – Eur. J.*, 2019, **25**, 1914–1917.

301 Y. Song, D. Johnson, R. Peng, D. K. Hensley, P. V. Bonnesen, L. Liang, J. Huang, F. Yang, F. Zhang, R. Qiao, A. P. Baddorf, T. J. Tschaplinski, N. L. Engle, M. C. Hatzell, Z. Wu, D. A. Cullen, H. M. Meyer, B. G. Sumpter and A. J. Rondinone, *Sci. Adv.*, 2018, **4**, e1700336.

302 D. Yu, E. Nagelli, F. Du and L. Dai, *J. Phys. Chem. Lett.*, 2010, **1**, 2165–2173.

303 Y. Jiao, Y. Zheng, K. Davey and S.-Z. Qiao, *Nat. Energy*, 2016, **1**, 16130.

304 W. Li, T. Wu, S. Zhang, Y. Liu, C. Zhao, G. Liu, G. Wang, H. Zhang and H. Zhao, *Chem. Commun.*, 2018, **54**, 11188–11191.

305 D. S. Su, S. Perathoner and G. Centi, *Chem. Rev.*, 2013, **113**, 5782–5816.

306 T. Wu, X. Li, X. Zhu, S. Mou, Y. Luo, X. Shi, A. M. Asiri, Y. Zhang, B. Zheng, H. Zhao and X. Sun, *Chem. Commun.*, 2020, **56**, 1831–1834.

307 F. Pan, H. Zhang, K. Liu, D. Cullen, K. More, M. Wang, Z. Feng, G. Wang, G. Wu and Y. Li, *ACS Catal.*, 2018, **8**, 3116–3122.

308 D. W. Stephan, *Acc. Chem. Res.*, 2015, **48**, 306–316.

309 C. Zhao, S. Zhang, M. Han, X. Zhang, Y. Liu, W. Li, C. Chen, G. Wang, H. Zhang and H. Zhao, *ACS Energy Lett.*, 2019, **4**, 377–383.

310 S. Mukherjee, D. A. Cullen, S. Karakalos, K. Liu, H. Zhang, S. Zhao, H. Xu, K. L. More, G. Wang and G. Wu, *Nano Energy*, 2018, **48**, 217–226.

311 C. Lv, Y. Qian, C. Yan, Y. Ding, Y. Liu, G. Chen and G. Yu, *Angew. Chem., Int. Ed.*, 2018, **57**, 10246–10250.

312 G. Peng, J. Wu, M. Wang, J. Niklas, H. Zhou and C. Liu, *Nano Lett.*, 2020, **20**, 2879–2885.

313 X. Mao, S. Zhou, C. Yan, Z. Zhu and A. Du, *Phys. Chem. Chem. Phys.*, 2019, **21**, 1110–1116.

314 J. Zhao, X. Ren, X. Li, D. Fan, X. Sun, H. Ma, Q. Wei and D. Wu, *Nanoscale*, 2019, **11**, 4231–4235.

315 Z. Geng, Y. Liu, X. Kong, P. Li, K. Li, Z. Liu, J. Du, M. Shu, R. Si and J. Zeng, *Adv. Mater.*, 2018, **30**, 1803498.

316 X. Yu, P. Han, Z. Wei, L. Huang, Z. Gu, S. Peng, J. Ma and G. Zheng, *Joule*, 2018, **2**, 1610–1622.

317 F. Ma, Y. Jiao, G. Gao, Y. Gu, A. Bilic, Z. Chen and A. Du, *Nano Lett.*, 2016, **16**, 3022–3028.

318 C. Liu, Q. Li, C. Wu, J. Zhang, Y. Jin, D. R. MacFarlane and C. Sun, *J. Am. Chem. Soc.*, 2019, **141**, 2884–2888.

319 C. Hering-Junghans, *Angew. Chem., Int. Ed.*, 2018, **57**, 6738–6740.

320 B. M. Hoffman, D. Lukoyanov, Z.-Y. Yang, D. R. Dean and L. C. Seefeldt, *Chem. Rev.*, 2014, **114**, 4041–4062.

321 Y. Fu and A. Manthiram, *RSC Adv.*, 2012, **2**, 5927–5929.

322 H. Chen, X. Zhu, H. Huang, H. Wang, T. Wang, R. Zhao, H. Zheng, A. M. Asiri, Y. Luo and X. Sun, *Chem. Commun.*, 2019, **55**, 3152–3155.

323 L. Xia, J. Yang, H. Wang, R. Zhao, H. Chen, W. Fang, A. M. Asiri, F. Xie, G. Cui and X. Sun, *Chem. Commun.*, 2019, **55**, 3371–3374.

324 T. Wu, P. Li, H. Wang, R. Zhao, Q. Zhou, W. Kong, M. Liu, Y. Zhang, X. Sun and F. Gong, *Chem. Commun.*, 2019, **55**, 2684–2687.

325 C. Choi, S. Back, N.-Y. Kim, J. Lim, Y.-H. Kim and Y. Jung, *ACS Catal.*, 2018, **8**, 7517–7525.

326 C. Chen, D. Yan, Y. Wang, Y. Zhou, Y. Zou, Y. Li and S. Wang, *Small*, 2019, **15**, 1805029.

327 X. Zhang, T. Wu, H. Wang, R. Zhao, H. Chen, T. Wang, P. Wei, Y. Luo, Y. Zhang and X. Sun, *ACS Catal.*, 2019, **9**, 4609–4615.

328 W. Qiu, X.-Y. Xie, J. Qiu, W.-H. Fang, R. Liang, X. Ren, X. Ji, G. Cui, A. M. Asiri, G. Cui, B. Tang and X. Sun, *Nat. Commun.*, 2018, **9**, 3485.

329 Z. Wei, Y. Zhang, S. Wang, C. Wang and J. Ma, *J. Mater. Chem. A*, 2018, **6**, 13790–13796.

330 L. Zhang, L.-X. Ding, G.-F. Chen, X. Yang and H. Wang, *Angew. Chem.*, 2019, **131**, 2638–2642.

331 X. Zhu, S. Mou, Q. Peng, Q. Liu, Y. Luo, G. Chen, S. Gao and X. Sun, *J. Mater. Chem. A*, 2020, **8**, 1545–1556.

332 G.-F. Chen, X. Cao, S. Wu, X. Zeng, L.-X. Ding, M. Zhu and H. Wang, *J. Am. Chem. Soc.*, 2017, **139**, 9771–9774.

333 Y. Yang, S.-Q. Wang, H. Wen, T. Ye, J. Chen, C.-P. Li and M. Du, *Angew. Chem., Int. Ed.*, 2019, **58**, 15362–15366.

334 D. T. Whipple and P. J. A. Kenis, *J. Phys. Chem. Lett.*, 2010, **1**, 3451–3458.

335 J. Artz, T. E. Müller, K. Thenert, J. Kleinekorte, R. Meys, A. Sternberg, A. Bardow and W. Leitner, *Chem. Rev.*, 2018, **118**, 434–504.

336 A. M. Appel, J. E. Bercaw, A. B. Bocarsly, H. Dobbek, D. L. DuBois, M. Dupuis, J. G. Ferry, E. Fujita, R. Hille, P. J. A. Kenis, C. A. Kerfeld, R. H. Morris, C. H. F. Peden, A. R. Portis, S. W. Ragsdale, T. B. Rauchfuss, J. N. H. Reek, L. C. Seefeldt, R. K. Thauer and G. L. Waldrop, *Chem. Rev.*, 2013, **113**, 6621–6658.

337 S. Roy, A. Cherevotan and S. C. Peter, *ACS Energy Lett.*, 2018, **3**, 1938–1966.

338 J. Wu, Y. Huang, W. Ye and Y. Li, *Adv. Sci.*, 2017, **4**, 1700194.

339 P. Lu, X. Tan, H. Zhao, Q. Xiang, K. Liu, X. Zhao, X. Yin, X. Li, X. Hai, S. Xi, A. T. S. Wee, S. J. Pennycook, X. Yu, M. Yuan, J. Wu, G. Zhang, S. C. Smith and Z. Yin, *ACS Nano*, 2021, **15**, 5671–5678.

340 R. Kortlever, J. Shen, K. J. P. Schouten, F. Calle-Vallejo and M. T. M. Koper, *J. Phys. Chem. Lett.*, 2015, **6**, 4073–4082.

341 L. R. L. Ting and B. S. Yeo, *Curr. Opin. Electrochem.*, 2018, **8**, 126–134.

342 L. Wang, W. Chen, D. Zhang, Y. Du, R. Amal, S. Qiao, J. Wu and Z. Yin, *Chem. Soc. Rev.*, 2019, **48**, 5310–5349.

343 R. Zhao, P. Ding, P. Wei, L. Zhang, Q. Liu, Y. Luo, T. Li, S. Lu, X. Shi, S. Gao, A. M. Asiri, Z. Wang and X. Sun, *Adv. Funct. Mater.*, 2021, **31**, 2009449.

344 Y. Y. Birdja, E. Pérez-Gallent, M. C. Figueiredo, A. J. Göttle, F. Calle-Vallejo and M. T. M. Koper, *Nat. Energy*, 2019, **4**, 732–745.

345 H. Yoshio, K. Katsuhei, M. Akira and S. Shin, *Chem. Lett.*, 1986, 897–898.

346 E. Benson, C. P. Kubiak, A. J. Sathrum and J. M. Smieja, *Chem. Soc. Rev.*, 2009, **38**, 89–99.

347 J. Qiao, Y. Liu, F. Hong and J. Zhang, *Chem. Soc. Rev.*, 2014, **43**, 631–675.

348 X. Sun, X. Kang, Q. Zhu, J. Ma, G. Yang, Z. Liu and B. Han, *Chem. Sci.*, 2016, **7**, 2883–2887.

349 O. S. Bushuyev, P. De Luna, C. T. Dinh, L. Tao, G. Saur, J. van de Lagemaat, S. O. Kelley and E. H. Sargent, *Joule*, 2018, **2**, 825–832.

350 R. J. Lim, M. Xie, M. A. Sk, J.-M. Lee, A. Fisher, X. Wang and K. H. Lim, *Catal. Today*, 2014, **233**, 169–180.

351 Z. Wang, Y. Li, H. Yu, Y. Xu, H. Xue, X. Li, H. Wang and L. Wang, *ChemSusChem*, 2018, **11**, 3480–3485.

352 M.-M. Shi, D. Bao, B.-R. Wulan, Y.-H. Li, Y.-F. Zhang, J.-M. Yan and Q. Jiang, *Adv. Mater.*, 2017, **29**, 1606550.

353 S.-J. Li, D. Bao, M.-M. Shi, B.-R. Wulan, J.-M. Yan and Q. Jiang, *Adv. Mater.*, 2017, **29**, 1700001.

354 M. Wang, S. Liu, T. Qian, J. Liu, J. Zhou, H. Ji, J. Xiong, J. Zhong and C. Yan, *Nat. Commun.*, 2019, **10**, 341.

355 Y. Yao, Q. Feng, S. Zhu, J. Li, Y. Yao, Y. Wang, Q. Wang, M. Gu, H. Wang, H. Li, X.-Z. Yuan and M. Shao, *Small Methods*, 2019, **3**, 1800324.

356 R. Manjunatha, A. Karajić, V. Goldstein and A. Schechter, *ACS Appl. Mater. Interfaces*, 2019, **11**, 7981–7989.

357 P. Wei, H. Xie, X. Zhu, R. Zhao, L. Ji, X. Tong, Y. Luo, G. Cui, Z. Wang and X. Sun, *ACS Sustainable Chem. Eng.*, 2020, **8**, 29–33.

358 X. Zhao, X. Lan, D. Yu, H. Fu, Z. Liu and T. Mu, *Chem. Commun.*, 2018, **54**, 13010–13013.

359 R. Zhang, L. Ji, W. Kong, H. Wang, R. Zhao, H. Chen, T. Li, B. Li, Y. Luo and X. Sun, *Chem. Commun.*, 2019, **55**, 5263–5266.

360 L. Xia, X. Wu, Y. Wang, Z. Niu, Q. Liu, T. Li, X. Shi, A. M. Asiri and X. Sun, *Small Methods*, 2019, **3**, 1800251.

361 R. Francke, B. Schille and M. Roemelt, *Chem. Rev.*, 2018, **118**, 4631–4701.

362 Y. Wang, J. Liu, Y. Wang, A. M. Al-Enizi and G. Zheng, *Small*, 2017, **13**, 1701809.

363 R. Schlögl, *Angew. Chem., Int. Ed.*, 2015, **54**, 3465–3520.

364 J. Schneider, H. Jia, J. T. Muckerman and E. Fujita, *Chem. Soc. Rev.*, 2012, **41**, 2036–2051.

365 E. V. Kondratenko, G. Mul, J. Baltrusaitis, G. O. Larrazábal and J. Pérez-Ramírez, *Energy Environ. Sci.*, 2013, **6**, 3112–3135.

366 J. Albo, M. Alvarez-Guerra, P. Castaño and A. Irabien, *Green Chem.*, 2015, **17**, 2304–2324.

367 M. F. Baruch, J. E. Pander, J. L. White and A. B. Bocarsly, *ACS Catal.*, 2015, **5**, 3148–3156.

368 J. E. Pander, M. F. Baruch and A. B. Bocarsly, *ACS Catal.*, 2016, **6**, 7824–7833.

369 A. Dutta, A. Kuzume, M. Rahaman, S. Vesztergom and P. Broekmann, *ACS Catal.*, 2015, **5**, 7498–7502.

370 C. Cui, J. Han, X. Zhu, X. Liu, H. Wang, D. Mei and Q. Ge, *J. Catal.*, 2016, **343**, 257–265.

371 J. T. Feaster, C. Shi, E. R. Cave, T. Hatsukade, D. N. Abram, K. P. Kuhl, C. Hahn, J. K. Nørskov and T. F. Jaramillo, *ACS Catal.*, 2017, **7**, 4822–4827.

372 J. L. White and A. B. Bocarsly, *J. Electrochem. Soc.*, 2016, **163**, H410–H416.

373 S. Back, J.-H. Kim, Y.-T. Kim and Y. Jung, *Phys. Chem. Chem. Phys.*, 2016, **18**, 9652–9657.

374 J. H. Koh, D. H. Won, T. Eom, N.-K. Kim, K. D. Jung, H. Kim, Y. J. Hwang and B. K. Min, *ACS Catal.*, 2017, **7**, 5071–5077.

375 J. S. Yoo, R. Christensen, T. Vegge, J. K. Nørskov and F. Studt, *ChemSusChem*, 2016, **9**, 358–363.

376 N. J. Firet and W. A. Smith, *ACS Catal.*, 2017, **7**, 606–612.

377 S. Back, M. S. Yeom and Y. Jung, *ACS Catal.*, 2015, **5**, 5089–5096.

378 T. Cheng, Y. Huang, H. Xiao and W. A. Goddard, *J. Phys. Chem. Lett.*, 2017, **8**, 3317–3320.

379 J. Rosen, G. S. Hutchings, Q. Lu, S. Rivera, Y. Zhou, D. G. Vlachos and F. Jiao, *ACS Catal.*, 2015, **5**, 4293–4299.

380 H.-E. Lee, K. D. Yang, S. M. Yoon, H.-Y. Ahn, Y. Y. Lee, H. Chang, D. H. Jeong, Y.-S. Lee, M. Y. Kim and K. T. Nam, *ACS Nano*, 2015, **9**, 8384–8393.

381 A. D. Handoko, K. W. Chan and B. S. Yeo, *ACS Energy Lett.*, 2017, **2**, 2103–2109.

382 E. Pérez-Gallent, M. C. Figueiredo, F. Calle-Vallejo and M. T. M. Koper, *Angew. Chem., Int. Ed.*, 2017, **56**, 3621–3624.

383 J. D. Goodpaster, A. T. Bell and M. Head-Gordon, *J. Phys. Chem. Lett.*, 2016, **7**, 1471–1477.

384 D. Ren, B. S.-H. Ang and B. S. Yeo, *ACS Catal.*, 2016, **6**, 8239–8247.

385 S. Lee, G. Park and J. Lee, *ACS Catal.*, 2017, **7**, 8594–8604.

386 S. Gao, Y. Lin, X. Jiao, Y. Sun, Q. Luo, W. Zhang, D. Li, J. Yang and Y. Xie, *Nature*, 2016, **529**, 68–71.

387 S. Ma, M. Sadakiyo, R. Luo, M. Heima, M. Yamauchi and P. J. A. Kenis, *J. Power Sources*, 2016, **301**, 219–228.

388 F. Calle-Vallejo and M. T. M. Koper, *Angew. Chem., Int. Ed.*, 2013, **52**, 7282–7285.

389 Y. Huang, A. D. Handoko, P. Hirunsit and B. S. Yeo, *ACS Catal.*, 2017, **7**, 1749–1756.

390 C. Hahn, T. Hatsukade, Y.-G. Kim, A. Vailionis, J. H. Baricuatro, D. C. Higgins, S. A. Nitopi, M. P. Soriaga and T. F. Jaramillo, *Proc. Natl. Acad. Sci. U. S. A.*, 2017, **114**, 5918.

391 H.-R. M. Jhong, S. Ma and P. J. A. Kenis, *Curr. Opin. Chem. Eng.*, 2013, **2**, 191–199.

392 X. Duan, J. Xu, Z. Wei, J. Ma, S. Guo, S. Wang, H. Liu and S. Dou, *Adv. Mater.*, 2017, **29**, 1701784.

393 A. Loiudice, P. Lobaccaro, E. A. Kamali, T. Thao, B. H. Huang, J. W. Ager and R. Buonsanti, *Angew. Chem., Int. Ed.*, 2016, **55**, 5789–5792.

394 M. B. Ross, C. T. Dinh, Y. Li, D. Kim, P. De Luna, E. H. Sargent and P. Yang, *J. Am. Chem. Soc.*, 2017, **139**, 9359–9363.

395 M. M. Abdelnaby, K. Liu, K. Hassanein and Z. Yin, *ChemNanoMat*, 2021, **7**, 969–981.

396 S. Nitopi, E. Bertheussen, S. B. Scott, X. Liu and I. Chorkendorff, *Chem. Rev.*, 2019, **119**, 7610–7672.

397 B. Jiang, X.-G. Zhang, K. Jiang, D.-Y. Wu and W.-B. Cai, *J. Am. Chem. Soc.*, 2018, **140**, 2880–2889.

398 H. S. Jeon, I. Sinev, F. Scholten, N. J. Divins, I. Zegkinoglou, L. Pielsticker and B. R. Cuenya, *J. Am. Chem. Soc.*, 2018, **140**, 9383–9386.

399 S. Y. Lee, H. Jung, N.-K. Kim, H.-S. Oh, B. K. Min and Y. J. Hwang, *J. Am. Chem. Soc.*, 2018, **140**, 8681–8689.

400 M. Ma, B. J. Trześniewski, J. Xie and W. A. Smith, *Angew. Chem., Int. Ed.*, 2016, **55**, 9748–9752.

401 Y.-X. Duan, F.-L. Meng, K.-H. Liu, S.-S. Yi, S.-J. Li, J.-M. Yan and Q. Jiang, *Adv. Mater.*, 2018, **30**, 1706194.

402 R. M. Arán-Ais, F. Scholten, S. Kunze, R. Rizo and B. Roldan Cuenya, *Nat. Energy*, 2020, **5**, 317–325.

403 J. Xie, X. Zhao, M. Wu, Q. Li, Y. Wang and J. Yao, *Angew. Chem.*, 2018, **130**, 9788–9792.

404 T. T. H. Hoang, S. Verma, S. Ma, T. T. Fister, J. Timoshenko, A. I. Frenkel, P. J. A. Kenis and A. A. Gewirth, *J. Am. Chem. Soc.*, 2018, **140**, 5791–5797.

405 E. L. Clark, C. Hahn, T. F. Jaramillo and A. T. Bell, *J. Am. Chem. Soc.*, 2017, **139**, 15848–15857.

406 J. T. L. Gamler, H. M. Ashberry, S. E. Skrabalak and K. M. Koczkur, *Adv. Mater.*, 2018, **30**, 1801563.

407 D. Kim, C. Xie, N. Becknell, Y. Yu, M. Karamad, K. Chan, E. J. Crumlin, J. K. Nørskov and P. Yang, *J. Am. Chem. Soc.*, 2017, **139**, 8329–8336.

408 S. Ma, M. Sadakiyo, M. Heima, R. Luo, R. T. Haasch, J. I. Gold, M. Yamauchi and P. J. A. Kenis, *J. Am. Chem. Soc.*, 2017, **139**, 47–50.

409 X. Zhang, F. Li, Y. Zhang, A. M. Bond and J. Zhang, *J. Mater. Chem. A*, 2018, **6**, 7851–7858.

410 H. B. Yang, S.-F. Hung, S. Liu, K. Yuan, S. Miao, L. Zhang, X. Huang, H.-Y. Wang, W. Cai, R. Chen, J. Gao, X. Yang, W. Chen, Y. Huang, H. M. Chen, C. M. Li, T. Zhang and B. Liu, *Nat. Energy*, 2018, **3**, 140–147.

411 X. Wang, Z. Chen, X. Zhao, T. Yao, W. Chen, R. You, C. Zhao, G. Wu, J. Wang, W. Huang, J. Yang, X. Hong, S. Wei, Y. Wu and Y. Li, *Angew. Chem.*, 2018, **130**, 1962–1966.

412 Y. Pan, R. Lin, Y. Chen, S. Liu, W. Zhu, X. Cao, W. Chen, K. Wu, W.-C. Cheong, Y. Wang, L. Zheng, J. Luo, Y. Lin, Y. Liu, C. Liu, J. Li, Q. Lu, X. Chen, D. Wang, Q. Peng, C. Chen and Y. Li, *J. Am. Chem. Soc.*, 2018, **140**, 4218–4221.

413 Y. Cheng, S. Zhao, B. Johannessen, J.-P. Veder, M. Saunders, M. R. Rowles, M. Cheng, C. Liu, M. F. Chisholm, R. De Marco, H.-M. Cheng, S.-Z. Yang and S. P. Jiang, *Adv. Mater.*, 2018, **30**, 1706287.

414 N. M. Adli, W. T. Shan, S. Hwang, W. Samarakoon, S. Karakalos, Y. Li, D. A. Cullen, D. Su, Z. X. Feng, G. F. Wang and G. Wu, *Angew. Chem., Int. Ed.*, 2021, **60**, 1022–1032.

415 H. Jin, C. Guo, X. Liu, J. Liu, A. Vasileff, Y. Jiao, Y. Zheng and S.-Z. Qiao, *Chem. Rev.*, 2018, **118**, 6337–6408.

416 W. Zhang, Q. Qin, L. Dai, R. Qin, X. Zhao, X. Chen, D. Ou, J. Chen, T. T. Chuong, B. Wu and N. Zheng, *Angew. Chem., Int. Ed.*, 2018, **57**, 9475–9479.

417 C. Cao, D.-D. Ma, J.-F. Gu, X. Xie, G. Zeng, X. Li, S.-G. Han, Q.-L. Zhu, X.-T. Wu and Q. Xu, *Angew. Chem., Int. Ed.*, 2020, **59**, 15014–15020.

418 F. P. García de Arquer, O. S. Bushuyev, P. De Luna, C.-T. Dinh, A. Seifitokaldani, M. I. Saidaminov, C.-S. Tan, L. N. Quan, A. Proppe, M. G. Kibria, S. O. Kelley, D. Sinton and E. H. Sargent, *Adv. Mater.*, 2018, **30**, 1802858.

419 W. Bi, C. Wu and Y. Xie, *ACS Energy Lett.*, 2018, **3**, 624–633.

420 J. Xu, X. Li, W. Liu, Y. Sun, Z. Ju, T. Yao, C. Wang, H. Ju, J. Zhu, S. Wei and Y. Xie, *Angew. Chem., Int. Ed.*, 2017, **56**, 9121–9125.

421 N. Elgrishi, M. B. Chambers, X. Wang and M. Fontecave, *Chem. Soc. Rev.*, 2017, **46**, 761–796.

422 N. Han, Y. Wang, L. Ma, J. Wen, J. Li, H. Zheng, K. Nie, X. Wang, F. Zhao, Y. Li, J. Fan, J. Zhong, T. Wu, D. J. Miller, J. Lu, S.-T. Lee and Y. Li, *Chem*, 2017, **3**, 652–664.

423 W.-H. Wang, Y. Himeda, J. T. Muckerman, G. F. Manbeck and E. Fujita, *Chem. Rev.*, 2015, **115**, 12936–12973.

424 W. Zhang, W. Lai and R. Cao, *Chem. Rev.*, 2017, **117**, 3717–3797.

425 X. Zhang, Z. Wu, X. Zhang, L. Li, Y. Li, H. Xu, X. Li, X. Yu, Z. Zhang, Y. Liang and H. Wang, *Nat. Commun.*, 2017, **8**, 14675.

426 M. Wang, L. Chen, T.-C. Lau and M. Robert, *Angew. Chem., Int. Ed.*, 2018, **57**, 7769–7773.

427 O. G. Sánchez, Y. Y. Birdja, M. Bulut, J. Vaes, T. Breugelmans and D. Pant, *Curr. Opin. Green Sust.*, 2019, **16**, 47–56.

428 S. Zhang, P. Kang, S. Ubnoske, M. K. Brennaman, N. Song, R. L. House, J. T. Glass and T. J. Meyer, *J. Am. Chem. Soc.*, 2014, **136**, 7845–7848.

429 H. Wang, Y. Chen, X. Hou, C. Ma and T. Tan, *Green Chem.*, 2016, **18**, 3250–3256.

430 K. Nakata, T. Ozaki, C. Terashima, A. Fujishima and Y. Einaga, *Angew. Chem., Int. Ed.*, 2014, **53**, 871–874.

431 K. Natsui, H. Iwakawa, N. Ikemiya, K. Nakata and Y. Einaga, *Angew. Chem., Int. Ed.*, 2018, **57**, 2639–2643.

432 X. Xue, H. Yang, T. Yang, P. Yuan, Q. Li, S. Mu, X. Zheng, L. Chi, J. Zhu, Y. Li, J. Zhang and Q. Xu, *J. Mater. Chem. A*, 2019, **7**, 15271–15277.

433 T. Liu, S. Ali, Z. Lian, C. Si, D. S. Su and B. Li, *J. Mater. Chem. A*, 2018, **6**, 19998–20004.

434 H. Yang, Y. Wu, Q. Lin, L. Fan, X. Chai, Q. Zhang, J. Liu, C. He and Z. Lin, *Angew. Chem., Int. Ed.*, 2018, **57**, 15476–15480.

435 G.-L. Chai and Z.-X. Guo, *Chem. Sci.*, 2016, **7**, 1268–1275.

436 H. Wang, J. Jia, P. Song, Q. Wang, D. Li, S. Min, C. Qian, L. Wang, Y. F. Li, C. Ma, T. Wu, J. Yuan, M. Antonietti and G. A. Ozin, *Angew. Chem., Int. Ed.*, 2017, **56**, 7847–7852.

437 J. Wu, M. Liu, P. P. Sharma, R. M. Yadav, L. Ma, Y. Yang, X. Zou, X.-D. Zhou, R. Vajtai, B. I. Yakobson, J. Lou and P. M. Ajayan, *Nano Lett.*, 2016, **16**, 466–470.

438 J. Wu, S. Ma, J. Sun, J. I. Gold, C. Tiwary, B. Kim, L. Zhu, N. Chopra, I. N. Odeh, R. Vajtai, A. Z. Yu, R. Luo, J. Lou, G. Ding, P. J. A. Kenis and P. M. Ajayan, *Nat. Commun.*, 2016, **7**, 13869.

439 Y. Song, W. Chen, C. Zhao, S. Li, W. Wei and Y. Sun, *Angew. Chem., Int. Ed.*, 2017, **56**, 10840–10844.

440 Y. Liu, Y. Zhang, K. Cheng, X. Quan, X. Fan, Y. Su, S. Chen, H. Zhao, Y. Zhang, H. Yu and M. R. Hoffmann, *Angew. Chem., Int. Ed.*, 2017, **56**, 15607–15611.

441 X.-M. Hu, H. H. Hval, E. T. Bjerglund, K. J. Dalgaard, M. R. Madsen, M.-M. Pohl, E. Welter, P. Lamagni, K. B. Buhl, M. Bremholm, M. Beller, S. U. Pedersen, T. Skrydstrup and K. Daasbjerg, *ACS Catal.*, 2018, **8**, 6255–6264.

442 X. Sun, L. Lu, Q. Zhu, C. Wu, D. Yang, C. Chen and B. Han, *Angew. Chem., Int. Ed.*, 2018, **57**, 2427–2431.

443 W. Ju, A. Bagger, G.-P. Hao, A. S. Varela, I. Sinev, V. Bon, B. Roldan Cuenya, S. Kaskel, J. Rossmeisl and P. Strasser, *Nat. Commun.*, 2017, **8**, 944.

444 C. Chen, X. Sun, X. Yan, Y. Wu, H. Liu, Q. Zhu, B. B. A. Bediako and B. Han, *Angew. Chem., Int. Ed.*, 2020, **59**, 11123–11129.

445 Y. Liu, S. Chen, X. Quan and H. Yu, *J. Am. Chem. Soc.*, 2015, **137**, 11631–11636.

446 L. Ye, Y. Ying, D. Sun, Z. Zhang, L. Fei, Z. Wen, J. Qiao and H. Huang, *Angew. Chem., Int. Ed.*, 2020, **59**, 3244–3251.

447 Y. Jiao, Y. Zheng, P. Chen, M. Jaroniec and S.-Z. Qiao, *J. Am. Chem. Soc.*, 2017, **139**, 18093–18100.

448 J. Wu, R. M. Yadav, M. Liu, P. P. Sharma, C. S. Tiwary, L. Ma, X. Zou, X.-D. Zhou, B. I. Yakobson, J. Lou and P. M. Ajayan, *ACS Nano*, 2015, **9**, 5364–5371.

449 B. Kumar, M. Asadi, D. Pisasale, S. Sinha-Ray, B. A. Rosen, R. Haasch, J. Abiade, A. L. Yarin and A. Salehi-Khojin, *Nat. Commun.*, 2013, **4**, 2819.

450 H. Yin, K. Xing, Y. Zhang, D. M. A. S. Dissanayake, Z. Lu, H. Zhao, Z. Zeng, J.-H. Yun, D.-C. Qi and Z. Yin, *Chem. Soc. Rev.*, 2021, **50**, 6423–6482.

451 N. Uddin, H. Zhang, Y. Du, G. Jia, S. Wang and Z. Yin, *Adv. Mater.*, 2020, **32**, 1905739.

452 Y. Yu, Y. Shi and B. Zhang, *Acc. Chem. Res.*, 2018, **51**, 1711–1721.

453 F. Lai, Z. Sun, S. E. Saji, Y. He, X. Yu, H. Zhao, H. Guo and Z. Yin, *Small*, 2021, **17**, 2100024.

454 O. A. Moses, L. Gao, H. Zhao, Z. Wang, M. Lawan Adam, Z. Sun, K. Liu, J. Wang, Y. Lu, Z. Yin and X. Yu, *Mater. Today*, 2021, **50**, 116–148.

455 M. Zhong, K. Tran, Y. Min, C. Wang, Z. Wang, C.-T. Dinh, P. De Luna, Z. Yu, A. S. Rasouli, P. Brodersen, S. Sun, O. Voznyy, C.-S. Tan, M. Askerka, F. Che, M. Liu, A. Seifitokaldani, Y. Pang, S.-C. Lo, A. Ip, Z. Ulissi and E. H. Sargent, *Nature*, 2020, **581**, 178–183.